

**Design of a Variable Camber Flap for Air Cargo
Challenge Aircraft**
(Versão final após defesa)

Ricardo Manuel Vitorino Soares

Dissertação para obtenção do Grau de Mestre em
Engenharia Aeronáutica
(Mestrado integrado)

Orientador: Prof. Doutor Pedro Vieira Gamboa

Dezembro de 2020

Acknowledgements

This work is the culmination of a long journey, one with some setbacks for sure. The support of those around, helped me steer through the rougher times and arrive at this important moment.

First, i would like to give my greatest thanks to my thesis adviser, professor Pedro Vieira Gamboa, for all the timely assistance and guidance when i most needed it, always bringing great insight and knowledge. I am also thankful for let me embark in a enriching experience that was Air Cargo Challenge 2019 edition project.

Secondly, i want to give special thanks to my colleagues and friends, Filipe Silva and Ricardo Palmeira for all the help in various classes during these final years. An extra thanks to Filipe for precious assistance in this work. Also want to acknowledge Joaquim Sousa for being a great friend and for all the support that he gave me.

Finally but not least important, i would never reached this point in my life without the support of my parents and sisters. The person that i am today and all that i achieved is thanks to them, for that i will always be grateful.

Resumo

A necessidade de uma aeronave mais competitiva para as edições do Air Cargo Challenge levou à procura de uma asa mais eficiente aerodinamicamente. Esta dissertação descreve os varios passos que levaram ao desenho de um flap sem fenda, com o mecanismo de atuação imbutido, para garantir uma superfície limpa. Multiplos espécimes com junta flexível foram produzidos e testados com recurso a uma bancada de testes construída para o efeito, de forma a calcular-se o binário necessário para determinada deflexão. As juntas têm o objetivo de servirem como cascas flexíveis na dobradiça do flap. Um dispositivo que revolve em torno de um eixo localizado no intradorso faz com que a casca do extradorso altere em comprimento, surgindo a necessidade de um material elástico. Um silicone RTV foi escolhido para fechar a fenda do flap. Um novo método experimental foi pensado para determinar o módulo de Young e o coeficiente de Poisson de forma a dimensionar a folha de silicone. Um teste foi realizado para aferir a capacidade de adesão de um agente selante.

A totalidade dos momentos que actuam sobre a dobradiça foram calculados. O momento aerodinâmico foi determinado com o recurso ao programa XFOIL, enquanto o do elastômero foi calculado com base nas suas propriedades e em trigonometria. Devido há natureza elástica do silicone, os efeitos resultantes da pressão do ar foram avaliados recorrendo às curvas de C_P do XFOIL para calcular as cargas resultantes. Posteriormente uma análise MEF com o software comercial Ansys previu as deformações perpendiculares ao plano. Para dimensionar o sistema de actuação, um program foi escrito no Matlab. Optimização foi conseguida através da comparação do binário que o servo motor enacte na dobradiça com o somatório dos momentos resistentes (aerodinâmico, elastômero e junta flexível). Com toda a metodologia acima descrita, um desenho final, baseado no painel central da asa do modelo do ACC2019, foi apresentado. De forma a validar o conceito apresentado e os métodos utilizados, uma pequena secção (250 mm envergadura) foi fabricada com recurso a processos de manufactura de partes moldadas. Para o novo conceito, um processo de adesão para a folha de silicone foi pensado e este requeriu um molde próprio para o efeito. Depois de desmoldada, a secção foi trimada e o servo motor foi instalado para verificar a funcionalidade. Um último teste foi efectuado, realizando modificações à bancada de teste construída previamente, com a finalidade de comparar os momentos projectados com os do produto final.

Palavras-chave

Dispositivo flap; Casca de asa flexível; Perfil asa limpo.

Abstract

The need for a more competitive Air cargo challenge (ACC) aircraft led the pursuit for a more aerodynamic efficient wing. This work details the various steps taken in the design of a gap-less flap system with the actuation mechanism inside for a clean surface. Multiple flexible joint specimens designs were manufactured and tested with the help of a special constructed test bench to assert the required torque to bend certain degrees. The goal is to serve as a flexible skin in the flap hinge line. A system that rotates around an axis on the lower wing skin means that the upper skin changes in length, arising the need for a flexible material. A RTV silicone rubber was chosen to close the upper surface flap gap. A novel test apparatus was devised to determine the silicone Young's Modulus and Poisson's ratio so the sheet could be sized. An adhesion test was also performed using a suitable bonding agent to verify if it had the capability of performing the task at hand.

The full range of hinge acting moments was determined. Aerodynamic hinge moment was simulated with XFOIL software, while the elastomer's was calculated with the found properties and trigonometry. Due to the elastomeric nature of silicone, air pressure effects were evaluated using XFOIL C_p curves to calculate resulting loads and a subsequent FEM analyse with Ansys Mechanical module predicted the outer plane deformations. A program in Matlab was written to help dimension the actuation system. Optimization was achieved by comparing the servo motor available hinge torque with the resisting moments sum (aerodynamic, elastomer and flexible skin joint). With all the described methodology, a final design was purposed based on the central wing panel of ACC 2019 edition model. To not only validate the concept at hand but also the employed methodology, a small (250 mm span) section was manufactured using conventional 2 parts hollow moulded manufacturing process. For the novel concept, a silicone sheet bonding procedure was planned and required a special mould for the effect. After de-moulded, the section was trimmed and the servo motor was installed to check the concept functionality. A final experiment using a modified bench test was realized to compare the projected hinge moments with the built section one's.

Keywords

Flap device; Flexible wing skin; Clean aerofoil surface.

Contents

1	Introduction	1
1.1	Motivation	1
1.2	Objectives	1
1.3	Thesis Outline	2
2	Literature Review	3
2.1	Flap Devices	3
2.1.1	Plain Flap	4
2.1.2	Split Flap	4
2.1.3	Slotted Flap	4
2.1.4	Fowler Flap	4
2.1.5	Junkers Flap	4
2.2	Wing Morphing	5
2.3	Competition RC Aircraft Concepts	7
3	Experimental Procedure	11
3.1	Skin Specimens	11
3.1.1	Design	11
3.1.2	Manufacturing	12
3.1.3	Test Bench	14
3.1.4	Composite Laminate Data Processing	16
3.2	Elastomer	19
3.2.1	RTV Silicone Testing	20
3.2.2	Dumbbell Specimen	20
3.2.3	Photometry	22
3.2.4	Image and Data Processing Program	22
3.2.5	Elastomer Bonding Agent	23
3.2.6	Aerodynamic Hinge Moment	24
4	Flap Design, Manufacturing and Validation	27
4.1	Flap Design	27
4.1.1	Elastomer Skin Sizing	27
4.1.2	Flexible Laminate Joint	32
4.1.3	Actuation System	33
4.2	Manufacturing	37
4.2.1	Upper/Bottom Skins	37
4.2.2	Elastomer Sheet	40
4.2.3	Jig and Assembly	41
4.3	Flap Validation	45

5	Results	47
5.1	Composite Laminate Specimens	47
5.2	Elastomer Sheet	54
5.3	XFOIL Hinge Moment	55
5.4	Elastomer Hinge Moment	55
5.5	Silicone Sealant Bonding	56
5.6	Elastomer Deformation	57
5.7	Flap Hinge Moments	58
5.8	Flap Validation	59
6	Conclusions and Future Work	61
6.1	Conclusions	61
6.2	Future Work	62
	Bibliografia	63
A	Annexes	69
A.1	Datasheets of the used components	69
A.2	Technical Drawings	73
A.3	Matlab code	84

List of Figures

1.1	ACC2019 wing panel showing the upper skin gap and external flap horn linkage.	1
2.1	Flap devices.	3
2.2	Euphoria F5J glider bottom skin design: 1 - Peelply strip for hinge; 2 - Glass fibre cloth; 3 - 1mm balsa wood sheet; 4 - Wing spar caps cut-off; 5 - Hinge cut-off.	8
2.3	GCM Vertigo F5J glider wing tip upper skin manufacture: 1 - Mould with sinusoidal protrusion; 2 - Carbon fibre sheets; 3 - Joint fibre stripe; 4 - Cut in the bottom skin layer; 5 - CNC machined foam core.	8
2.4	Built in wipers manufacture: 1 - TE; 2 - Control surface; 3 - Double sided tape; 4 - Mylar sheet; 5 - Epoxy with micro-balloons mixture.	9
2.5	Upper wing surface gap seal: 1 - Thin tape; 2 - Cassette tape; 3 - Control surface.	9
3.1	Test specimens schematics: Left - Top view; Right - Side view from the 3 different joint types. Numbering represents the order of materials application.	12
3.2	Composite specimens curing process.	14
3.3	Test bench: 1 - Data acquisition board; 2 - Potentiometer; 3 - Servo motor; 4 - Load cell; 5 - LiFe battery; 6 - Battery eliminator circuit (BEC); 7 - Protractor; 8 - Clamp.	14
3.4	Multiple test combinations: a) 2 horn heights; b) 2 joint widths.	15
3.5	LabView VI work environment: a) Block diagram DAQ Assist assembly; b) Front panel WaveForm graph.	15
3.6	Apparatus for specimen deflection monitoring.	16
3.7	Angular relations and forces acting on the specimen.	17
3.8	Files sample data averaged with a PivotTable.	18
3.9	Length change in upper skin gap.	19
3.10	ASTM Die A part design for laser cutting.	21
3.11	Elastomer sheet for specimen laser cutting.	21
3.12	Elastomer testing: a) Apparatus for reading and saving force data; b) Camera/lens combo for specimen marks photos to posteriori calculate elongation.	22
3.13	Original image is processed so the specimen marks are isolated in a binary image.	23
3.14	Binary image objects are cleaned and their centroid found.	23
3.15	Geometry design routine: Purple - New airfoil with 20° trailing edge flap; White - NewACC2017 aerofoil.	25
4.1	Elastomer bonding position calculation based on flap deflection.	28
4.2	Elastomer joint moment schematics.	29
4.3	Elastomer's sheet thickness manufacture testing.	30

4.4	Aerofoil C_p distribution: left - positive deflection; right - negative deflection. Blue dashed line is the C_p curve.	31
4.5	Ansys mechanical displaying the mesh's element quality for test 1.	32
4.6	Force application schematics of a servo actuation system: 1 - Servo motor; 2 - Flap hinge.	33
4.7	Diagram: Angular and force relationships between both circular movements, dependent on flap deflection.	34
4.8	Plot illustrating the change in position.	35
4.9	Flap horn CATIA V5 part design: 1 - 7 mm gap for the elastomer sheet bonding.	35
4.10	Servo motor position and rod length determination.	36
4.11	Catia V5 part design of the remaining flap components: 1 - Elastomer sheet; 2 - Wing TE spar; 3 - Flap spar; 4 - Elastomer support.	37
4.12	Bottom shell manufacture: 1 - Balsa sheet A; 2 - Carbon strips; 3 - Balsa sheets B and C; 4 - Interior carbon layer A and B fabrics; 5 - Flap balsa sheet; 6 - Exterior carbon layer; x_1 - 69.5 mm; x_2 - 249 mm; x_3 - 254 mm. Red dashed lines represent the chamfer zones.	38
4.13	Upper shell manufacture: 1 - Balsa sheet A; 2 - Carbon strips; 3 - Balsa sheets B and C; 4 - Interior carbon layer; 5 - Flap balsa sheet; 6 - Exterior carbon layer; x_1 - 69.5 mm; x_2 - 249 mm. Red dashed lines represent the chamfer zones.	39
4.14	Elastomer curing process: Weights pressing a acrylic plate over the mould.	40
4.15	Elastomer upper shell bonding: a) Top view drawing with the cutting marks; b) Upper shell parts fixation in the 20° flap deflection mould; c) Bonding between the elastomer sheet and the upper shell with the silicone sealant.	41
4.16	Jig design and manufacture.	41
4.17	Servo bay: Left - Servo mount; Right - Reinforcement plate.	42
4.18	Shells LE closing laminate manufacture and main spar.	42
4.19	Finished panel section.	43
4.20	Panel assembly procedure: a) LECL and spars trimming and positioning; b) Epoxy resin with micro-balloons application; c) Parts adhesion to bottom shell; d) Elastomer support bonding to upper shell; e) Epoxy resin with micro-balloons application to upper and bottom shells for panel closing; f) Servo bay opening; g) Panel cutting and trimming.	44
4.21	Flap test procedure.	45
5.1	Specimen 1 torque per unit span versus measured deflection. Legend - deflection direction/horn height.	48
5.2	Specimen 2 torque per unit span versus measured deflection. Legend - deflection direction/joint width/horn height.	48
5.3	Specimen 3 torque per unit span versus measured deflection. Legend - deflection direction/joint width/horn height.	49
5.4	Specimen 4 torque per unit span versus measured deflection. Legend - deflection direction/joint width/horn height.	49

5.5	Specimen 5 torque per unit span versus measured deflection. Legend - deflection direction/joint width/horn height.	50
5.6	Specimen 6 torque per unit span versus measured deflection. Legend - deflection direction/joint width/horn height.	50
5.7	Torque per unit span versus measured deflection: 5 mm horn height and 3 mm joint width.	52
5.8	Torque per unit span versus measured deflection: 5 mm horn height and 5 mm joint width.	52
5.9	Torque per unit span versus measured deflection: 10 mm horn height and 3 mm joint width.	53
5.10	Torque per unit span versus measured deflection: 10 mm horn height and 5 mm joint width.	53
5.11	Elastomer stress versus strain test results and Young's modulus calculation.	54
5.12	Aerodynamic hinge moment per unit span for different Reynolds numbers.	55
5.13	Silicone sealant bonding shear stress tests. Horizontal dashed lines indicate the initial failure point.	56
5.14	Ansys mechanical deformation and Von-Mises stress analyse for test 3.	57
5.15	Hinge moment versus flap deflection: illustrates the available servo torque and the hinge moment to overcome.	58
5.16	Flap design and final build required torque comparison.	59

List of Tables

3.1	Specimen characterization.	13
3.2	2 part epoxy resin specifications.	13
3.3	RTV silicone rubber properties at 25°C.	19
3.4	Silicone sealant adhesion test specimen dimensions.	24
4.1	Flap design specifications.	27
4.2	P_f and P_1 x coordinate in relation P_0 and their x/c position.	30
4.3	Ansys static structural analyses parameters.	31
4.4	Solver control options	32
4.5	Servos specifications.	36
4.6	Manufacturing materials dimensions.	38
4.7	Manufacturing materials dimensions.	39
5.1	Specimens laminates joint thickness and neutral axis.	51
5.2	Predicted elastomer Young's modulus versus experimental test.	54
5.3	Elastomer Poisson's coefficient calculation.	54
5.4	Elastomer hinge moment by unit span (m) [N].	56
5.5	Shear stress calculation for the considered elastomer sheet dimensions.	57
5.6	Elastomer sheet deformation (Y axis) and Von-Mises stress.	57
5.7	Final versus predicted panel mass by unit span (m).	59
A.1	YZC-133 1 kg and 5 kg Load Cell.	69
A.2	Silicone acetate for wet rooms.	70
A.3	NI-TB 4330 data acquisition board.	71

List of Acronyms

ACC	Air Cargo Challenge
BEC	Battery Eliminator Circuit
CAD	Computer Assisted Design
DCA	Department of Aerospace Sciences
FEM	Finite Element Method
LE	Leading Edge
LECL	Leading Edge Closing Laminate
MFC	Macro Fibre Composite
NACA	National Advisory Committee for Aeronautics
PET	Polyethylene Terephthalate
PVA	Poly Vinyl Alcohol
RC	Radio Controlled
RMB	Right Mouse Button
RTV	Room Temperature Vulcanization
SMA	Shape Memory Alloy
STOL	Short Take-Off and Landing
TE	Trailing Edge
UBI	University of Beira Interior
VI	Virtual Instrument

Nomenclature

A	Section Area [mm ²]
b_h	Flap horn lever's [mm]
b_s	Servo motor lever's [mm]
C_{D_0}	Zero lift drag coefficient
c	Aerofoil chord [m]
c_f	Flap cord [m]
C_{he}	Hinge moment coefficient
c_j	Distance between horn linkage and load cell axis [mm]
C_L	Lift coefficient
C_p	Pressure coefficient
d	Rod length [mm]
D	Test bench rod length [mm]
E	Young's Modulus [MPa]
E_1	First layer Young's Modulus [MPa]
E_2	Second layer Young's Modulus [MPa]
e	Measurement accuracy of the load cell [%]
e_H	Load cell, hysteresis error [%]
e_L	Load cell, non-linearity [%]
e_R	Load cell, repeatability [%]
e_S	Load cell, temperature effect on span [%/°C]
e_Z	Load cell, temperature effect on zero balance [%/°C]
F	Force [N]
F_e	Elastomer force [N]
$F_{e,t}$	F_e perpendicular component to the lever's fulcrum [N]
F_f	Form factor
F_h	Force generating hinge torque [N]
F_L	Lift [N]
F_s	Force resulting from servo torque [N]
$F_{s,r}$	Servo motor force transmitted to the rod [N]
F_1	Force enacted by rod on load cell [N]
F_{1h}	F_1 horizontal component [N]
F_2	Force enacted by specimen on rod [N]
F_{2t}	F_2 perpendicular component to the lever's fulcrum [N]
H	Distance between test bench line and load cell line [mm]
H^{bar}	Hinge moment per unit of span [N]
h	Distance between test bench line and horn linkage [mm]
h_0	h value for $\delta = 0$ [mm]
l	Span length [mm]
L	Unstrained elastomer length [mm]
L_0	Elastomer length at $\delta_f = 0$ [mm]

L/D	Lift to Drag ratio
L_f	Flap gap length [mm]
L_i	Minimum gap length and elastomer installation length [mm]
L_R	Rated capacity of the load cell [kg]
M_e	Moment enacted by elastomer at hinge [N m]
M_H	Aerodynamic hinge moment [N m]
$M_{h,s}$	Servo motor torque at hinge [N m]
M_j	Moment at specimen joint [N m]
M_s	Servo motor rated torque [kgf cm]
M_T	Sum of M_e , M_{He} and M_j [N m]
N	Number of load cells used
P_0	Hinge rotation axis
P_1	Elastomer fixation position on TE
$P_{1,x}$	P_1 x coordinate
$P_{1,y}$	P_1 y coordinate
P_f	Elastomer position at determined flap deflection
$P_{f,x}$	P_f x coordinate
$P_{f,y}$	P_f y coordinate
P_i	Elastomer position at maximum negative flap deflection
P_{ref}	Elastomer's flap position at $\delta_f = 0$
$P_{ref,x}$	P_{ref} x coordinate
$P_{ref,y}$	P_{ref} y coordinate
P_h	Connection point between rod and flap horn
P_s	Connection point between rod and servo motor
P_∞	Free stream pressure [Pa]
Q	Interference factor
r	Lever [mm]
S	Elastomer's hardness [Shore A]
t	Load cell temperature variation range [°C]
t_1	First layer thickness [mm]
t_2	Second layer thickness [mm]
u	x distance between servo motor and hinge rotation axis [mm]
v	y distance between servo motor and hinge rotation axis [mm]
V_∞	Free stream velocity [m/s]
W_1	Maximum load to be measured [kg]
x/c	Aerofoil chord fraction
x_e	X axis distance between P_1 and P_f [mm]
x_j	Distance between horn linkage and rotation axis [mm]
$x_{j,0}$	x value for $\delta = 0$ [mm]
y_n	Neutral axis position [mm]

Greek symbols

α	Angle of attack [°]
α_j	Angle between F_{2t} and F_2 [°]
α_e	Angle between $F_{e,t}$ and F_e [°]
α_h	Angle between $F_{s,r}$ and F_h [°]
α_s	Angle between F_s and $F_{s,r}$ [°]
β	Smaller angle between r and test bench line [°]
β_0	B value for $\delta = 0$ [°]
$\beta_{b,ref}$	Horn lever angle at $\delta_f = 0$ [°]
β_h	Angle between b_h and x axis [°]
β_s	Angle between b_s and x axis [°]
δ	Specimen deflection [°]
δ_f	Flap deflection [°]
$\delta_{f,stp}$	Flap deflection increments [°]
ΔL	Variation in length [°]
ε	Strain
γ_e	Angle between the elastomer's lever and the x axis [°]
γ_h	Angle between the rod and the horn lever [°]
γ_s	Angle between the rod and the servo lever [°]
ϕ	Angle between x axis and elastomer sheet [°]
ψ	Angle between the rod and the x axis [°]
Ψ	Angle between F_1 and F_{1h} [°]
ρ	Specific mass [Kg/m ³]
ρ_∞	Free stream specific mass [Kg/m ³]
σ	Stress [MPa]

Chapter 1

Introduction

1.1 Motivation

Air Cargo Challenge (ACC) is an international competition that takes place in Europe every two years and is directed at aeronautical and aerospace students. The goal is to design and build a radio controlled aeroplane that can lift the maximum payload possible, while complying to regulations given by the organizers. Final score is not only attributed based on the aircraft performance but also on other aspects like design report and presentation [1]. University of Beira Interior's (UBI) Department of Aerospace Sciences (DCA) has a long history of participation with multiple wins. Recent changes were done to the type of flight profile and a speed component was introduced. This factor allied with opposing teams getting better at each edition created the need to innovate and improve various aspects of the aircraft in order to stay competitive. A conventional control surface was used in ACC2019 model for both flaps and ailerons which have slot in the trailing edge of the wing (Figure 1.1). According the literature this is responsible for an 10% increase in the form factor (F_f) which directly influences the zero lift drag coefficient (C_{D_0}). The actuation was done by a servo motor and a rod connected to a horn in the control surface. Part of the components were on the exterior increasing the interference factor (Q), which again affects the C_{D_0} directly [2, p. 74-76]. The need to address these drawbacks paved the way for this work.

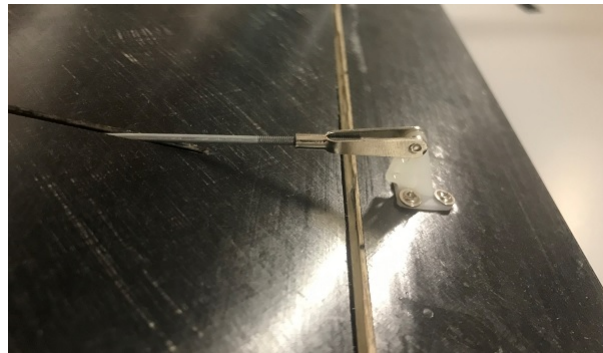


Figure 1.1: ACC2019 wing panel showing the upper skin gap and external flap horn linkage.

1.2 Objectives

This work has the main objective of improving ACC aircraft performance by designing a flap/flaperon system that results in a cleaner aerofoil in order to reduce drag. Various design aspects need to be tackled in order to succeed. In summary the main goals of this thesis are

as follows:

- Test various skins made with different combinations of composite materials, to find one flexible enough to function as a hinge in the wing's lower skin;
- Find a solution to remove or reduce the trailing edge slot in the upper wing skin;
- Move all the actuation system components inside the wing structure;
- Calculate the required torque to actuate the system, so proper servo motor can be selected;
- Present a final design based on the ACC2019 wing central panel;
- Manufacture and testing of a panel section in order to validate the final design and employed methodology.

1.3 Thesis Outline

This thesis consists of six main chapters including this one and their contents are summarized below:

- Chapter 1 details the motivation behind this work and the main objectives;
- Chapter 2 gives a brief overview over the main types of flap devices, reviews the recent work on trailing edge (TE) morphing and RC competition gliders designs and manufacturing techniques;
- Chapter 3 describes all the experiments performed in order to acquire the necessary data, so a flap/flaperon device could be designed;
- Chapter 4 covers the flap design and the entire panel section fabrication, including the employed manufacturing processes. The final experiment, realized in order to validate the design, is also described in this chapter;
- Chapter 5 presents and discusses all the experimental and simulation results;
- Chapter 6 gives the final conclusions and remarks, also presents possible future work to improve the presented design.

Chapter 2

Literature Review

In this chapter a brief overview at the 5 main flap devices types is presented with focus on their function and historical background. Then a review at the current wing trailing edge camber morphing state of the art is realized, particularly looking for actuation, structures and flexible skins morphing concepts. Finally a search at the current competition RC gliders and aeromodelling in general is accomplished, with emphasis on surface controls design and manufacturing techniques.

2.1 Flap Devices

Aircraft wings are designed and optimized for their main flight stage, in the case of commercial aeroplanes for cruise. This makes them inefficient at take-off and landing since the aerodynamic requirements are different for those stages [3], where high lift (F_L) at lower speeds is necessary for short distance take-off and landing (STOL). This lead to the installation of high-lift devices like flaps on the TE and slats at the leading edge (LE), which in turn increase the wing surface area and camber resulting in higher lift generation [4]. Flap devices can be divided into five main different types (Figure 2.1): plain flap; split flap; slotted flap; fowler flap; junkers flap.

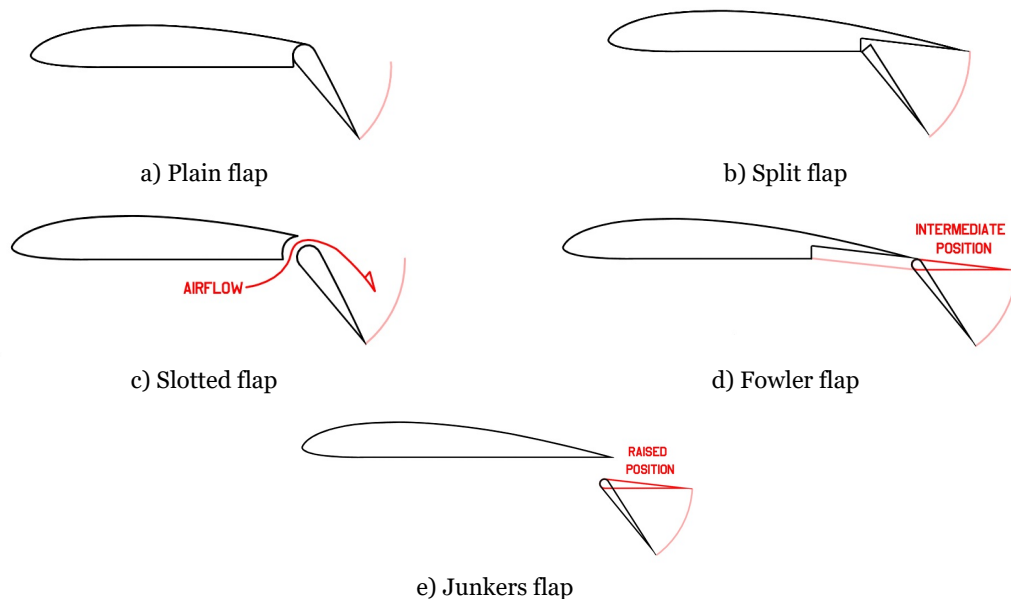


Figure 2.1: Flap devices.

2.1.1 Plain Flap

Plain flaps are the simplest flap device. A hinge close to the trailing edge of the wing enables these to deflect [5, p. 452]. But these are very limited in the amount of lift that they can create and result in the wing having a wake behind it proportionally to the deflection. Fairy Hamble Baby developed by the Fairy Aviation in 1916 was the first aeroplane to have plain flaps [6, p. 8-9]. Nowadays they are used for control surfaces and when simpler flap designs are preferred, found mainly in small aircraft.

2.1.2 Split Flap

Split flaps are located at the lower surface of the trailing edge and deflect downwards thanks to a hinge in the flap leading edge [5, p. 584]. They help increase lift, although like the plain flap, the generated amount is limited. At full deflection it has the particularity of acting like a spoiler increasing drag. Both increase in lift and mainly drag, increased the glide angle which was useful on approach [7, p. 367]. It was invented in 1920 by Orville Wright and James Jacobs. The Northrop Gamma and the Douglas DC-1 were the first to incorporate this design in 1932 [8, p. 17-18].

2.1.3 Slotted Flap

Slotted flaps have a gap between the wing trailing edge and the flap LE. This forces the higher pressure air in the bottom surface to move upwards delaying the airflow separation and as a result increases lift [5, p. 569]. Gustav Lachmann and Handley Page came out around the same time with the idea of a wing slot. They found that this design allowed greater angles of attack and a massive increase in lift. Lachmann ended working for Handley's company and in the process combined the slot with a flap creating the slotted flap which increased lift even further [8, p. 52]. This design is common among modern aircraft.

2.1.4 Fowler Flap

Fowler flaps slide backwards from the trailing edge raising the wing section area. As the flap extends, it then starts to curve downwards increasing aerofoil camber [5, p. 249-250]. The former increases lift without major drag penalties; the latter although with a benefit in lift generation it also increases drag significantly. Another characteristic is that the flap also provides a wing slot effect. This design was invented by Harlan D. Fowler, giving its name, in 1924 after becoming interested in wings with variable area during World War I. His concept was later tested by National Advisory Committee for Aeronautics (NACA), proving its performance [8, p. 236]. Today, Fowler flaps are widely used in combination with slotted flaps, sometimes with more than one slot, in commercial aviation.

2.1.5 Junkers Flap

Junkers flaps consist of a slotted plain flap fixed at the wing's trailing edge lower surface and rotates at its leading edge [5, p. 331]. A venturi effect occurs between the flap and wing's

lower surface increasing the airflow velocity. This gives energy to the upper wing surface boundary layer, particularly at lower air speed. On the downside, junkers flaps generate more drag specially at higher speeds. It was developed by Otto Mader, a German engineer, in late 1920's [9]. They were commonly used in Junkers aircraft and today are seen in some ultralights.

2.2 Wing Morphing

Modern wings are a compromise of the various flight envelop phases [10]. A wing that can change its shape (wing morphing) to fit the mission task at hand is a research topic among the scientific community, although this concept is not new. The Wright brothers used wing twist to control their first powered controlled flight. Also, the mentioned high lift devices in section 2.1 can be considered morphing since they alter the wing geometry. But they are necessary for an increase in aerodynamic performance and these systems usually do not enable the aircraft to perform different mission tasks [11]. So morphing can be described as structures that alter their shape to accommodate a new operating task or adapt in order to respond to environment conditions changes [12]. Serious attention for aerofoil morphing started at the end of last century [13] and current research involves technologies inspired in birds biology since they can change their wing's as required [14]. Barbarino et al. [15] made an extensive review of aircraft morphing.

For the purpose of this work, the focus will be on the recent research regarding trailing edge morphing. Although the final product may be quite conventional, the goal to create a continuous flexible flap system has some challenges that the current scientific work in morphing structures, skins and actuation mechanisms could help solving.

Vos et al. [16] described the application of piezoelectric bender actuators to introduce camber in the wing's trailing edge, so roll control could be achieved. Benders behaviour was accurately predicted through a deflection model. The author also found that by pre-compressing the actuators thanks to the use of an elastomer skin, deflections increased. Better results were obtained compared to traditional systems. Also massive decrease in control systems weight and parts, compared to traditional servo motors, was demonstrated.

Continuing his previous work, Vos et al. [17] details the design, modelling and testing of piezoelectric flight control mechanism for a morphing wing. A postbuckled pre-compressed bending actuator was mounted between the main spar and the trailing edge stiffener and an elastic skin covered the wing outside to serve as surface and to generate axial pre-compression in the piezoelectric actuator. A small air vehicle wing incorporating morphing panels at the outboard sides experienced excellent roll control. Again savings in operating empty weight were obtained compared with conventional servo actuators.

Bilgen et al. [18] described the implementation of a Macro Fibre Composite (MFC) actuator for wing morphing in a micro aerial vehicle. The actuation capability of this piezoceramic

actuator was tested in a wind tunnel and compared with a conventional trailing edge control surface. The morphing design exhibited less drag at equivalent lift. Later its stability and control was proven by flying a remotely pilot air vehicle with two MFC's actuators.

Barbarino et al. [19] presented a novel morphing trailing edge concept with the goal of replacing a conventional flap system. The trailing edge consisted of a multi-rib composed of 5 sections united by pairs of cross lamina, these had elastic properties so the structure could experience deflection. A shape memory alloy wire linked with the sections worked as actuator and its contraction enabled rotation. By estimating external aerodynamic load, the author concluded that although it caused a reduction in performance compared to no load, tip displacement was still above target.

Thill et al. [20] summarized the recent studies of corrugated structures for morphing wings. The author also built and wind tunnel tested a proof of concept trailing edge camber morphing aerofoil using corrugated sandwich structures. The demonstrator worked well at low speeds. Change in chord length and trailing edge deflections were achieved while maintaining a continuous aerofoil surface. A reduction in drag was also experienced by the use of a segmented exterior layer.

Popov et al. [21] modelled and experimented the performance of a morphing wing in a open-loop architecture. That was achieved by changing the shape of a flexible skin with the use of two shape memory alloy (SMA) actuators in a non-linear behaviour. The wing contained a cam that moves in the chord plane making a rod linked to a roller move perpendicular to the chord plane. A compression gas spring is heated to control the system by acting over the cam.

Vos et al. [22] described, through the examination of a directionally biased pressure adaptive honeycomb, a reduced order model capable of simplifying the geometry in Finite Element Method (FEM) analyses. This honeycomb, installed in the trailing edges, uses pressurization of the cells to alter the structure shape. For a zero cell differential pressure the honeycomb is relaxed and the flap is deflected. As cell pressure increases the flap retracts to its neutral position. Wing tunnel tests showed an increase in lift coefficient.

Woods et al. [23] introduced a novel morphing concept, the Fishbone Active Camber. As the name suggests, it is a design inspired by fish biology and allows continuous large aerofoil camber. Tendons were passed through holes in the stringers and connected to the trailing edge on one side, while the others were attached to a spooling pulley that in turn drove the system by means of actuator. Lift to drag ratio (L/D) was better when compared to a conventional flap aerofoil.

Liu et al. [24] proposed and studied the in-plane mechanical properties of a o Poisson's coefficient (ν) cosine honeycomb support structure. The characteristics were compared to the accordion honeycomb and was found that the former required less transversal driving

force to actuate. Capability for wing camber morphing was tested, proving suitability for one dimensional wing morphing.

Pankonien et al. [25] expanded upon already developed cascading bi-morph concepts. Span-wise morphing was achieved thanks to the use of spaced MFC's actuators and 3D printed flexure boxes with an elastomer skin closing the gaps. A elastomeric honeycomb skin was 3D printed to minimize bubbling due to aerodynamic load.

Yokozeki et al [26] developed and tested a morphing aerofoil using a corrugated flexible seamless flap like structure. It consisted of C-shaped circular and vertical straight sections. The flap is deflected downwards by means of a wire placed along the bottom surface connected to the trailing edge on one end and to a servo motor on the other. They evaluated and compared basic aerodynamic properties to a traditional hinged control surface and concluded that the morphing design exhibited superior properties in lift coefficient (C_l).

Kumar et al. [27] proposed a morphing wing design using a double corrugated variable camber structure. Structural and aerodynamic comparison was done to Yokozeki's [26] and Woods [23] work. FEM analyses showed that Kumar's design withstands larger stresses in both skin and corrugated structures while achieving similar trailing edge displacement. Thin aerofoil theory and XFOIL panel method demonstrated better aerodynamic performance.

kang et al. [28] devised a flap morphing mechanism that can change the wing shape smoothly to prevent aerodynamic losses. A SMA actuator using flexinol wires when heated shrunk and deformed a quadrilateral frame, which in return shifted the upper skin and deflected the trailing edge downwards like a flap. This design increased de pressure differential as the flap deflection angles kept increasing, but aerodynamic losses occurred due to flow separation at the flap rotation area.

2.3 Competition RC Aircraft Concepts

Aeromodelling is a field of interest to look for manufacturing techniques, parts and systems design. F5J and F3J competition gliders have similar characteristics to the ones desired in a Air Cargo Challenge aircraft, like a high wing aspect ratio, high L/D , high strength-to-weight ratio and smooth continuous surfaces to minimize aerodynamic drag. This made them prime candidates for research. In this section an overview of relevant wing designs and constructions techniques present in modern F5J and F3J gliders are summarized.

Euphoria F5J glider employs a wing made of reinforced glass fibre sandwich with balsa wood serving as core. In the manufacturing process [29] the glass cloth is impregnated with epoxy resin over a plastic film and after that another sheet is added on top. A mould is used to cut the fibre to dimension, then the plastic sheet on one of the sides is removed and the glass fibre is applied over the wing mould. A roller is used to properly spread the layer and then the remaining plastic sheet is removed. Again the roller is utilized to guarantee the proper appli-

cation of the glass cloth. A peelply strip is added in the flap and ailerons joint line to serve as hinge (Figure 2.2) The balsa wood core is applied over the mould; this sheet has cuttings for the flap and ailerons hinge, but also for the wing spar caps. Layers of impregnated carbon fibre fabric, to serve as spar caps, are added in the respective cut-off's. To finish, another glass layer is added over the balsa core and impregnated with resin. GCM's Vertigo F5J glider, for

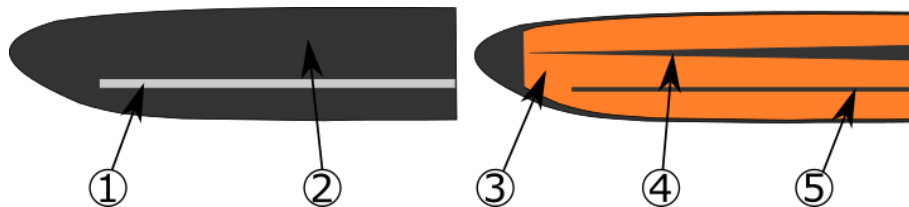


Figure 2.2: Euphoria F5J glider bottom skin design: 1 - Peelply strip for hinge; 2 - Glass fibre cloth; 3 - 1mm balsa wood sheet; 4 - Wing spar caps cut-off; 5 - Hinge cut-off.

its 2 wing tip panels construction, uses a machined foam core with indentations for the spar and ailerons hinges [30]. During initial production, the central panel used a sandwich type structure composed of a balsa wood core, an external layer of carbon fibre and an internal glass fibre layer. Newer models also started using a foam core for the panel structure [31]. Upper skin mould for the wing tips has a large sinusoidal protrusion while the central bottom skin mould has a small one. The carbon layers applied in these moulds are cut into 2 sections and placed on each side of the protrusion. A fibre stripe is applied over to connect both sides and function as a flexible hinge (Figure 2.3). The bottom wing tip skin is cut in the hinge line to enable deflection [32]. Similar to Vertigo, Samba's Prestige 2PK F5J also uses a sinusoidal upper skin hinge with a cut on the bottom layer for ailerons. They also recently moved from 2 piece hollow moulded panels to foam core [33]. One way to close the control

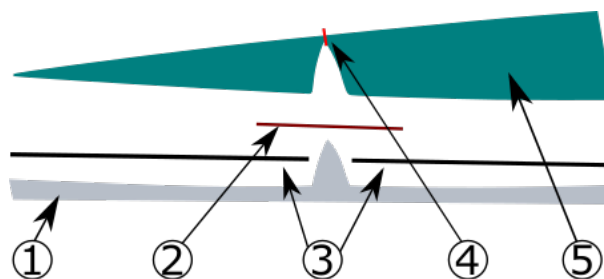


Figure 2.3: GCM Vertigo F5J glider wing tip upper skin manufacture: 1 - Mould with sinusoidal protrusion; 2 - Carbon fibre sheets; 3 - Joint fibre stripe; 4 - Cut in the bottom skin layer; 5 - CNC machined foam core.

surface upper skin gap is to install wipers, those can be bonded plastic films [34] or "built in" [35, 36] through an interesting manufacturing method. Joe Manor describes [37] in great detail this technique. First a double sided tape is applied to the control surface (Figure 2.4a) and any excess is trimmed, such that it is levelled with the wipers starting area. Then a very thin mylar sheet is bonded to the tape with enough length so it can be tucked under the wing upper skin TE (Figure 2.4b). The control surface is opened to a 90° angle or close to it and secured with tape, so the mylar sheet inside can be accessed. A mixture of epoxy resin with micro-balloons is then prepared, it should not be too thick or thin, and it is put inside a ziplock bag or another container that enables easy application. A thick strip is placed where

the mylar meets with the control surface. With the help of a small spatula the mix is spread inside towards the control surface spar or foam core. As this procedure is done, the applied mixture should be checked for air bubbles and, if any are present, those are removed with the spatula. Another large strip is disposed, but this time against the front end of the mylar and it is smoothed out so it has an even thickness across the wiper (Figure 2.4a). Again air bubbles are checked for. Finally, the mylar front end is tucked inside the TE (Figure 2.4b) and the panel is rotated so the mylar is facing down, allowing the epoxy to settle down during cure and not running into the hinge or TE (Figure 2.4c). After curing, the mylar and double sided tape are removed and the wiper front end is trimmed with sand paper (Figure 2.4d). A simple way to achieve a smooth continuous surface is to make a gap seal. An interesting

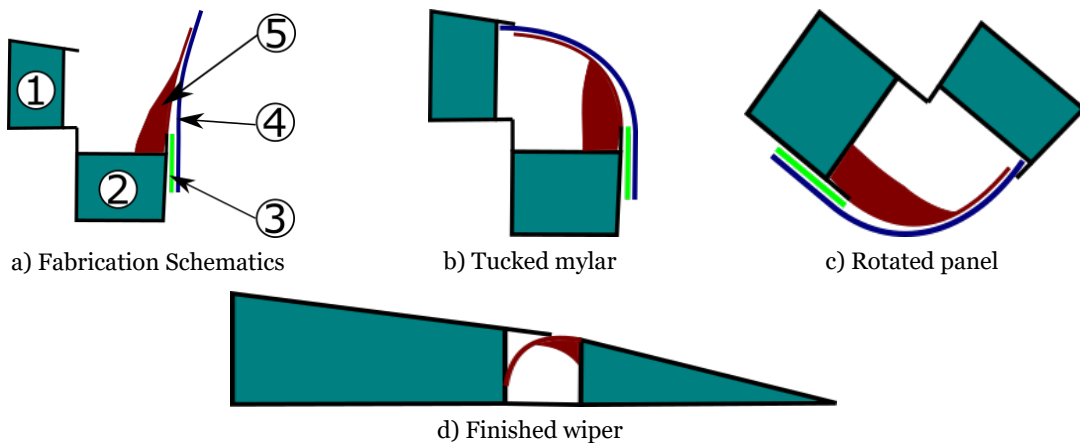


Figure 2.4: Built in wipers manufacture: 1 - TE; 2 - Control surface; 3 - Double sided tape; 4 - Mylar sheet; 5 - Epoxy with micro-balloons mixture.

method is to use a thin film like cassette tape bonded to a thin tape [38, 39]. The procedure is very simple and starts by laying a strip of tape stretched over a bench with the sticky side faced up (Figure 2.5a). The two ends are secured in place with masking tape. The cassette film, with a smaller width, is placed over the regular tape with the non-magnetic side facing down. This is done by aligning both tapes edges, so on one of the regular tape span-wise edge there is not exposed sticky surface. Finally the tapes are applied to the upper skin, the remaining tape sticky area is bonded to the wing skin next to gap so the cassette film covers it (Figure 2.4b). Other thin films like curling ribbon can be used instead of the cassette tape [40].

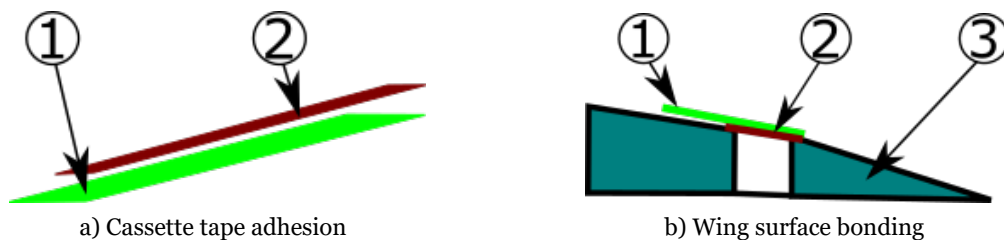


Figure 2.5: Upper wing surface gap seal: 1 - Thin tape; 2 - Cassette tape; 3 - Control surface.

Chapter 3

Experimental Procedure

For the design of a flap/flap-eron device, a plain type was chosen because of the simplicity. Due to small chord thickness of the ACC2019 aerofoil in the flap area and with the goal of introducing the actuation system fully inside the wing to create a clean surface, other more capable flap devices were deemed too complex to install. Also because of budget reasons combined with complexity, for the actuation system a traditional servo motor will be used instead of the more advanced concepts described in the literature review. The remaining of this chapter details the multiple experiments that must be realized in order to retrieve the necessary data for the design of the control surface. The experimental tests conducted were the follow:

- Manufacturing of the specimens for the flexible skin joint;
- Test bench, the assembly and the hardware/software for data acquisition;
- Manufacturing of the Room Temperature Vulcanization (RTV) silicone test subject for upper wing skin;
- Test apparatus to find the silicone's Young's Modulus and Poisson's coefficient;
- Test of a sealant agent as means to bond the rubber and composite skin;
- XFOIL simulation to find the aerodynamic hinge moment.

3.1 Skin Specimens

To create a flexible joint to serve as a control surface hinge, various test subjects were built and tested. The joint skin needs to be flexible enough that regular servo motors can actuate the system mechanism, but offer at the same time adequate structural rigidity.

3.1.1 Design

Skin specimens were designed to represent the trailing edge skin. In order to achieve that, they were divided in two sections, one representing the flap while the other corresponding to the remaining aerofoil. Three different solutions were chosen to work as a joint. Type A (Figure 3.1.1b), the bottom layer is continuous while the inner layer is interrupted with a 5 mm gap. In between these a fibre strip is applied. Type B (Figure 3.1.1c), bottom and inner layer follow the same design as type A, but in this case a fibre strip is not applied and the inner layer gap is reduced to 0.5 mm. Type C (Figure 3.1.1d), both the bottom and inner layers are interrupted with a 5 mm gap and between these, two fibre strips are applied. Each specimen is 250 mm in length, this value was selected because it is 1/3 of the wing panel span of the

model used in ACC2019. This allowed to save material while still being a representative span. In regard to the width, 50 mm was the selected dimension being approximately the same as ACC2019 model flap cord (c_f). For the structure, a sandwich composite was chosen for one of the parts, while the other was a simple composite skin since this part will be clamped to the test bench. This design is faithful to the ACC2019 model. A balsa wood core and two carbon fibre layers, one on each side, were used. Sheets with a weight of 30 g m^{-2} and a $\pm 45^\circ$ orientation fibre were used. As for the balsa wood, 1 mm thick sheets with a density of 200 kg m^{-3} were selected. For type A and C joints, glass and aramid fabrics were selected to

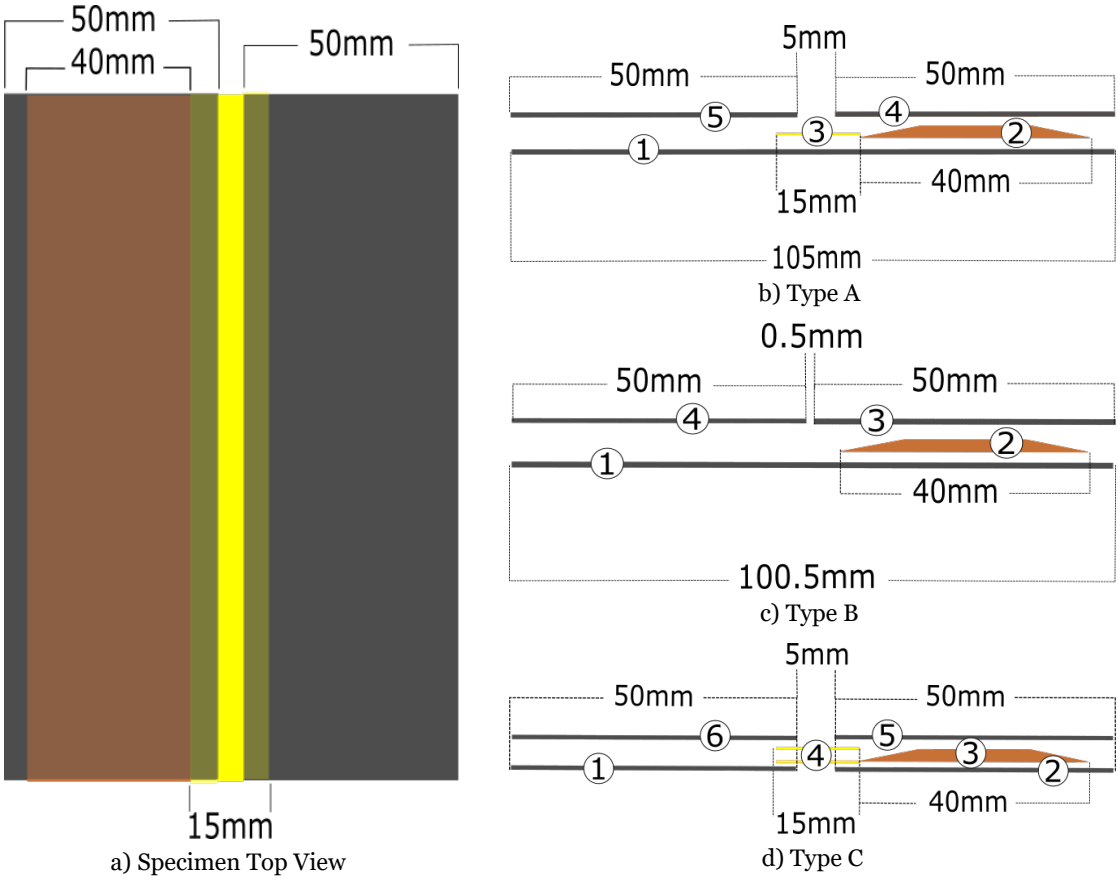


Figure 3.1: Test specimens schematics: Left - Top view; Right - Side view from the 3 different joint types. Numbering represents the order of materials application.

be used as fibre strips between the bottom and inner carbon fibre layers. Six combinations were devised. The table 3.1 illustrates the six specimens and the materials selected. For the glass fibre, a 50 g m^{-2} bidirectional ($0^\circ/90^\circ$) fabric was selected. Also a bidirectional ($0^\circ/90^\circ$) fabric but with 36 g m^{-2} was chosen for the aramid fibre.

3.1.2 Manufacturing

The first step in the manufacturing procedure is to cut fibre sheets and the balsa wood with the required dimensions and then chamfer the balsa edges (10% inclination) in the span direction with sand paper. A glass table was used to laminate the test specimens. A polyvinyl alcohol (PVA) release agent was applied on the surface and left to dry for at least 30 min-

Table 3.1: Specimen characterization.

Specimen	Joint	Fibre layers	Inner layer Gap
1	Type B	None	0.5 mm
2	Type A	1 Aramid	5 mm
3	Type C	2 Aramid	5 mm
4	Type C	2 Glass	5 mm
5	Type C	1 Aramid/1 glass	5 mm
6	Type A	1 Glass	5 mm

utes. Meanwhile the necessary peelply, cotton sheet, breath and vacuum bag to cover the laminate were cut. After checking that the release agent is dry, a two part epoxy resin is prepared. Table 3.2 shows its characteristics. Both parts are weighted according the compo-

Table 3.2: 2 part epoxy resin specifications.

Resin	Hardener	Mixture	Pot life	Curing time
Epoxy Resin L	Hardener W 300	100:35 by weight	300 minutes	24-72 hours

nents data sheet. Usually in the manufacturing of composite laminates, the total resin mass to be prepared is equal to the mass of the fibres that need to be impregnated. Due to previous experience, mainly from ACC2019, it was found that mixing resin with a mass equal to that of the fabric, was not enough to properly impregnate the fibres. A 50% increase in resin mass was established to be the optimal quantity. The two parts were thoroughly blended and then de-gassed in a vacuum chamber to completely remove the air. The remaining manufacturing procedure for both types of joint were as follows:

1. A coat of resin was applied over the glass surface where the fabric sheets would be disposed;
2. For type A and C joints the non-cut carbon fibre sheet was disposed over the resin;
3. A brush was used to gently press and stroke the fibres, so they could soak in the resin. To guarantee proper impregnation, if needed, more resin was applied;
4. For type B joints, one carbon sheet was disposed and then the procedure described in 3 was applied. The second sheet was applied with specified spacing and the process described in 3 was repeated;
5. The bottom side of the balsa wood was coated with resin and applied over the carbon fibre;
6. For type A joint, the single fibre strip was applied. Then the procedure described in 3 was applied;
7. For type C joint, each strip was applied individually. After each application point 3 was repeated;
8. For all configurations, resin was disposed on top of the balsa wood. Then a layer of carbon fibre was applied over it, again bullet point 3 was followed;
9. For both joint types the second inner layer was applied respecting the required spacing. Step 3 was executed one last time.

The peelply, breath bag and cotton sheet were disposed over the laminate in this order. An

adhesive tape was used to bond the vacuum bag to the glass table, but before this was done a hole was cut in the bag, so a vacuum pump extractor could be attached. Then the pump was turned on and the bag was checked for any leaks. In order to achieve proper curing, the laminate was left for 12 hours in the vacuum bag (Figure 3.2).

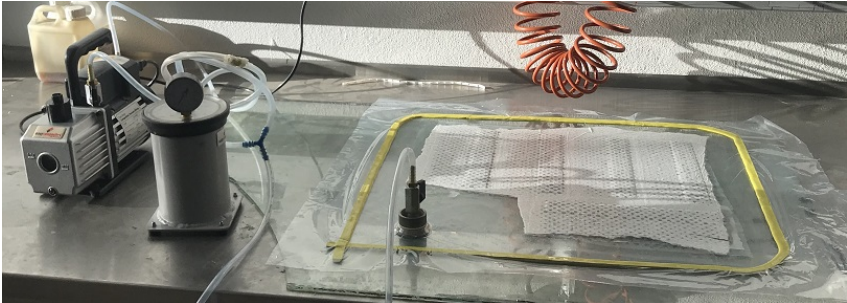


Figure 3.2: Composite specimens curing process.

3.1.3 Test Bench

A test bench was built in order to acquire de necessary data to calculate the hinge moment of the various test specimens. The apparatus is shown in Figure 3.3. The load cell was bolted to a custom designed and laser cut plywood part, which subsequently was glued to 4 linear bearing wheels. Those would slide along 2 aluminium rods that were attached to 4 pillow block bearings. This meant that the load cell could move back and forward parallel to the test bench base. The specimens were secured by the balsa wood free section with the clamp by means of tightening six 3 mm bolts. A protractor was made by means of printing one in a paper sheet and then glued to a piece of plywood.

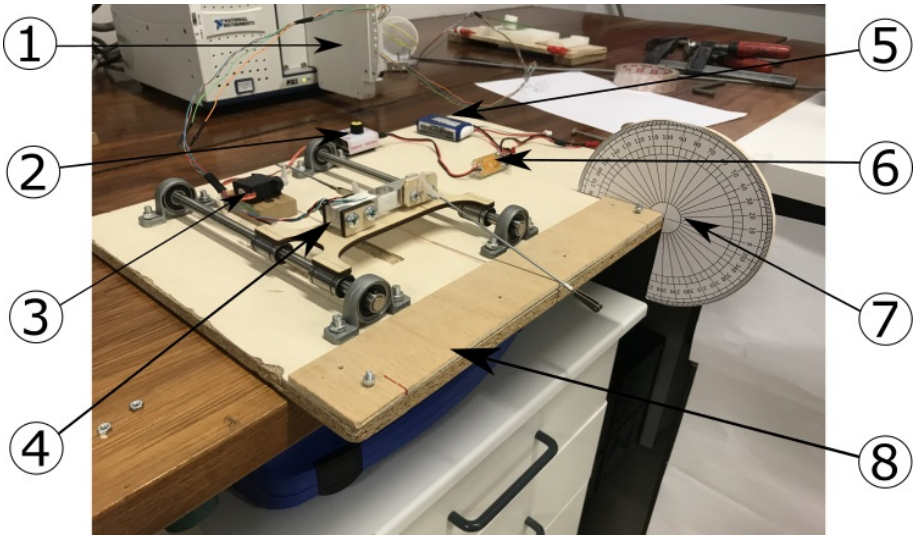


Figure 3.3: Test bench: 1 - Data acquisition board; 2 - Potentiometer; 3 - Servo motor; 4 - Load cell; 5 - LiFe battery; 6 - Battery eliminator circuit (BEC); 7 - Protractor; 8 - Clamp.

A special designed and 3D printed horn, with two holes (Figure 3.4) was screwed to the sandwich section of the specimen. Two marks were drawn on the specimen joints at 3 mm and

5 mm from the sandwich edge (Figure 3.4), in order to analyse the force required to bend the specimens at different joints widths. Due to having various fibres combinations, it is important to study the effect that they have on the resistance to deflection in both positive and negative directions. So, with 6 specimens, 2 horn holes, 2 joint widths and 2 deflection directions a total of 48 tests were performed. Before any test was done, the load cell needed to

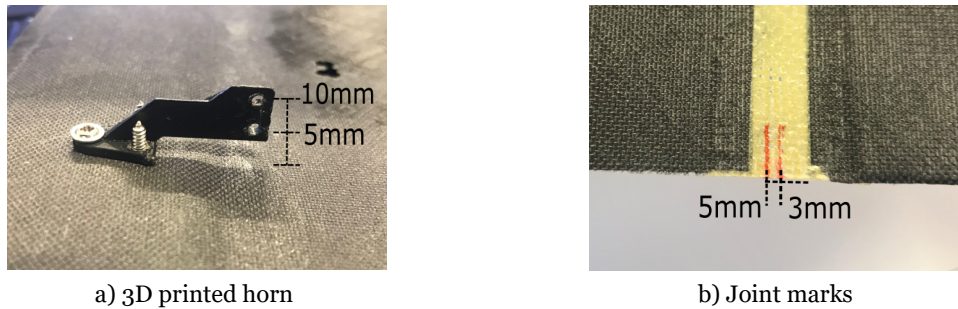


Figure 3.4: Multiple test combinations: a) 2 horn heights; b) 2 joint widths.

be calibrated. That was achieved by connecting the cell to the data acquisition board (NI-TB 4330) and using the commercial software NI LabView 2014. The first step was to create a new Virtual Instrument (VI), then click Right Mouse Button (RMB) on the block diagram, then Measurement I/O, NI-DACmx and insert a DAQ Assist (Figure 3.5). The acquisition signal was selected and then, analogue, force and bridge. The required load cell information was then inserted (Annex A.1). Next a WaveForm graph was introduced by clicking RMB on the VI Front Panel. Then the graph was dragged inside the DAQ Assist on the block diagram. Finally the graph was connected to the "DATA" cell in DAC Assist 3.5. Then the procedure to calibrate the load cell was done. First, by clicking RMB in DAC Assist "DATA" cell and clicking Properties, then calibration, 2 point calibration (linear) and a frequency that needed to be a multiple of 60 Hz was chosen. The first measurement was done without any load and the value 0 was introduced in the "REF" cell for a 0 kg load. The second measurement was done with the maximum load (1 kg), for that a calibration weight was used. Then the value 1 was introduced in the "REF" cell for a 1 kg load and then "next" was pressed to finish the setup.

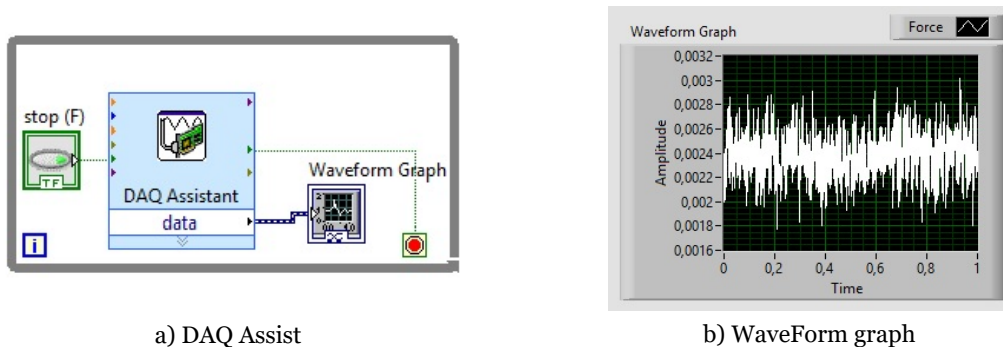


Figure 3.5: LabView VI work environment: a) Block diagram DAQ Assist assembly; b) Front panel WaveForm graph .

Now that the calibration was completed, the specimens experiment could be realized. The created VI in LabView used for calibration was opened and then the test settings were selected by clicking RMB on the DAC Assist "DATA" cell and choosing properties. The setting "continuous samples" was chosen at a 1000 samples per cycle and a refresh rate of 1000 Hz. A Nikon D3100 DSLR camera with an 18-55mm lens was aligned with the specimen trailing edge (Figure 3.6) so the deflection could be monitored using the protractor. Load cell data were read at 5° increments between 0° and 50° for a total of 11 samples. The potentiometer was used to control the servo motor, which in turn pushed the load cell making the specimen deflect. Resistance was offered by the joint while it was being bent and the load cell read that data. After positioning the specimen at the desired angle, both Nikon shutter release control and stop LabView VI continuous sample acquisition were pressed. This way a picture was taken and that second of data was stored in memory. To save the data, RMB was clicked on the WaveForm graph and option export was selected, then the data was copied to clipboard and pasted on a "txt" file. The continuous sample acquisition was started again and the entire process was repeated. In the end, a 50° picture of the joint was taken to analyse the deformation.

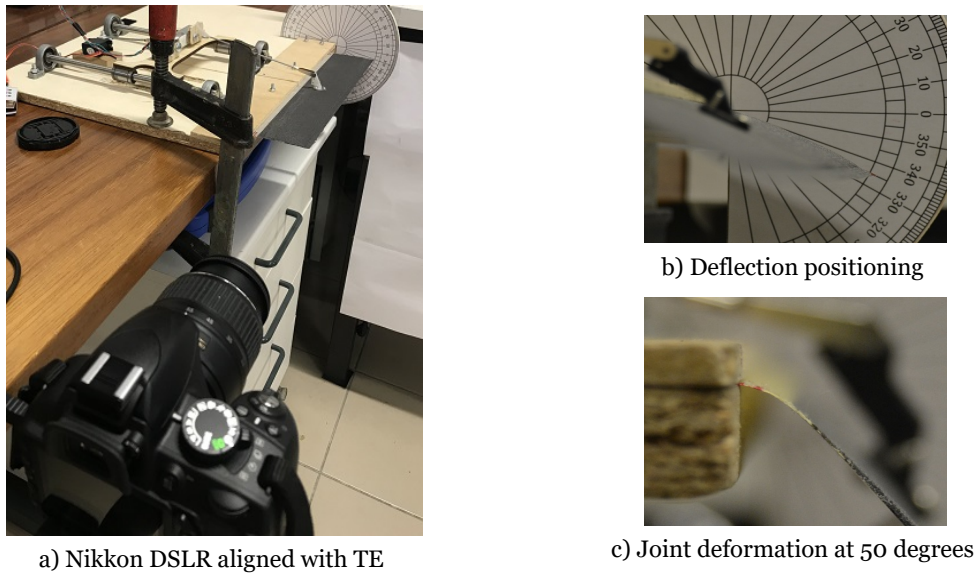


Figure 3.6: Apparatus for specimen deflection monitoring.

3.1.4 Composite Laminate Data Processing

From the testing described in section 3.1.3, data concerning the force read by the load cell at specified deflection was saved. For the purpose of this work, moment at the specimen joint (M_j) needed to be calculated. This was achieved by trigonometry relations through known dimensions. Figure 3.7 shows a test bench schematic with the mentioned relations. Specimen joint moment can be calculated using Equation 3.1.

$$M_j = F_{2t} \times r \quad (3.1)$$

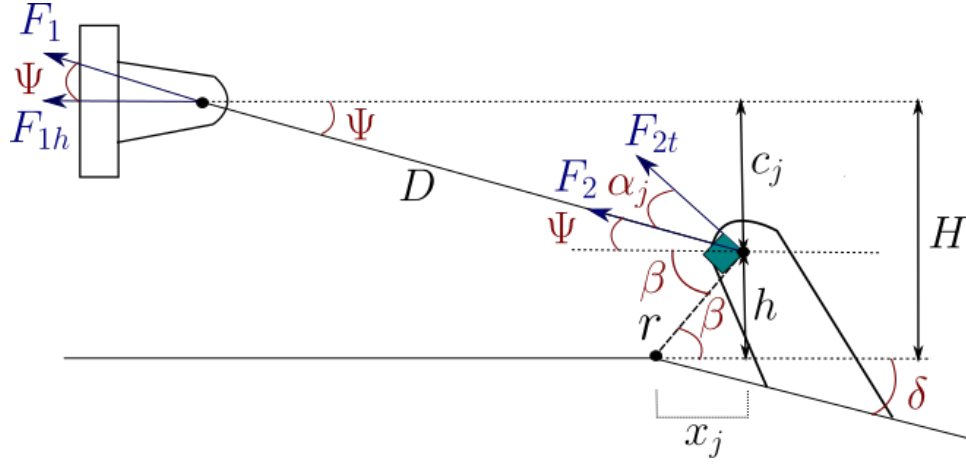


Figure 3.7: Angular relations and forces acting on the specimen.

where F_{2t} is the force perpendicular to the lever's fulcrum and r is the lever arm length. From Figure 3.7 the following equations can be deduced.

$$F_{2t} = \cos \alpha_j \times F_2 \quad (3.2)$$

$$F_1 = \frac{F_{1h}}{\cos \Psi} \quad (3.3)$$

$$F_1 = F_2 \quad (3.4)$$

$$M_j = \cos \alpha_j \left(\frac{F_{1h}}{\cos \Psi} \right) \times r \quad (3.5)$$

In Equation 3.5 the F_{1h} component is the value read by the load cell. For the joint moment to be calculated further relations, between the triangle angles and side lengths, had to be made and are shown bellow. For $\delta = 0$, h_0 , $x_{j,0}$ and β_0 are the reference values.

$$r = \sqrt{h_0^2 + x_{j,0}^2} \quad (3.6)$$

$$\beta_0 = \cos^{-1} \left(\frac{x_{j,0}}{r} \right) \quad (3.7)$$

$$\beta = \beta_0 - \delta \quad (3.8)$$

$$h = \sin \beta \times r \quad (3.9)$$

$$c_j = H - h \quad (3.10)$$

$$\Psi = \sin^{-1} \left(\frac{c_j}{D} \right) \quad (3.11)$$

$$\alpha_j = 90^\circ - \beta - \Psi \quad (3.12)$$

Now before the joint moment can be calculated the propagation of uncertainty needs to be addressed. As in any experimental procedure, where measurements have to be made, uncertainties appear due to limitations, like instruments precision. This in combination with the different variables present, leads to the propagation of those uncertainties. Since for this experiment various measurements had to be done and thanks to multiple equations necessary to calculate the joint moment, the propagation of uncertainty had to be accounted for. To quantify this, formula 3.13 is used [41]. Basically, Z is a function of the independent variables A, B , etc. Absolute error is used to represent those uncertainties ($\sigma_Z, \sigma_A, \sigma_B$).

$$(\sigma_Z)^2 = \left(\frac{\delta Z}{\delta A} \sigma_A \right)^2 + \left(\frac{\delta Z}{\delta B} \sigma_B \right)^2 \dots \quad (3.13)$$

The general formula for propagation of uncertainty is applied to Equations 3.5 through 3.12. The saved data from the load cell was processed with the commercial software Microsoft Excel. The ".txt" files were imported using Power Query and summarized with a PivotTable (Figure 3.8) which averaged the 1000 samples of force data for each deflection. Then in a spreadsheet, Equations 3.5 through 3.12 were implemented with their uncertainty derived formulas. The data measured by the load cell has an associated relative error and is found with Equation 3.14 [42]. Annex A.1 has the load cell properties required for calculation. Load cell data results were then multiplied by the relative error to obtain the absolute one, so it could be combined with the other uncertainties through Equation 3.13.

Row Labels	Average of Amplitude - Force
00.txt	0,00000
05.txt	0,09648
10.txt	0,19198
15.txt	0,27640
20.txt	0,36709
25.txt	0,44879
30.txt	0,54493
35.txt	0,65325
40.txt	0,75683
45.txt	0,84597
50.txt	0,93372

Figure 3.8: Files sample data averaged with a PivotTable.

$$e > \sqrt{e_L^2 + e_H^2 + e_R^2 + \left(\frac{e_z \times L_R \times N}{W_1} \times t \right)^2 + (e_s \times t)^2} \quad (3.14)$$

3.2 Elastomer

Now the upper skin gap of the aerofoil is addressed. Since the flap rotating axis is positioned on the bottom wing skin by means of a flexible composite hinge, this meant that upper skin length (L_f) increases and decreases depending on the flap deflection (Figure 3.9). So, to create a continuous skin that can accommodate this change in dimension an elastic material had to be used. Bubert et al. [43] described the development of a passive elastomeric matrix composite skin to be applied in an span morphing UAV wing tip. The authors found that Room Temperature Vulcanization silicone elastomers were viable as matrix material due to their high elongations at break and low stiffness which reduces the force necessary to actuate the system.

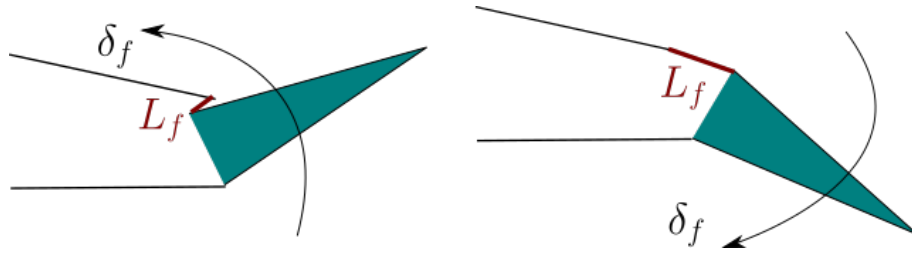


Figure 3.9: Length change in upper skin gap.

This made RTV silicone a prime candidate for the flap upper layer connecting skin. After extensive research, was found that vendors do not indicate the elastomers Young's Modulus, this represented a challenge because this property is necessary to calculate the force required to deform the material. A property that vendors provide is the hardness (Shore A or D), A. N. Gent [44] described a correlation between elastomers hardness and Young's Modulus, although not highly accurate, equation 3.15 gives a good first approximation.

$$E = \frac{0.0981(56 + 7.62336 \times S)}{0.137505(254 - 2.54 \times S)} \quad (3.15)$$

where E and S are Young's Modulus and Shore A hardness, respectively. After market research, CS25 Condensation Cure Silicone Rubber (Easy Composites Ltd.) was the chosen product for further testing. The silicone properties are shown in Table 3.3.

Table 3.3: RTV silicone rubber properties at 25°C.

Property	Result	Units
Density	1.04-1.14	g cm^{-3}
Hardness	23-27	Shore A
Tensile Strength	3.8-4.2	MPa
Tear Strength	15-20	kN m^{-1}
Elongation at break	500-550	%
Viscosity	20000-26000	mPa s
Mix ratio	100:5	Parts
Pot Life	60-90	Minutes
De-mould time	24	Hours

3.2.1 RTV Silicone Testing

Due to the lack of a proper elastomer testing machine, an experimental procedure had to be devised. ASTM D412 [45] describes the standard test methods for vulcanized rubber and thermoplastic elastomers. For dumbbell test specimens these are marked with a bench marker and then placed on the testing machine grips. Then the specimen is elongated at a constant rate and the distance between marks and force are measured at the desired elongations and at rupture. To calculate the stress at any given elongation, Equation 3.16 is used.

$$\sigma = \frac{F}{A} \quad (3.16)$$

where σ , F and A are the stress and force at the specified elongation and the specimen unstrained cross-section, respectively. After a force is applied to a material, the deformation that occurs in response to that is called strain (ε) and it is calculated using Equation 3.17.

$$\varepsilon = \frac{\Delta L}{L} \quad (3.17)$$

where ΔL and L are the change in length and initial distance between marks, respectively. Strain is a dimensionless number. If deformation is not too large an elastic material like rubber can stretch and then return to its original form without sustaining permanent strain. This is called elastic deformation. At this stage linear behaviour occurs and the Young's or Elasticity Modulus (E) can be used and is expressed by Equation 3.18.

$$E = \frac{\sigma}{\varepsilon} \quad (3.18)$$

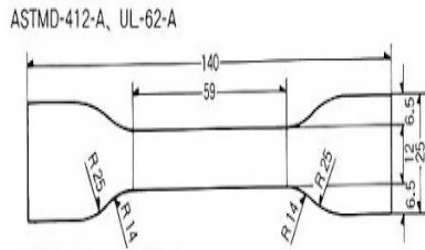
A material's Young's modulus is extracted by first plotting a stress/strain curve, then a linear regression of the elastic deformation data is done. This gives an equation of the $y=ax+b$ type, where E is the slope (a).

3.2.2 Dumbbell Specimen

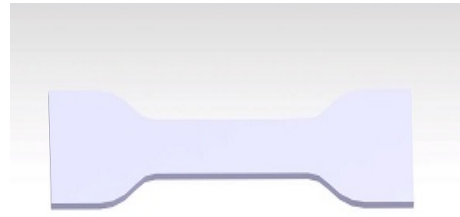
ASTM D412 describes six different sizes of dumbbells specimen. For the purpose of this work, type A die (Figure 3.10) was the chosen one. They should be made either by mould injecting or cut from a sheet, at least 1.3 mm thick. The lack of moulds or die cutters meant that an alternative had to be found. It was decided that a 2 mm elastomer sheet was to be manufactured and the specimen laser cut. To achieve that, a mould was designed in a commercial Computer Assisted Design (CAD) program (CATIA V5). Also, a type A die was designed according to ASTM D412 dimensions.

Top view drawings were created for the laser cutting machine (Annex A.2). A 2 mm thick acrylic sheet was cut to be used as mould. For the base a glass table was utilized. The elastomer specimen manufacturing procedure is described below:

1. The glass surface was properly cleaned and then a PVA release agent was applied;
2. Both acrylic mould parts were coated with PVA and left to dry for 30 minutes;



a) ASTM D412 Die A dimensions



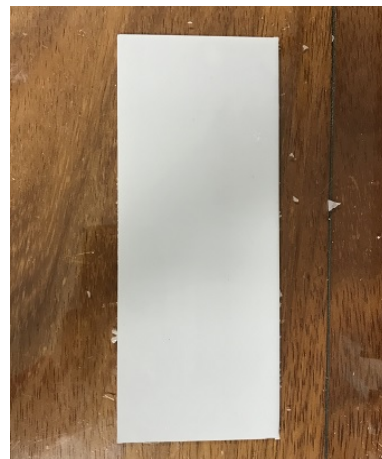
b) CATIA V5 Die A part

Figure 3.10: ASTM Die A part design for laser cutting.

3. After dried, the mould was positioned on the glass table;
4. Both parts of the RTV silicone are weighted in the specified proportions. Total mass is calculated given mould volume and mixture specific mass;
5. The components were mixed in a container with 5 times the mixture volume and then stirred vigorously until an homogenous solution was achieved;
6. Excess air was then removed with the help of a vacuum chamber;
7. Then the mixture was poured into the mould and spread with the aid of a spatula. Any excess of silicone that may had poured over the extremities was cleaned;
8. Mould's top cover was applied slowly while checking if there was not any air gaps;
9. Weights were added on top and they needed to reach the mould edges so the acrylic top did not bend (Figure 3.11a);
10. After 24 hours curing time the elastomer sheet was removed from the mould (Figure 3.11b).



a) Weights pressing the mould



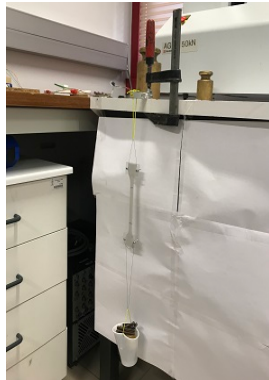
b) Cured elastomer sheet

Figure 3.11: Elastomer sheet for specimen laser cutting.

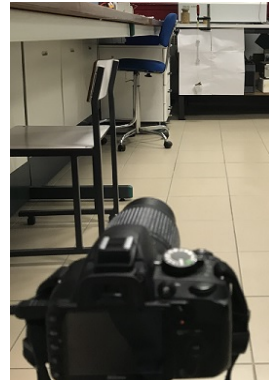
Elastomer sheet was stored for a week to finish curing and reach maximum properties. After that, the specimen was laser cut using the 3D die A part drawings. Then markers were drawn and specimen width and thickness measured with a caliper.

3.2.3 Photometry

Photometry was chosen as a novel way of measure the specimen elongation. As for the force, a 5 kgf (YZC-133) rated load cell was used. Both specimen extremities were clamped by means of two acrylic pieces tightened by two bolts. One end was secured to the load cell and the other to a bucket that was hanged with the purpose of adding weight (Figure 3.12). Across the room a Nikon DSLR camera with a 55-210mm telephoto lens was stationed. The settings were manually set and kept the same trough the experiment.



a) Force data acquisition



b) Nikon D3100 DSLR camera

Figure 3.12: Elastomer testing: a) Apparatus for reading and saving force data; b) Camera/lens combo for specimen marks photos to posteriori calculate elongation.

At the beginning, a reference photo was taken and the marks distance were measured with a caliper so the pixel size could be later determined. The goal was to add mass, to the bucket, in increments and at each one, a photo of the specimen was taken and the force data was saved. The NITB-4330 data acquisition board and LabView 2014 software were again used. For load cell calibration and acquiring data procedure refer to section 3.1.3. The photos were then passed through an image processing program written for the effect. Here, the distance between marks were measured and the strain calculated using the reference photo and the L length.

3.2.4 Image and Data Processing Program

Here the image processing program is described. First, the user is required to introduce the reference values (A, L_i), then the images naming scheme and the quantity to import is written for the "for" cycle. As each image is being imported they are separated in three planes (RGB), then the plane where the specimen marks exhibit larger contrast is chosen for thresholding (Figure 3.13). The contrast levels are adjusted in the chosen plane until satisfactory results are reached while the others are kept at zero. Both planes are then converted into binary and a final image is done by the sum of these.

In the next step, the final binary image is inverted and any hole is filled. Now the image is structured by using lines with a chosen size and angle. A command is used to detect the number of objects in the image and another to find the desired property, in this case, its centroid.

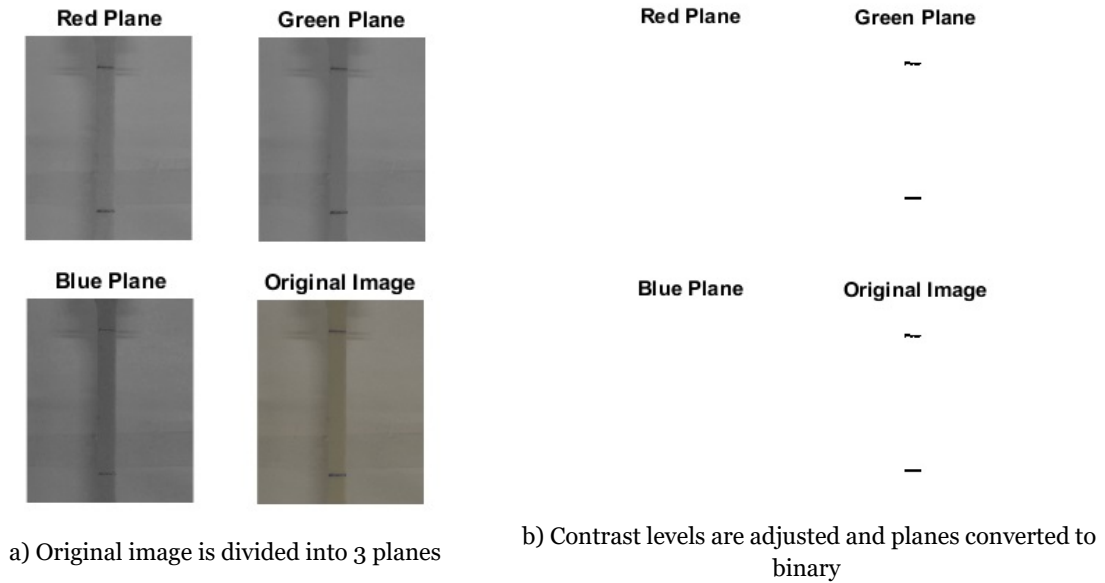


Figure 3.13: Original image is processed so the specimen marks are isolated in a binary image.

Those are then positioned over the original image to check proper correlation (Figure 3.14). Centroids data are then extracted to a vector and the distance between these is calculated and stored in another one. Pixel size is determined by dividing the marks distance from reference photo (pixels) with L . Marks distance vector is converted to metric by multiplying with the pixel size.

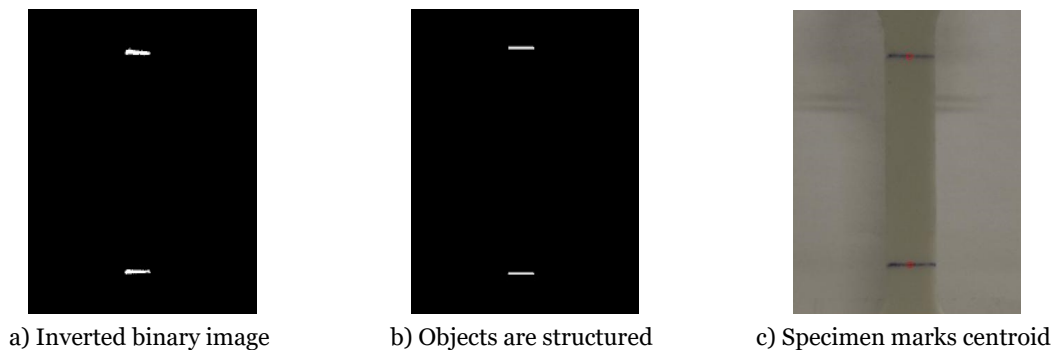


Figure 3.14: Binary image objects are cleaned and their centroid found.

A ".txt" file with the force data measured by the load cell is imported and stored into a vector. Stress and strain are then calculated using Equations 3.16 and 3.17, respectively. Finally, a chart is drawn using stress and strain vectors, and a linear regression from the data is also drawn, where the slope (a) is the Young's Modulus (E).

3.2.5 Elastomer Bonding Agent

To close the upper wing gap, a suitable way to bond the elastomer to composite skin, one that is also able to withstand the loads resulting from stretching the rubber had to be found. Silicone is known for their poorly adhering capabilities to other materials so finding a good candidate was not an easy task. Different agents were tested: epoxy glue; cyanoacrylate;

contact glue; hot glue. All shared a common characteristic, after being glued to a carbon fibre laminate and cured, they separated right way when handled, making it impossible to realize any testing, proving the inability of these agents to work as a solution. Bubert et al. [43] for his elastomer skin, tested 2 agents to work as an adhesive, both silicone based. So for further testing, a silicone acetate for wet rooms (Würth International AG) was chosen (Annex A.1). To test the adhesive capabilities a lap shear test was devised. Silicone strips were cut from the remaining sheet used for the Die A specimens and glued to the rough side of a carbon fiber laminate. This was done by spreading a thin layer of sealant over the laminate and then pressing the strips onto it. Table 3.4 shows specimen dimensions.

Table 3.4: Silicone sealant adhesion test specimen dimensions.

Specimen	Length [mm]	Width [mm]	Thickness [mm]
1	23.80	7.20	2.05
2	27.05	10.20	2.05
3	27.05	10.45	2.05
4	23.35	7.90	2.05
5	23.35	10.20	2.05
6	23.50	6.10	2.05
7	23.50	5.75	2.05

After 48 hours the specimens were checked and showed promising results, now further testing could be done. The 5 kgf load cell was used for this test due to being already calibrated and configured. The only changed setting was the number of samples to 5000. This meant that continuous 5 second data samples were generated. The free end of the specimen was attached to the load cell with the acrylic pieces used in section 3.2.3, while the laminate was pulled by hand. The experiment procedure started by initiating de LabView VI data acquisition. When a new sample started the laminate was pulled continuously until failure in the bonding was achieved. Then the data acquisition was immediately stopped to keep information in memory. Data was saved using the same method described in section 3.1.3.

3.2.6 Aerodynamic Hinge Moment

For the actuation system design, three main hinge moments had to be considered, the composite skin joint resistance to bending, the elastomer force acting at the hinge while stretching and the hinge moment resulting from aerodynamic load. Previous testing enabled the calculation of the former two, leaving the latter to be obtained. That was achieved using XFOIL, an aerofoil analyses software developed by Mark Drela [46]. XFOIL can predict various aerofoil parameters, in this case the hinge moment coefficient (C_{he}). For that, an aerofoil design tool allows the addition of a control surface at the desired location. The procedure is very simple and is described bellow:

1. A "txt" file with the aerofoil coordinates is loaded using the command "load" followed by the file name including the extension;
2. GDES command is used to open the aerofoil design routine;
3. A trailing edge flap is created using the "flap" command;

4. First the flap hinge "x" location is chosen by aerofoil chord fraction;
5. Then hinge "y" location is chosen by specifying the "y" on function of the thickness;
6. Desired flap deflection, in degrees, is selected;
7. "Exec" command is used to set the buffer aerofoil to current (Figure 3.15);
8. In XFOIL main menu "ppar" command is used to set the panelling parameters;
9. Number of nodes was set to 300 and TE/LE panel density ratio to 0.5;
10. Again in XFOIL main menu, "oper" command is chosen to initiate the operation;
11. "V" is introduced to select viscous mode, Reynolds and Mach number are introduced;
12. The number of iterations is set to 100 and the angle of attack (α) is chosen initiating the operation;
13. After converging the "FMOM" command is used to give the hinge moment per unit of span (H^{bar}).

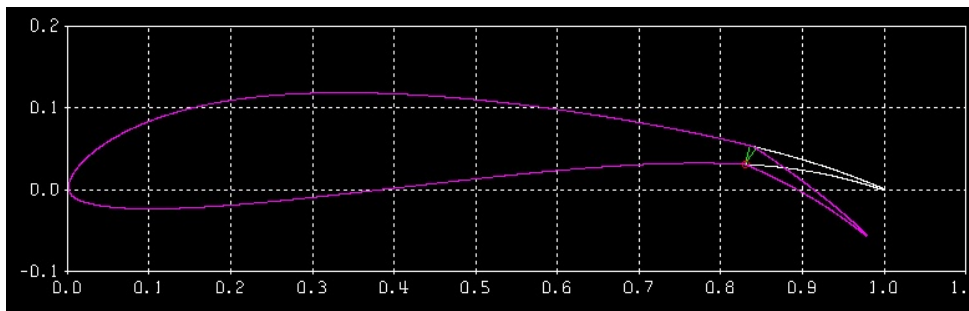


Figure 3.15: Geometry design routine: Purple - New airfoil with 20° trailing edge flap; White - NewACC2017 aerofoil.

XFOIL gives the hinge moment coefficient value through the Equation 3.19.

$$H^{bar} = C_{he} \frac{1}{2} \rho_{\infty} V_{\infty}^2 \quad (3.19)$$

where ρ_{∞} and V_{∞} are the free stream density and speed, respectively. With this equation the hinge moment resulting from aerodynamic load can be calculated. ACC2019 aircraft had an average maximum speed of 17 m s^{-1} . For the purpose of these simulations a maximum of 20 m s^{-1} airspeed was chosen. Flap deflection was changed from -50° to 50° in 5° increments. The angle of attack was the same through all the simulations ($\alpha = 0$). An important issue that also needed addressing was the elastomer behaviour during flight when experiences suction due to negative C_p and pressure due positive C_p . After each simulation the C_p versus x/c data points were saved in a "txt" file to be used in further analyses.

Chapter 4

Flap Design, Manufacturing and Validation

4.1 Flap Design

In this section, the data gathered previously is used as guide to design a flap system. As for the remaining aerofoil, ACC2019 central wing panel design was used. For the purpose of this project and as a means of comparison, it was decided that the panel was going to have a span equal to the ACC2019 aircraft (745 mm). A first draft was done to have an idea of the components positioning and interactions with each other. Another consideration was the project maximum flap deflection, ACC2019 aircraft had 3 flap positions, 8° for take-off, 16° for landing and -8° for cruising. For a greater margin and since the flap system is also expected to function as a flaperon, both positive and negative deflection of 20° was chosen for this project. Table 4.1 summarizes the design specifications.

Table 4.1: Flap design specifications.

Aerofoil	cord	Hinge position	Positive deflection	Negative deflection
NewACC2017	0.3 m	0.83 x/c	20°	20°

4.1.1 Elastomer Skin Sizing

Sizing the elastomer sheet is important because of the impact that it has on the actuation system. As seen in Figure 3.9, flap deflection stretches the silicone. As this happens, the resistance offered by the elastomer causes a moment, which needs to be overcome, on the joint. So first step was to figure how much the silicone stretches as flap deflects. For that, CATIA V5 part design of ACC2019 central panel was used to obtain the necessary reference dimensions at 83% chord (Figure 4.1). This is important because the required force to stretch the silicone is strain dependent as shown in Equation 4.1 deduced from Equations 3.18, 3.16 and 3.17.

$$F = E \times A \times \frac{\Delta L}{L} \quad (4.1)$$

One end of the elastomer sheet is bonded to the flap section at the maximum negative position (P_i) while the other is bonded to the main panel (P_l). When under no load the sheet has a length of (L_i) and at a neutral flap position (P_{ref}) it has a L_0 length. For any flap deflection applied, the change in position is called P_f and the sheet length L_f . This produces a variation in length ($\Delta L = L_f - L_i$). To know the positions of all points, a Cartesian reference system with origin at P_0 , the flap rotation axis, is drawn. So P_{ref} is at position ($0 : r$). P_l depends on of the chosen elastomer length for neutral position (L_0) and the angle ϕ (12,6°). In this

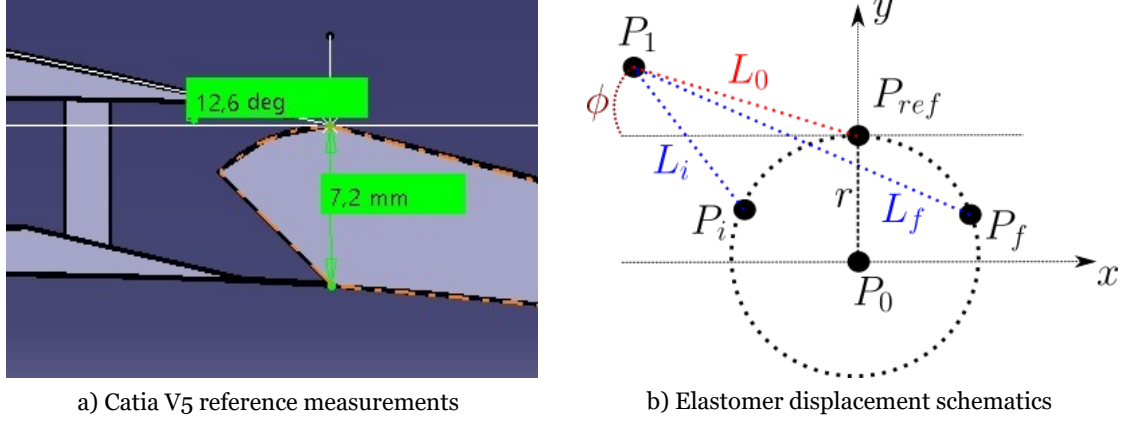


Figure 4.1: Elastomer bonding position calculation based on flap deflection.

aerofoil section at this scale and for simplicity reasons, P_1 is positioned in a straight line tangent to the wing's upper skin TE. Various L_0 values were attributed to predict different strains. Equations 4.2 and 4.3 are used to calculate the coordinates of P_1 .

$$P_{1,x} = \cos(180 - \phi) \times L_0 + P_{ref,x} \quad (4.2)$$

$$P_{1,y} = \sin(180 - \phi) \times L_0 + P_{ref,y} \quad (4.3)$$

where $P_{1,x}$ and $P_{1,y}$ are the x and y coordinates, respectively. Similarly $P_{ref,x}$ and $P_{ref,y}$ are the coordinates of P_{ref} . Since the coordinates of P_f changes along a circumference of radius r , its new position is calculated with equations 4.4 and 4.5.

$$P_{f,x} = \cos(90 - \delta f) \times r \quad (4.4)$$

$$P_{f,y} = \sin(90 - \delta f) \times r \quad (4.5)$$

Now ΔL can be found, first by calculating the distance between two points, using Equation 4.6, to give L_f and then subtracted L_i .

$$L_f = \sqrt{(P_{f,x} - P_{1,x})^2 + (P_{f,y} - P_{1,y})^2} \quad (4.6)$$

Cross-section area (A) is another characteristic, by looking to Equation 4.1, that affects the required force to strain the elastomer. As the span has a fixed length, sheet thickness is the remaining dimension to be optimized that affects the cross-section area. For force calculations, Equations 4.1 through 4.6 were implemented in an Excel spreadsheet, L_0 was given values from 5 mm to 25 mm in 5 mm increments and sheet thickness was varied from 0.1 mm to 1 mm in 0.1 mm increments. As stated previously the flap deflection will vary from its bonded position at -20° to its maximum deflection of 20° for strain calculations. Now the joint moment resulting from the elastomer (M_e) force needs to be calculated. To better understand the mechanics of this, refer to Figure 4.2, where the angular relations and force vectors can

be observed. Also the necessary equations can be deduced and are shown below.

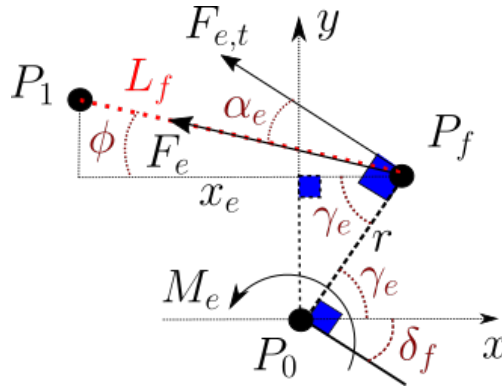


Figure 4.2: Elastomer joint moment schematics.

$$M_e = F_e \cos \alpha_e r \quad (4.7)$$

$$\alpha_e = 90 - \gamma_e - \phi \quad (4.8)$$

$$\gamma_e = 90 - \delta_f \quad (4.9)$$

$$\phi = \cos^{-1} \left(\frac{x_e}{L_f} \right) \quad (4.10)$$

where $F_{e,t}$ is the perpendicular component to the lever's r the distance between P_f and P_0 , x_e is the x axis distance between $P_{f,x}$ and $P_{1,x}$, ϕ is the angle formed by the radius r and x_e . From the results obtained (section 5.4) it became clear that to minimize the elastomer impact on the actuation system a low thickness and/or larger L_0 is required. Since the silicone rubber is an elastic material, a large L_0 is not advised due to the possible deformation that can occur thanks to out of plane pressure differentials. So the goal is to make the elastomer sheet as thin as possible.

A testing procedure was done to evaluate how thin it is possible to manufacture a elastomer sheet. For the mould, a car headlight protecting film made of polyethylene terephthalate (PET) with a 0.2 ± 0.05 mm thickness was chosen. Thinner products that could be used as a mould were difficult to find and 0.2 mm was a good compromise. A glass table was used as base, then a film section was cut and glued to the table, after that a square was removed so the silicone could be poured in the middle. Refer to section 3.2.2 for the two part RTV silicone manufacturing. After curing, the elastomer was torn up during the de-moulding process showing the thickness was too small. In the next test two layers of film were staked together for a total of 0.4 ± 0.1 mm and another batch of rubber was prepared. This time after curing the silicone sheet was successfully removed, making this thickness viable. For a thickness of 0.4 mm, L_0 from 5 mm to 15 mm was not a option due to high hinge torque requirements. For

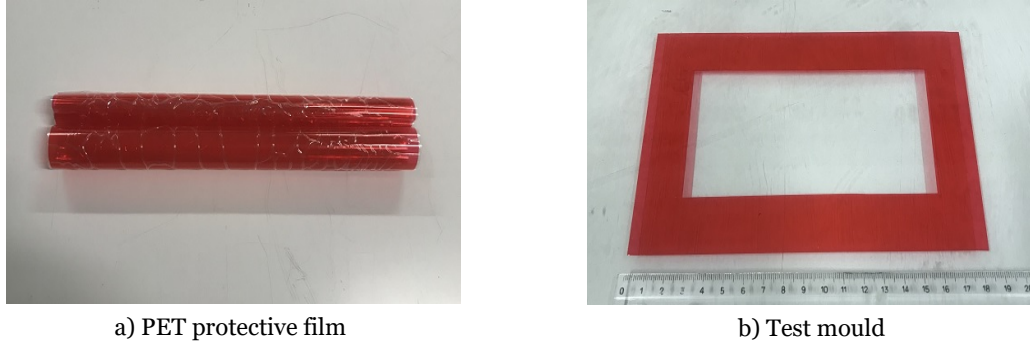


Figure 4.3: Elastomer's sheet thickness manufacture testing.

example, ACC2019 aircraft wing panel span measured 745 mm and for the actuation system each panel used a servo motor with a rated torque of 0.265 N m. An equal span panel using an elastomer sheet with a 15 mm L_0 would have a predicted hinge torque of 0.451 N m and it still needed to take into account the flexible laminate joint and the aerodynamic forces. So L_0 of 20 mm to 25 mm is a more practical measurement to avoid a large increase in servo motor rated torque, since their weight and power requirements also increase leading to added mass. Larger L_0 would decrease the loads but as previously mentioned, the elastic nature of the silicone in combination with the airflow pressure and lower tension could lead to aerofoil shape deformation.

Due to the mentioned above, it becomes important to study the aerodynamic effect on the elastomer sheet. This is when the C_p curves saved from XFOIL aerofoil analyses done in section 3.2.6 come into play. Commercial software Ansys 18.2 was chosen for the task in hand. The first step, was to find the x/c location of the elastomer sheet extremities for both deflections, so the force by unit of span resulting from aerodynamic pressure in the elastomer location could be calculated with Equation 4.11.

$$\frac{F}{Span} = c^2 \int_{\frac{x_1}{c}}^{\frac{x_2}{c}} C_p(x) \frac{dx}{c} \frac{1}{2} \rho_\infty V_\infty^2 + P_\infty \quad (4.11)$$

That was accomplished by finding the flap hinge location in millimetres, then using Equations 4.4 and 4.2 to find the x coordinate of P_f and P_1 x , and consequently their LE distance in millimetres for both deflections. Next, the LE distance was divided by the chord length to convert to x/c . This was done to L_0 lengths of 20 and 25 millimetres. Table 4.2 shows the referred positions. Then, a polynomial fit was performed to the saved data from section

Table 4.2: P_f and P_1 x coordinate in relation P_0 and their x/c position.

Point	x coord.	LE distance	x/c position
P_0	0 mm	249 mm	0.83
P_f at $20^\circ \delta_f$	2.46 mm	251.46 mm	0.84
P_f at $-20^\circ \delta_f$	-2.46 mm	246.54 mm	0.82
P_1 at 20 mm L_0	-19.52 mm	229.48 mm	0.76
P_1 at 25 mm L_0	-24.34 mm	224.66 mm	0.75

3.2.6. This was done for both -20° and 20° deflections, at the elastomer location. The upper surface data for 20° was divided into two trendlines for a better correlation due to a spike at the hinge location. With the polynomial fits, the elastomer boundaries in Table 4.2 and

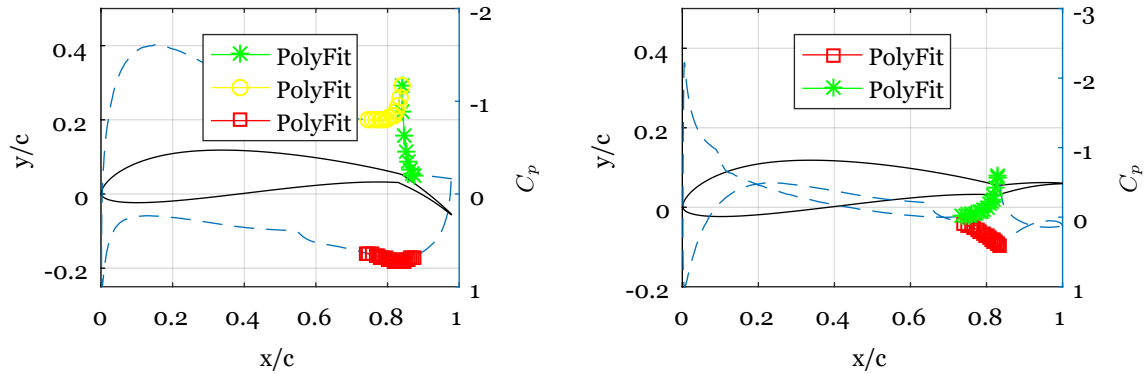


Figure 4.4: Aerofoil C_p distribution: left - positive deflection; right - negative deflection. Blue dashed line is the C_p curve.

Equation 4.11, the force by unit of span acting over the elastomer sheet was calculated. With this data a FEM analysis could now be performed in Ansys. To predict how much the sheet was going to deform, two small sections with 10 mm span and $P_1 - P_f$ chord were designed. Two analysis needed to be conducted, minimum and maximum deflection, for each section for a total of 4. At minimum deflection there was not any strain, so only the aerodynamic load would be acting. For maximum deflection, on top of the aerodynamic load, the material would be stretched (ΔL). The Ansys test parameters are shown in Table 4.3. The process

Table 4.3: Ansys static structural analyses parameters.

Test	L_0	Deflection	Section [$l \times L_i$]	Thickness	ΔL	Force [N]
1	20 mm	-20°	10×17.72 mm	0.4 mm	0 mm	-0.0047
2	20 mm	20°	10×17.72 mm	0.4 mm	4.78 mm	0.0274
3	25 mm	-20°	10×22.71 mm	0.4 mm	0 mm	-0.0049
4	25 mm	20°	10×22.71 mm	0.4 mm	4.79 mm	0.0304

used to perform the tests in Ansys is described below:

1. A material library module was dragged to the workbench and the RTV silicone was created with its mechanical properties;
2. Then a mechanical model module was added and the material cells were connected between the two modules;
3. The section is designed as a surface so it is analysed with shell elements to save time and computational resources. Desinger module was the used tool;
4. In the model branch of the work tree, the sheet thickness and material were selected;
5. The mesh was done by first selecting edge sizing with RMB in the mesh branch of the work tree and choosing a 0.4 mm element size, applied at the 4 edges. This value is chosen because it is the sheet thickness and leads to a better mesh quality (Figure 4.5);

6. Again in the mesh branch with RMB, a face meshing was selected with quadrilateral elements. Then the mesh was created;
7. In the workbench, a static structural module was placed and the model cell was connected to the model cell of the model module;
8. Now the remaining parameters were introduced, first the boundaries. For test 1 and 3, the edges received a fixed support and the force was applied normal to the sheet surface;
9. Test 2 and 4, one of the edges received a fixed support, but on the other a displacement equal to ΔL was applied. Again the force was normal to the surface;
10. Now the remaining parameters regarding the solver were chosen. Those are indicated in Table 4.4. The remaining options stayed as standard;
11. Finally, the output options were selected. For this case, the directional deformation in the y axis and the equivalent stress (Von-mises).

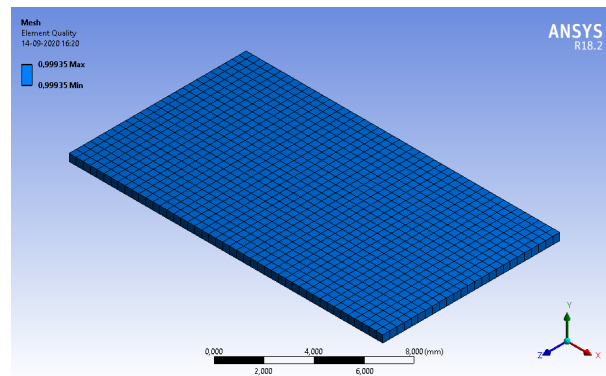


Figure 4.5: Ansys mechanical displaying the mesh's element quality for test 1.

Table 4.4: Solver control options

Solver Controls		Step Controls		Non-linear Controls	
Large deflection	ON	Auto-Time Stepping	ON	Newton-Raphson Option	Full
—	—	Define by	Substeps	Line Search	ON
—	—	Initial Substeps	30	—	—
—	—	Minimum Substeps	30	—	—
—	—	Maximum Substeps	100	—	—

With the results from Ansys static structural analysis (section 5.6), it was observed that the elastomer sheet deformation due to the pressure differential was small, specially at positive deflection. Meaning that any of the two options for L_0 was acceptable. The 25 mm one has the benefit of requiring less servo torque to stretch but in comparison with the 20 mm one, it suffers a little more deformation. A final decision regarding this matter will be made after the actuation system design.

4.1.2 Flexible Laminate Joint

Now a flexible skin joint needs to be chosen. The silicone sheet sizing showed the significant impact that the elastomer has on the required actuation forces. So to minimize further power requirements, the laminate design that required less torque to bend was chosen, which was specimen 1. The calculated torque required to deflect 20° was added to the elastomer's one

and the aerodynamic hinge moment (M_H) for that same deflection (Equation 4.12). With the full torque actuating over the hinge calculated, the next step is to dimension the actuation system.

$$M_T = M_j + M_e + M_H \quad (4.12)$$

4.1.3 Actuation System

Flap actuation is done by means of a servo motor, which pushes or pulls a rod connected to a horn mounted in the flap. Servo motors have a rated torque (M_s), but depending on how the system is mounted that may never fully transmitted to the joint ($M_{h,s}$). For a better understanding how the system works, Figure 4.6 provides a visual representation of how the force is applied. If friction is neglected in the servo and horn joints, Equations 4.13 and 4.14 can be deduced.

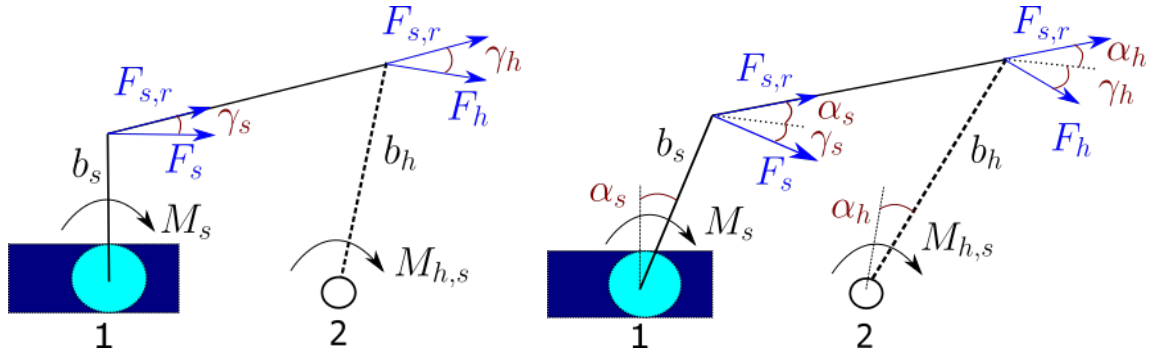


Figure 4.6: Force application schematics of a servo actuation system: 1 - Servo motor; 2 - Flap hinge.

$$M_{h,s} = M_s \frac{b_h}{b_s} \cos(\gamma_s + \alpha_s) \cos(\gamma_h + \alpha_h) \quad (4.13)$$

where γ_s and γ_h are the angle of the control rod to the perpendicular to the moment arm. As for α_s and α_h , they are the rotation of the servo and horn arm, respectively, and

$$\alpha_h = \alpha_s \frac{b_h}{b_s} \quad (4.14)$$

By inspecting them, it becomes clear that to increase the servo hinge moment, the flap horn lever needs to be greater than the servo one. Although this reduces the flap rotation angle. This posed a challenge due to the goal of having the actuation system inside the wing panel to reduce drag, specially combined with limited interior height near the TE. It is also noted that as the servo and hinge rotates, the angles (α_s) and (α_h) increase. Looking at Equation 4.13 it can be concluded that this results in a lower hinge moment $M_{h,s}$. With this in mind and to optimize the servo torque, one way is to have $\alpha_s = \alpha_h = 0$ at 20° flap deflection, when the hinge experiences its maximum load due to the elastomer strain, flexible joint bending and aerodynamic forces. Another way to take full advantage of the servo torque is to keep the $\frac{b_h}{b_s}$ ratio at a minimum of 1. Space inside the panel at hinge location comes at a premium with

around 7 mm of height between surfaces. Taking that into account plus the skin thickness and the horn dimensions, realistically the lever will not be greater than 5 mm, so b_h equal to 5 mm was adopted. Now to keep the levers ratio at a minimum of 1, b_h needs to be at maximum 5 mm and ideally even less. But due to physical limitations 5 mm is as close, it will get to the servo rotation. So b_s equal to 5 mm was chosen.

As the available hinge torque changes depending on the system dimensions, connecting locations and the actuation mechanism itself, the need to have a tool that can predict this becomes critical for the design process. With the information acquired in this section a program in Matlab was created. Figure 4.7 shows the relations schematics necessary to write the code.

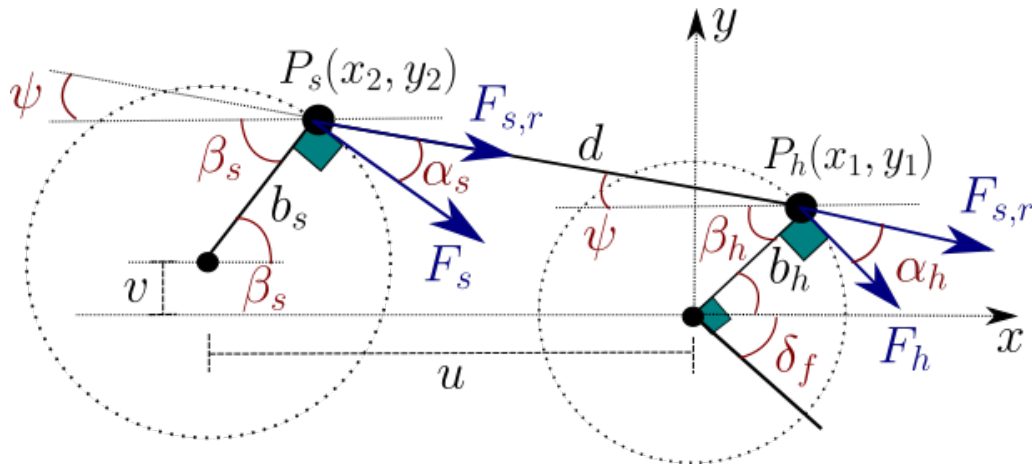


Figure 4.7: Diagram: Angular and force relationships between both circular movements, dependent on flap deflection.

The program code is in Annex A.3 and its operation is described bellow:

1. First the initial parameters are introduced ($b_s, b_h, \beta_{h,ref}, u, v, d, M_s, \delta_f$ range and $\delta_{f,stp}$);
2. A "for cycle" starts from minimum to maximum deflection with $\delta_{f,stp}$ increments;
3. Calculates β_h using Equation 4.15 and initiates a counter so the results for each deflection step are stored in a array;
4. Solves a four Equations (4.16 - 4.19) and four unknowns system to find P_s location in relation to P_h , giving its coordinates. Equation 4.20 functions as a restriction equation and forces only one solution from the system instead of two;
5. It calculates β_s and ψ based on P_h and P_s coordinates and rod length (d);
6. Finds α_h and α_s using the relations found in Figure 4.7;
7. Torque at the hinge is calculated with equation 4.13.

$$\beta_h = \beta_{h,ref} - \delta_f \quad (4.15)$$

$$P_{h,x1} = \cos \beta_h b_h \quad (4.16)$$

$$P_{h,y1} = \sin \beta_h b_h \quad (4.17)$$

$$(P_{s,x} - u)^2 + (P_{s,y} - v)^2 = b_s^2 \quad (4.18)$$

$$d = \sqrt{(P_{s,x} - P_{h,x})^2 + (P_{s,y} - P_{h,y})^2} \quad (4.19)$$

$$P_{s,y} > v \quad (4.20)$$

A plot with the available hinge torque at each deflection step is drawn, also a plot that illustrates the circular movement (Figure 4.8) is drawn to help visualize the actuation system and if the program worked as expected. As both levers are equal in length and their rotation

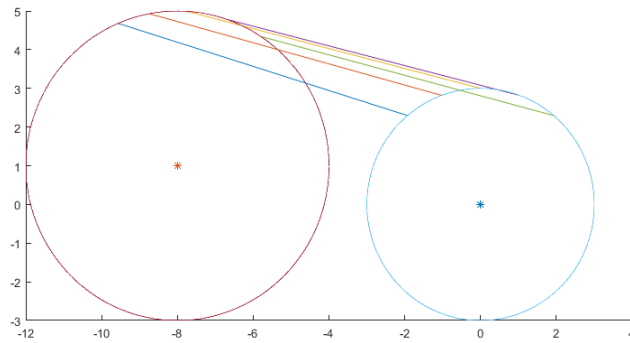
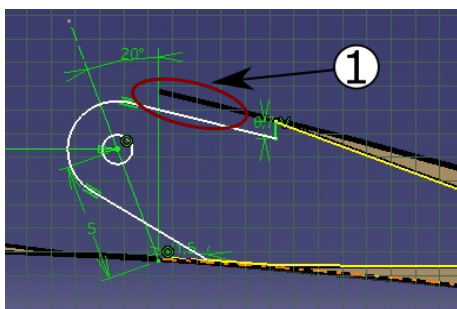
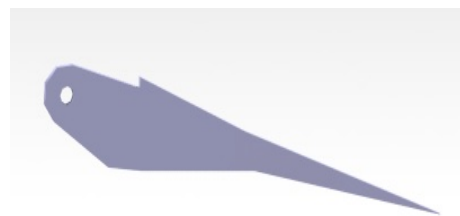


Figure 4.8: Plot illustrating the change in position.

axis will be over the x axis, with the described program help, was found that to maximize the available hinge torque, both alpha angles need to be 0° at maximum flap deflection, in this case 20° . In order to achieve that, $\beta_{h,ref}$ and β_s angles needed to be 110° . With this conclusion in mind, the flap horn was designed in CATIA V5 (Figure 4.9). Its edges were made to coincide with flap skin laminate so actuation forces can be transmitted. At the front end where the rod is connected, there is a gap (0.7 mm) between the top portion and the carbon laminate so the elastomer sheet can be bonded.



a) Sketch



b) 3D rendering

Figure 4.9: Flap horn CATIA V5 part design: 1 - 7 mm gap for the elastomer sheet bonding.

Then the last step was to position the servo motor inside the CATIA V5 panel design. It will be fixed in the bottom surface between the main and trailing edge spar, while respecting the purpose parameters and adjusting the rod length (Figure 4.10). Now that the available

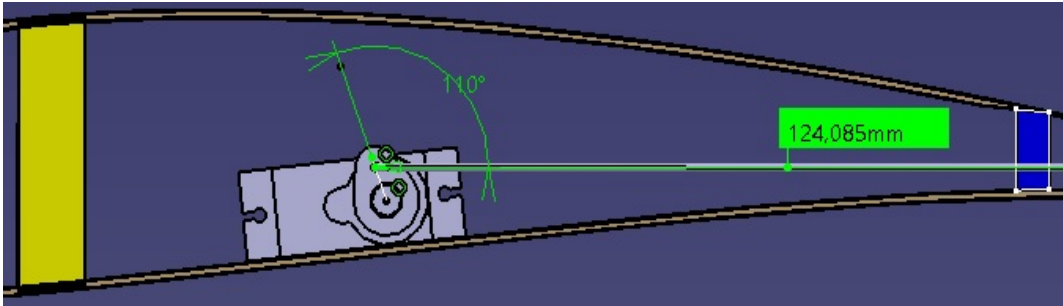


Figure 4.10: Servo motor position and rod length determination.

servo torque at the hinge can be calculated and also the total moment resulting from the joint laminate flexural rigidity, elastomer strain and the aerodynamic load that needs to be overcome at the hinge is known, L_0 will be chosen. This was done by first researching various servo motors and their respective rated torque, then using that data to plot the available torque at the hinge using the MatLab program described above against the total moment (M_T) for both L_0 possible dimensions. Table 4.5 has the researched servos specifications. With the results obtained (section 5.7), only one servo motor has the rated torque required

Table 4.5: Servos specifications.

Model	Operating Voltage [V]	Stall Torque [kgf cm]	Mass [g]
Corona DS-939MG	4.8/6.0	2.5/2.7	12.5
Corona DS-238MG	4.8/6.0	4.0/4.6	22
Corona DS-236MG	4.8/6.0	6.0/7.0	27

for maximum deflection for both L_0 lengths. The second larger torque rated servo barely meets the requirements for $L_0 = 20$ mm. Since it is better to leave a operating safety margin, the corona DS-236MG is the only viable option with a sizeable margin for both values of L_0 . The smaller L_0 with 20 mm was chosen as the project dimension since it suffers less deformation due to aerodynamic pressure.

Now the elastomer sheet was designed in CATIA V5 with the selected dimensions. TE and flap spars were also designed, they both will face the silicone sheet edges. Finally a support for the elastomer was designed, so when the flap deflects, the sheet keeps a curvature in the rotation area and also to protect the silicone from being punctured by the horn. The elastomer part design was achieved by defining a 20 mm distance between the flap LE and the wing upper skin TE (Figure 4.11a). A 25 mm distance was enforced between the flap LE and the wing upper skin TE balsa wood core, to create a 5 mm surface area to bond the sheet (Figure 4.11a). As for the TE spar, like it was referred, faces the sheet edge and its positioned vertical parallel to the part design z axis and its 5 mm wide. Both bottom and top coincide with the inner carbon layers (Figure 4.11b). Likewise the flap spar also faces the elastomer edge and is placed vertically parallel to the z axis and is 5 mm wide (Figure 4.11c). For last,

the elastomer support was placed between the silicone sheet and the flap horn. The former followed the latter curvature (Figure 4.11d).

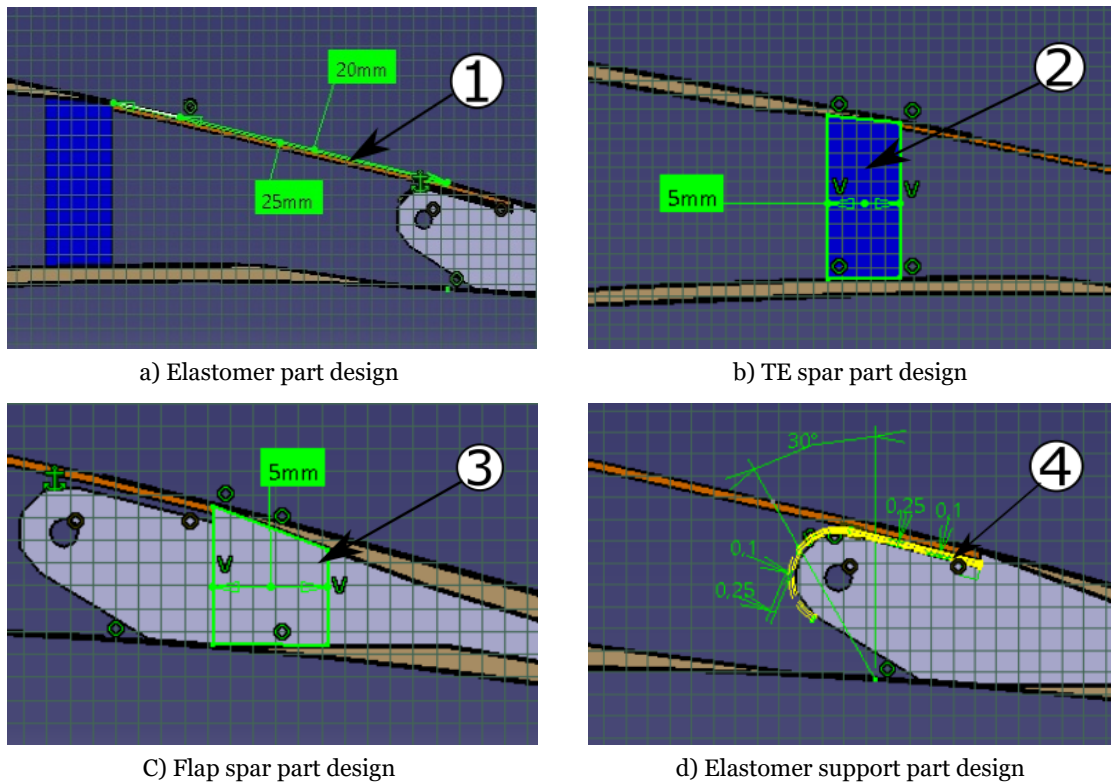


Figure 4.11: Catia V5 part design of the remaining flap components: 1 - Elastomer sheet; 2 - Wing TE spar; 3 - Flap spar; 4 - Elastomer support.

4.2 Manufacturing

This section details the manufacturing procedure for a panel section. ACC2019 wing panels had a span of 745 mm and the project of this flap system used that dimension as reference, but for the purpose of a demonstrator and since the hinge torque scales linearly with the span, a smaller panel with 250 mm of span was deemed adequate. Not only would, be easier and quicker to manufacture but also, require less material.

4.2.1 Upper/Bottom Skins

The first step of the process was to manufacture the bottom and upper skins. They consist mainly of a sandwich structure with one layer of carbon fibre on each side and a balsa wood core. Before any manufacturing could be done, preparations were needed. First the parts position in relation to the LE were measured in the panel CAD design and were marked onto the mould. Now the manufacturing materials were prepared, the carbon fibre layers and balsa sheets were cut, then the balsa wood was chamfered, finally the carbon fibre strips for the spar caps were also cut, a 80 g m^{-2} unidirectional was used. All materials had a larger length than the 250 mm span to make a longer panel section that could be trimmed later. Figure

4.12 shows the materials arrangement and Table 4.6 indicates the respective dimensions for the bottom skin.

Table 4.6: Manufacturing materials dimensions.

Material	Length [mm]	Width [mm]	Chamfers LE/TE [mm]
Ext. carbon layer	270	350	
Int. carbon layer A	270	285	
Int. carbon layer B	270	65	
Spar caps	280	10	10/10
Balsa sheet A	300	65.3	10/—
Balsa sheet B	300	100	—/10
Balsa sheet C	300	76.3	10/10
Flap balsa sheet	300	36.6	10/15

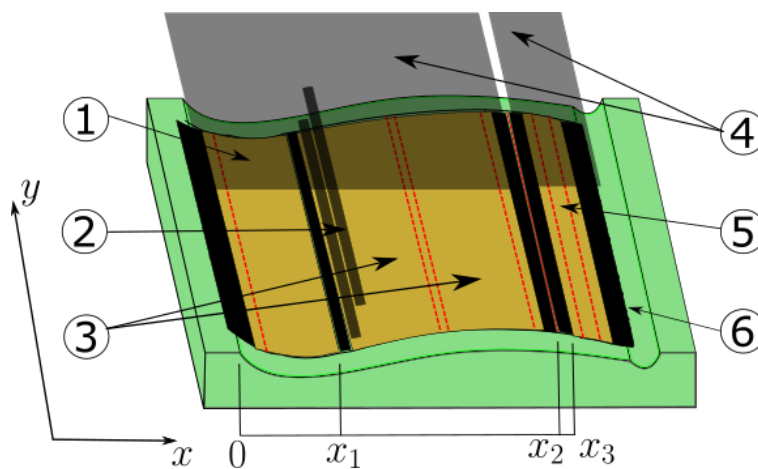


Figure 4.12: Bottom shell manufacture: 1 - Balsa sheet A; 2 - Carbon strips; 3 - Balsa sheets B and C; 4 - Interior carbon layer A and B fabrics; 5 - Flap balsa sheet; 6 - Exterior carbon layer; x_1 - 69.5 mm; x_2 - 249 mm; x_3 - 254 mm. Red dashed lines represent the chamfer zones.

As for the procedure, it was the same used for ACC2019 model and is described below:

1. A PVA release agent coat was applied to the mould and left to dry. Meanwhile the peelply, punctured bag and cotton sheet were cut;
2. A 2 part epoxy resin was prepared according the supplier specifications;
3. With the help of a paint roller the mould was coated with resin. Then the exterior carbon layer was applied starting from the middle and moving towards the LE and TE. Again the roller was used to guarantee proper fibre impregnation;
4. The balsa sheet A was resin coated on the bottom and applied aligned with the spar caps marks. Then the extremities were hot glued to the mould for fixation;
5. The balsa sheet was pressed for a few minutes until adhering with the carbon;
6. The carbon strips were then applied 1 by 1 between the spar caps marks facing balsa sheet A. At each application it was guaranteed that the strips were properly embedded with resin;
7. The B and C balsa wood sheets were also coated with resin in the bottom an then applied, sheet B facing the carbon strips and C aligned with B chamfers. Extremities were also hot

- glued to the mould;
8. The flap's balsa sheet was applied aligned with its mark following the same procedure as the others sheets;
 9. Balsa's wood top was coated with resin using the roller;
 10. The fabric of the interior carbon layer A was applied, starting from the interruption mark and continuing in, direction to the leading edge. Proper fibre impregnation was checked;
 11. Fabric B was then applied, also starting from the interruption mark, but keeping a 0.5 mm gap between both parts and in, direction to the trailing edge. All the laminated area was pressed with the paint roller;
 12. Peeply was applied followed by the punctured bag and then the cotton sheet. The mould was then inserted in a vacuum bag;
 13. The vacuum pump was then turned on and the bag was checked for any leaks.

Upper skin manufacturing is similar to the lower, so the procedure described above was used. The main difference is the interior carbon layer is continuous instead of being divided in two parts. This meant that the mould did not need a interruption mark. Like for the lower layer skin, the materials arrangement and dimensions are displayed in Figure 4.13 and Table 4.7.

Table 4.7: Manufacturing materials dimensions.

Material	Length [mm]	Width [mm]	Chamfers LE/TE [mm]
Ext. carbon layer	270	350	
Int. carbon layer	270	350	
Spar caps	280	10	10/10
Balsa sheet A	300	68.5	10/-
Balsa sheet B	300	100	-/10
Balsa sheet C	300	56.8	10/10
Flap balsa sheet	300	38	10/15

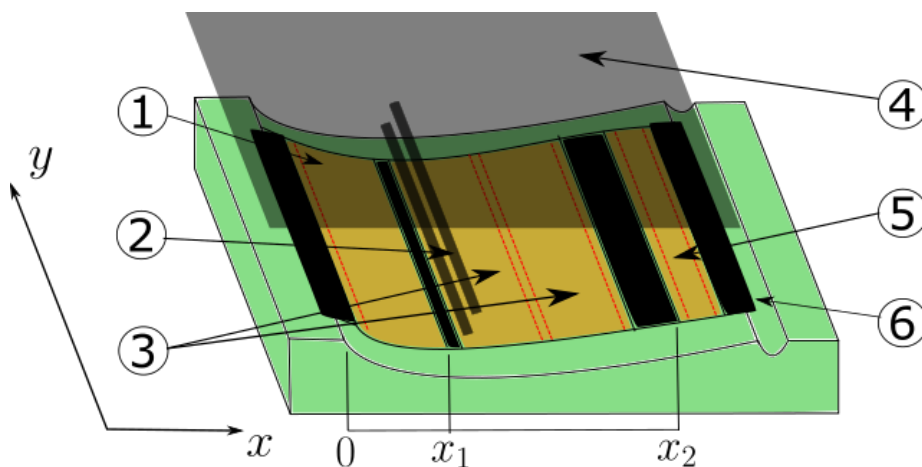


Figure 4.13: Upper shell manufacture: 1 - Balsa sheet A; 2 - Carbon strips; 3 - Balsa sheets B and C; 4 - Interior carbon layer; 5 - Flap balsa sheet; 6 - Exterior carbon layer; x_1 - 69.5 mm; x_2 - 249 mm. Red dashed lines represent the chamfer zones.

4.2.2 Elastomer Sheet

The elastomer will be used to unite the flap to the upper wing shell. The silicone sheet manufacturing process is described in this section and is as follows:

1. The glass table surface was clean and then the 2 layers of PET protective film were applied. An snap-off cutter was used to cut the internal mould dimensions;
2. A PVA release agent was applied to the mould;
3. The two part RTV silicone components were weighted and then mix in a 5 times larger than mix volume container;
4. The silicone was vigorously mix until it was homogenous. Then the container was placed inside a vacuum chamber to de-gauss;
5. The mixture was then poured into the mould and a spatula used to properly spread the silicone. Any excess that flowed over the mould boundaries was cleaned;
6. An acrylic sheet was carefully placed over the mould. It was make sure that there wasn't any air bubbles;
7. In the end weights were placed on top of the acrylic sheet. These needed to settle over the mould so the acrylic didn't bend;
8. After 24 hours of curing the elastomer sheet was de-moulded.



Figure 4.14: Elastomer curing process: Weights pressing a acrylic plate over the mould.

Now that the elastomer sheet was fabricated, its going to be bonded. First, the upper skin needs to be cut. To achieve this, the precise location needed to be known, a CATIA V5 drawing with the top view of the upper shell containing the elastomer edges was printed. The elastomer is going to be bonded so its unstrained when flap deflection is -20° . So this could be done the flap was deflected -20° in CATIA V5 part design and a new part to serve as mould was designed (Annex A.2). A foam block was cut with hot wire using the designed part to serve as the physical mould. Now the remaining procedure is described bellow:

1. After curing the upper shell was removed from its mould;
2. The printed drawing was fixed with tape in the external layer (Figure 4.15a);
3. The skin was placed over the foam male mould for better placement and a snap-off cutter was used for cutting;
4. The two resulting parts were aligned in the foam female mould and fixed with tape (Figure

- 4.15b);
5. The parts were marked to align the elastomer edges during placement;
 6. The silicone sealant was applied with a spatula and spread uniformly within the marks boundaries;
 7. The elastomer sheet cut with the project dimensions was disposed, aligned with the marks and gently pressed against the sealant (Figure 4.15c);
 8. The shell was positioned so the elastomer sheet was not pulling in the bonding area. It was left curing for 48 hours.

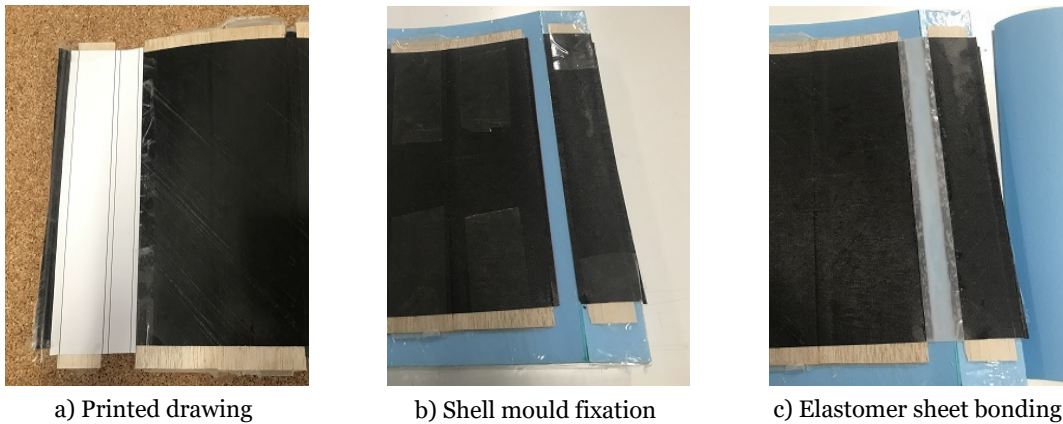


Figure 4.15: Elastomer upper shell bonding: a) Top view drawing with the cutting marks; b) Upper shell parts fixation in the 20° flap deflection mould; c) Bonding between the elastomer sheet and the upper shell with the silicone sealant.

4.2.3 Jig and Assembly

In this section the remaining manufacture process and parts assembly are detailed. To achieve this, a means to position all the required parts and components was necessary, that is where a jig came into play. The CATIA V5 wing panel part design was used to draw a plate (Figure 4.16a) where one of its sides contours the bottom shell inner layer and embraces the mould. Then incisions were drawn to position important parts like the leading edge closing laminate, main spar, trailing edge and flap spar. After completing the plates design, they were fabricated with 4 mm plywood by laser cutting. Then the jig was assembled using wood beams and small triangular feet were used for better support (Figure 4.16b).

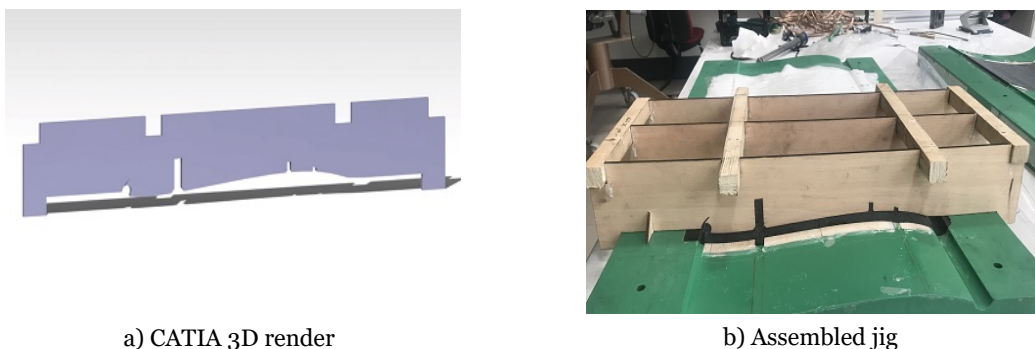


Figure 4.16: Jig design and manufacture.

The servo bay required a reinforcement plate with supports to fixate the servo motor, these were laser cut from a laminate sheet with the same structure as the skin sandwich using the ACC2019 CAD design (Figure 4.17). The next step was to manufacture the flap horn, using the CAD part design, two parts were laser cut from a 4 mm plywood then the head portion was removed. To connect the rod, a servo motor horn was cut and sandwiched between both plywood parts and epoxy glue bonded them together. Initially the idea was to use the plywood horn but the rod fixation area was too thin and was breaking apart.

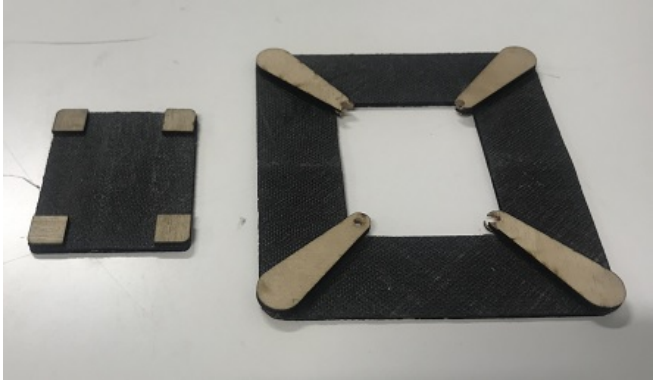


Figure 4.17: Servo bay: Left - Servo mount; Right - Reinforcement plate.

A leading edge closing laminate (LECL) needed to be manufactured as a means to close the skins leading edge. For that a LE male foam mould was made with hot wire (Figure 4.18), then the LECL was done with two carbon fibre layers, the same fabric used in the skins. As for the spars, the main one was cut to size from a spare one from ACC2019 since it was the same design. The remaining spars were cut from Airex foam with a margin from the project dimensions.



Figure 4.18: Shells LE closing laminate manufacture and main spar.

Having all the required parts, the wing panel closing procedure and final assembly could be started and was as follows:

1. The already cut closed to dimension spars, were continuously sand paper and checked if already fitted in their respective incisions, until they did;

2. The spars and LECL were positioned in the jig (Figure 4.20a);
3. A 2 part epoxy resin with micro-balloons was prepared as bonding agent, then with a spatula the mixture was applied to the mentioned parts (Figure 4.20b);
4. The jig was put in position over the mould and weights were added to press it down (Figure 4.20c);
5. After 24 hours of curing the jig was removed leaving the parts in there respective positions;
6. The flap horn was then glued into position with the rod already connected;
7. A cut was made in the trailing edge spar so the rod could pass through;
8. The servo bay reinforcement plate was bonded with a 2 part epoxy glue. A printed CATIA V5 top view drawing was used for placement;
9. The upper shell was positioned in its mould and fixed with tape;
10. The elastomer support was bonded using the silicone sealant (Figure 4.20d);
11. The moulds were closed to check the shells fitting and the spars were sand paper if needed;
12. Again an epoxy resin with micro-balloons was prepared and applied to the spars top, skins LE/TE and to the upper skin areas where the spars connected (Figure 4.20e);
13. The moulds were then closed and clamps were used to press them against each other;
14. After 24 hours curing the moulds were open, but before that the adhesive tapes were removed through the sides with a pliers;
15. Then with the already closed panel the servo bay was cut with the help of CATIA V5 drawing for reference. A safety margin was used and then the edges were sand paper until they faced the internal reinforcement plate (Figure 4.20f);
16. The panel was then marked to the specified dimensions and mounted in a jig. First, the excess sandwich laminate was cut with a rotary tool and then sand paper to span length (Figure 4.20g);

The manufactured panel section is presented in Figure 4.19.

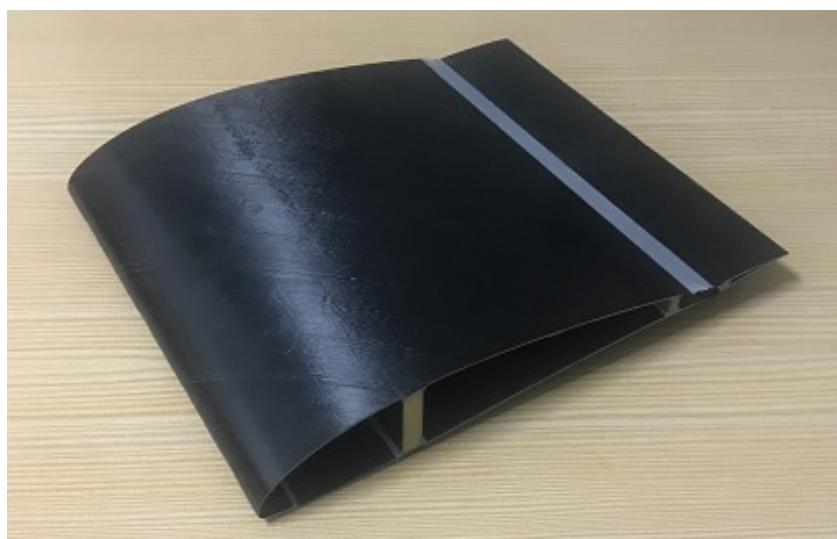
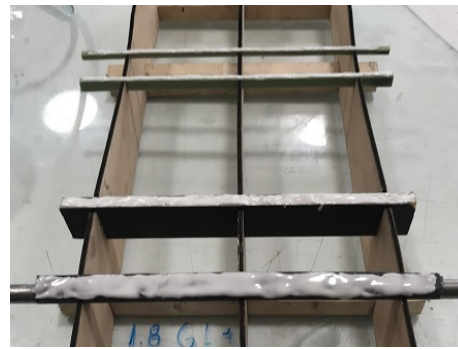


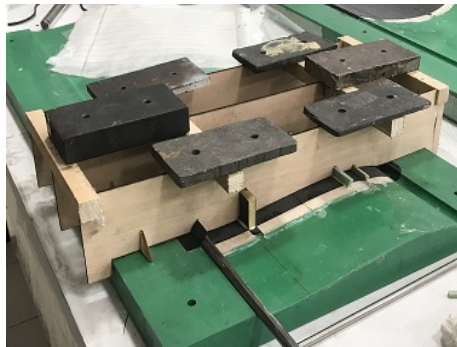
Figure 4.19: Finished panel section.



a)



b)



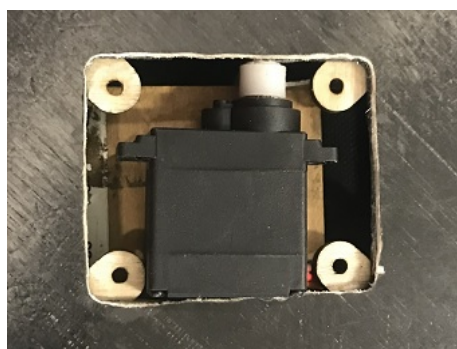
c)



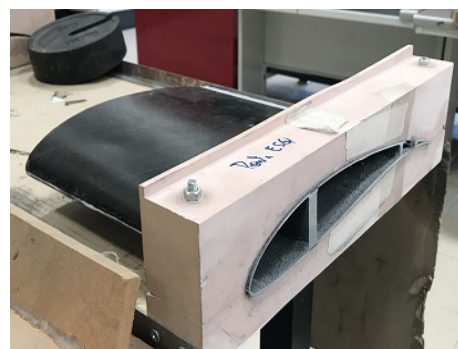
d)



e)



f)



g)

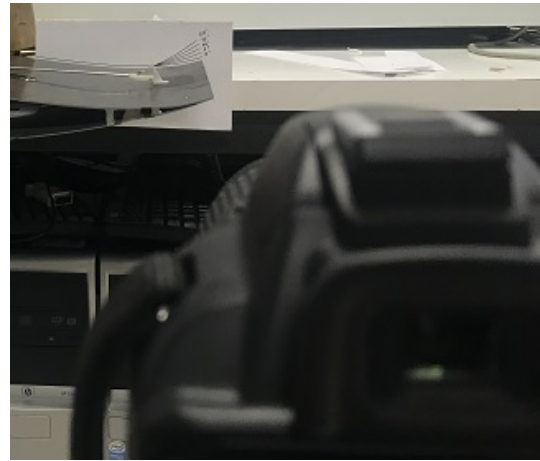
Figure 4.20: Panel assembly procedure: a) LECL and spars trimming and positioning; b) Epoxy resin with micro-balloons application; c) Parts adhesion to bottom shell; d) Elastomer support bonding to upper shell; e) Epoxy resin with micro-balloons application to upper and bottom shells for panel closing; f) Servo bay opening; g) Panel cutting and trimming.

4.3 Flap Validation

In this section an experimental procedure is described as a means to validate the flap system. Along this work various experiments were conducted and the retrieved data in association with the employed methodology, enabled the design of a flap mechanism. Now the built demonstrator will be tested so a comparison between the projected and final product can be realised. A similar experiment to the flexible joint laminates one was chosen. The test bench used in that one was retrofitted to receive the built flap. Due to the difficulty of connecting the load cell to the internal rod, the connection had to be made from the outside. To achieve that a new horn was bonded in bottom flap skin in a way that it would be symmetrical to the interior horn connection hole. A CAD drawing was done with flap deflection marks from 0° to 20° in 5° increments, so with the help of DSLR camera the flap could be positioned at the desired angles to collect data. For testing, a 5 kgf load cell was used and the flap was secured into place with metal rods, weights and clamps (Figure 4.21). As for the data acquisition procedure itself, refer to section 3.1.3, as it was the same.



a) Test bench



b) DSLR Camera alignment

Figure 4.21: Flap test procedure.

Chapter 5

Results

In this chapter previous experiments results are shown. This data was not only necessary for the flap system design but also gives a baseline for future works or projects. First, the composite laminate specimens results are presented, followed by the elastomer Young's Modulus determination. The shear stress tests for the silicone sealant are then presented. Next, the hinge moment resulting from the aerodynamic forces over the control surface, calculated with XFOIL, are presented. Then, the hinge moment results from the elastomer sheet and the deformation resulting from the airflow pressure acting over the elastomer are displayed. With all the moments calculated, the necessary actuation system torque is found and compared with different servo motors and their hinge available torque. Finally the built concept experimental hinge moment results are compared with the predicted ones based on the used methodology.

5.1 Composite Laminate Specimens

Specimen test results are divided in two categories. In the first category, each specimen behaviour is analysed regarding all the different test parameters. In the other, specimens are compared to each other in the various test parameters.

For specimen 1 only four variations were done instead of eight. This was due to having only one continuous carbon layer while the other was interrupted, which caused the specimen to bend on that line. So testing a 3 or 5 millimetres wide joint was trivial. In Figure 5.1 for the same horn height, the results were similar for both positive and negative deflections. This was expected due to the laminate construction being composed of two carbon layers, one continuous and another interrupted, so the necessary torque to bend in both directions is expected to be the same. Specimens 3 and 4 as fabrication goes, are also made with two layers of the same fabric. So the same behaviour as specimen 1 was expected. Figures 5.3 and 5.4 show that for the same pairs of positive and negative deflection, for the different parameters, the necessary torque for bending was again similar and within the standard deviation.

For specimens 2, 5 and 6, due to the joint be being compose of two different fabric layers with their own Young's Modulus, that could affect the results of each positive and negative deflection pair and make them diverge. Young's Modulus effect in the neutral axis of two layer composite can be checked by Equation 5.1. The axis did not change significantly (Table 5.1), so the results for these cases were equally anticipated to be similar. Figures 5.2, 5.5 and 5.6 show the prediction to be correct. Finally, as expected, in specimens 2 through 6 the

3 mm joint width required a larger torque to bend than the 5 mm due to having less flexible area.

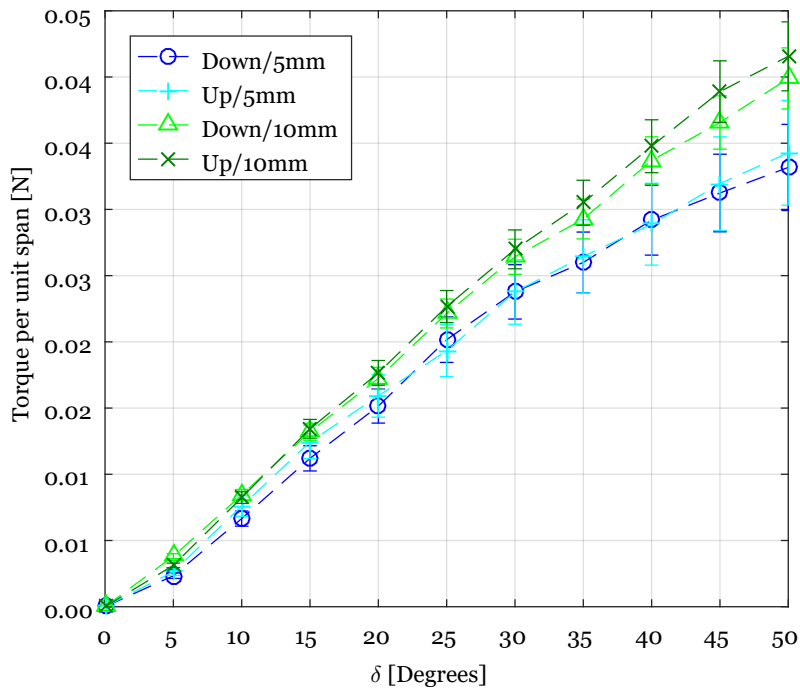


Figure 5.1: Specimen 1 torque per unit span versus measured deflection. Legend - deflection direction/horn height.

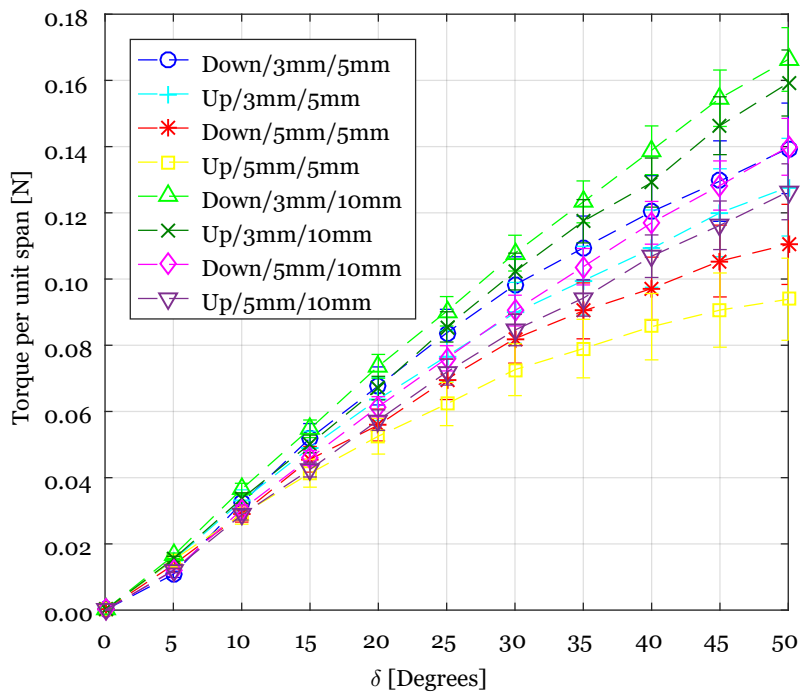


Figure 5.2: Specimen 2 torque per unit span versus measured deflection. Legend - deflection direction/joint width/horn height.

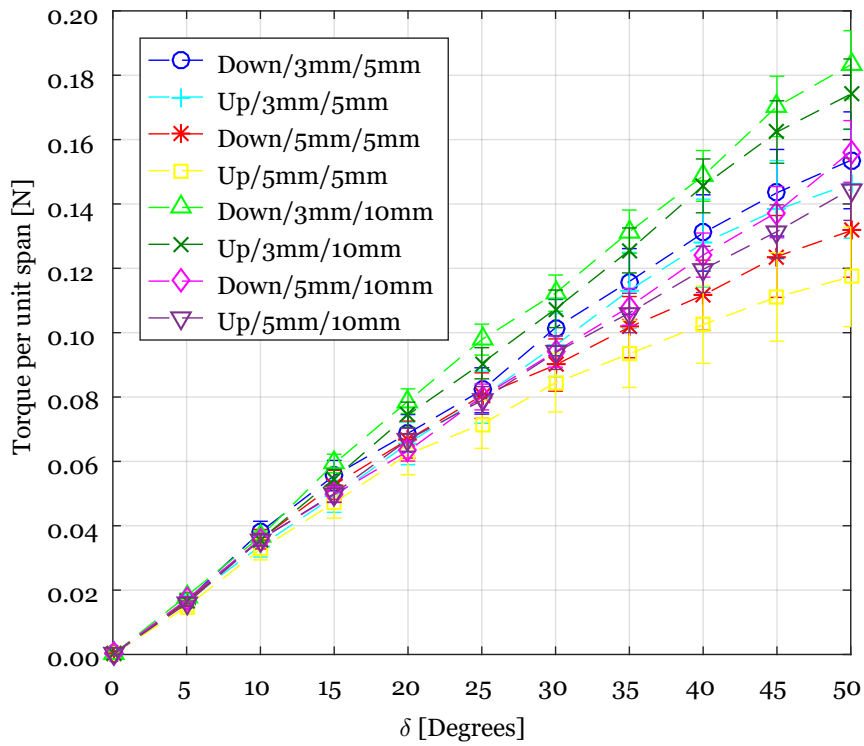


Figure 5.3: Specimen 3 torque per unit span versus measured deflection. Legend - deflection direction/joint width/horn height.

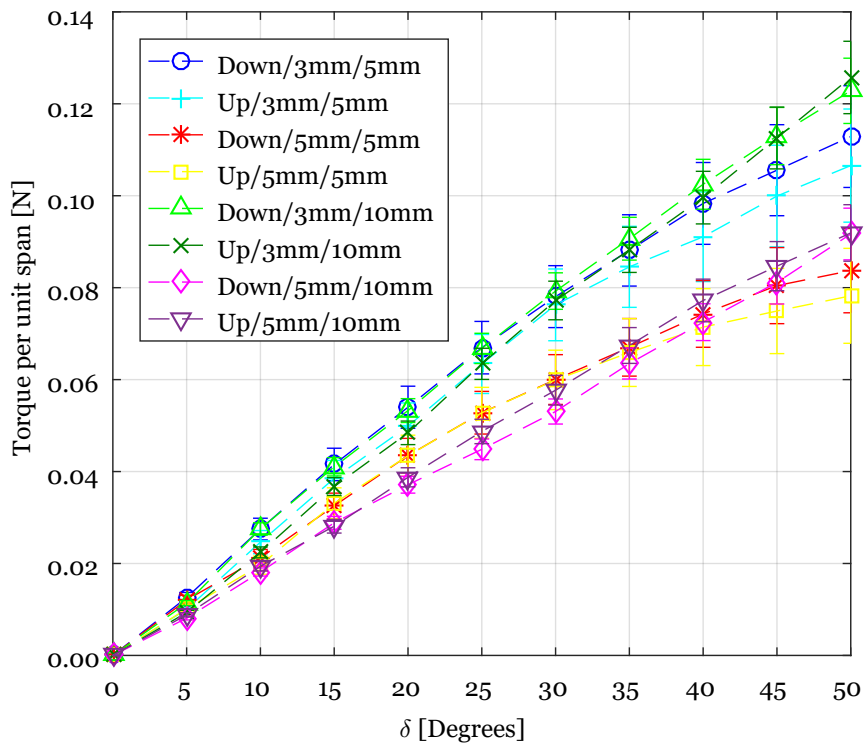


Figure 5.4: Specimen 4 torque per unit span versus measured deflection. Legend - deflection direction/joint width/horn height.

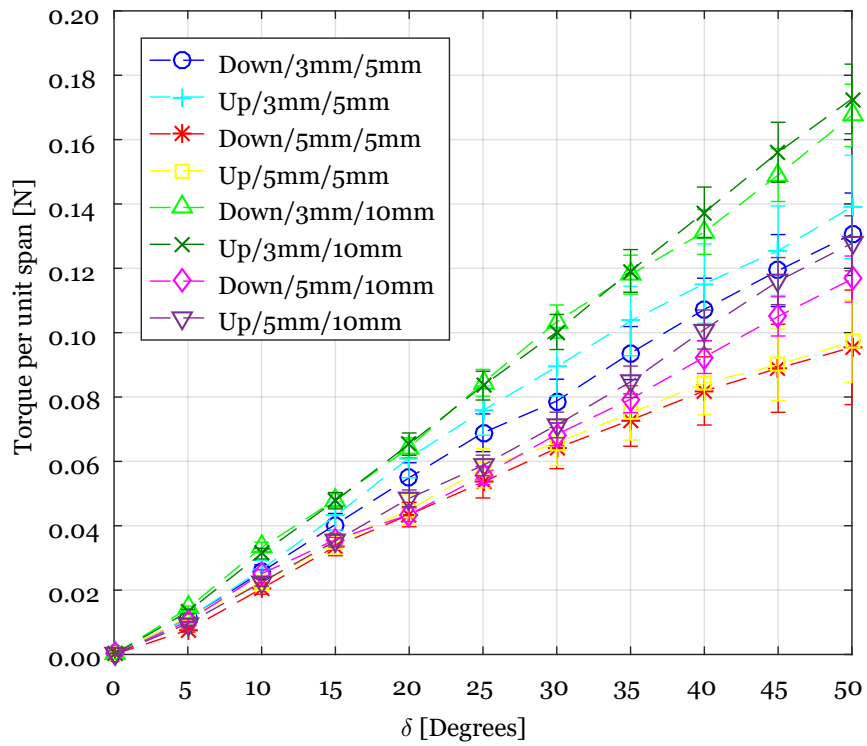


Figure 5.5: Specimen 5 torque per unit span versus measured deflection. Legend - deflection direction/joint width/horn height.

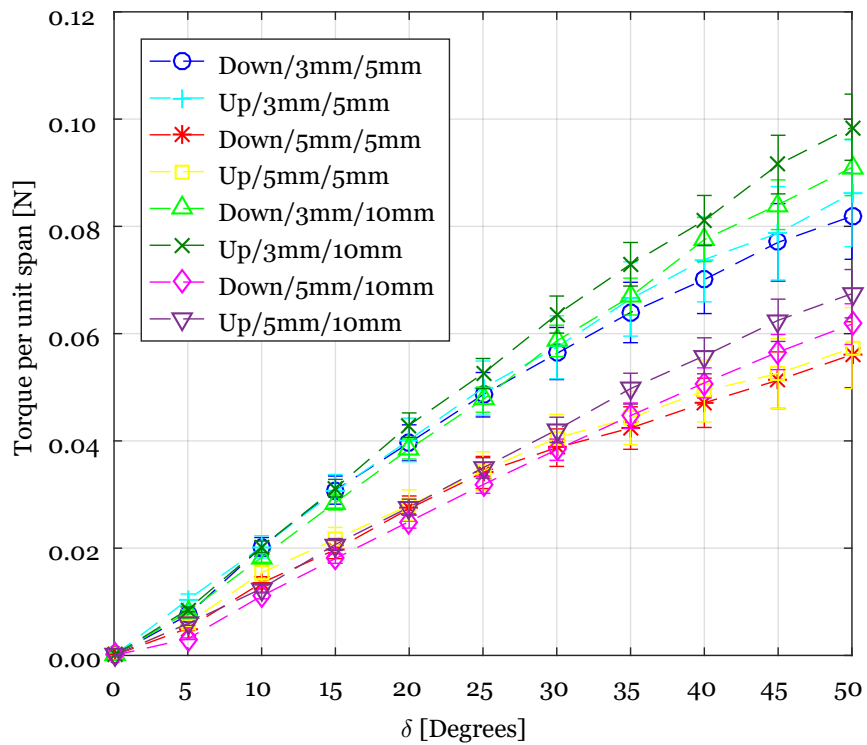


Figure 5.6: Specimen 6 torque per unit span versus measured deflection. Legend - deflection direction/joint width/horn height.

Figures 5.7 through 5.10 show the relation between specimens in terms of the necessary torque required to bend them. Again, the results are shown by unit of span (m). Values for each pair of positive and negative deflection were averaged, since the previous results showed they were similar and within the standard deviation. Since specimen 1 only has one width test, its results were plotted against both the other specimens widths (3 mm and 5 mm) for comparison.

In each test, specimen 1 was by far the one that required less torque to bend, which was expected due to one of the layers being interrupted. Specimen 6 was consistently the second best performer followed by specimen 4. These laminates were fabricated with the two thinner fibres so these results were not surprising. Then, specimen 3 always required the larger amount of torque to bend in the performed tests. Although the aramid fibre had a low weight (36 g m^{-2}), it was the thicker laminate (Table 5.1) leading to higher torque requirements. This also made specimens 2 and 5, which used an aramid layer, be the other specimens with high torque requirements. Between these two, for tests with a 3 mm joint they performed similarly (Figures 5.7 and 5.9), but the same did not occur for the 5 mm joint test, where the specimen 2 required a larger torque (Figures 5.8 and 5.10).

Specimens 2 and 5 produced the only out of pattern results, were the thicker laminate required the larger amount of torque to bend. One of the reasons for this could be explained by the different specimen design; specimen 2 was type A while 5 was type C. Another one could be an irregularity in the manufacturing process, where some extra fibre strands could have been trapped between layers. Because these off the norm results were consistent for both pairs of negative and positive deflections and at the two horn heights. At 3 mm width both specimens had equal torque and, at 5 mm width, specimen 2 produced higher torque.

$$y_n = \frac{E_1 \times t_1 \times \frac{t_1}{2} + E_2 \times t_2 \times \left(\frac{t_1+t_2}{2}\right)}{E_1 \times t_1 + E_2 \times t_2} \quad (5.1)$$

Table 5.1: Specimens laminates joint thickness and neutral axis.

Specimen	Joint thickness [mm]	Neutral axis [mm]
1	0.06 ± 0.01	0.03
2	0.17 ± 0.01	0.94
3	0.22 ± 0.01	0.11
4	0.15 ± 0.01	0.08
5	0.19 ± 0.01	0.09
6	0.14 ± 0.01	0.07

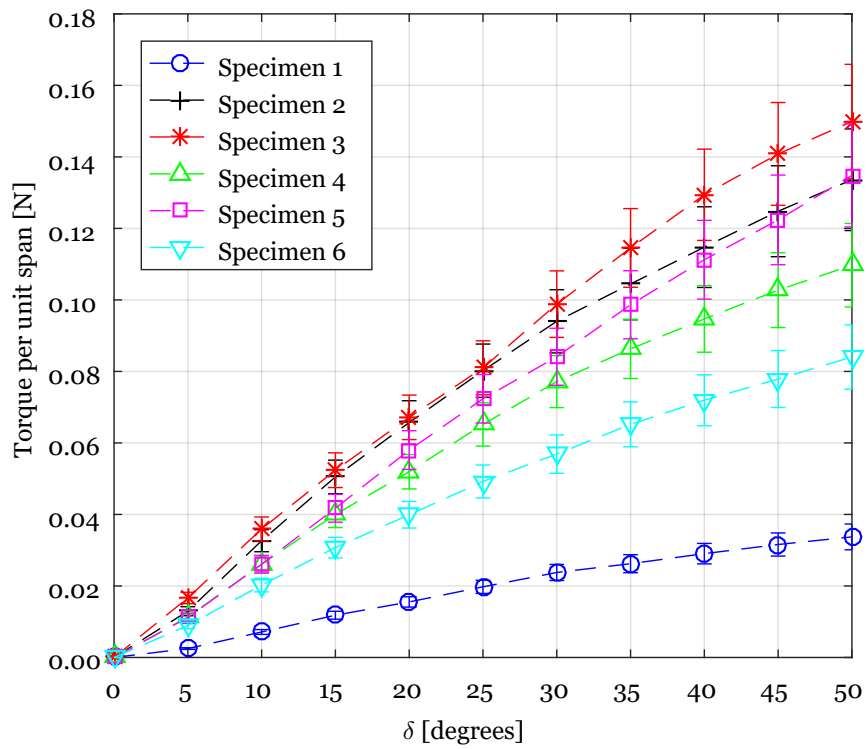


Figure 5.7: Torque per unit span versus measured deflection: 5 mm horn height and 3 mm joint width.

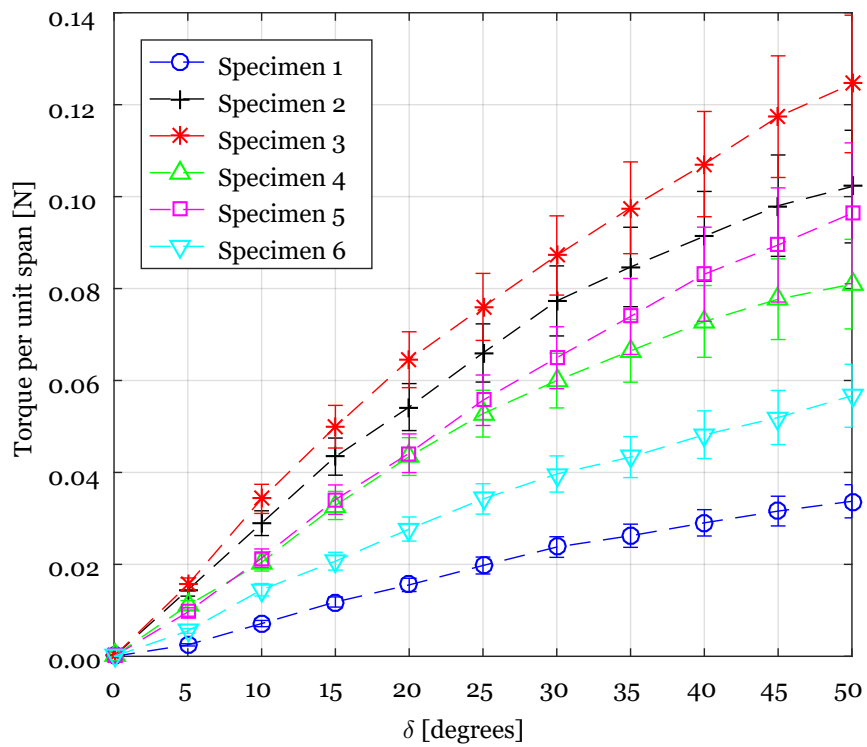


Figure 5.8: Torque per unit span versus measured deflection: 5 mm horn height and 5 mm joint width.

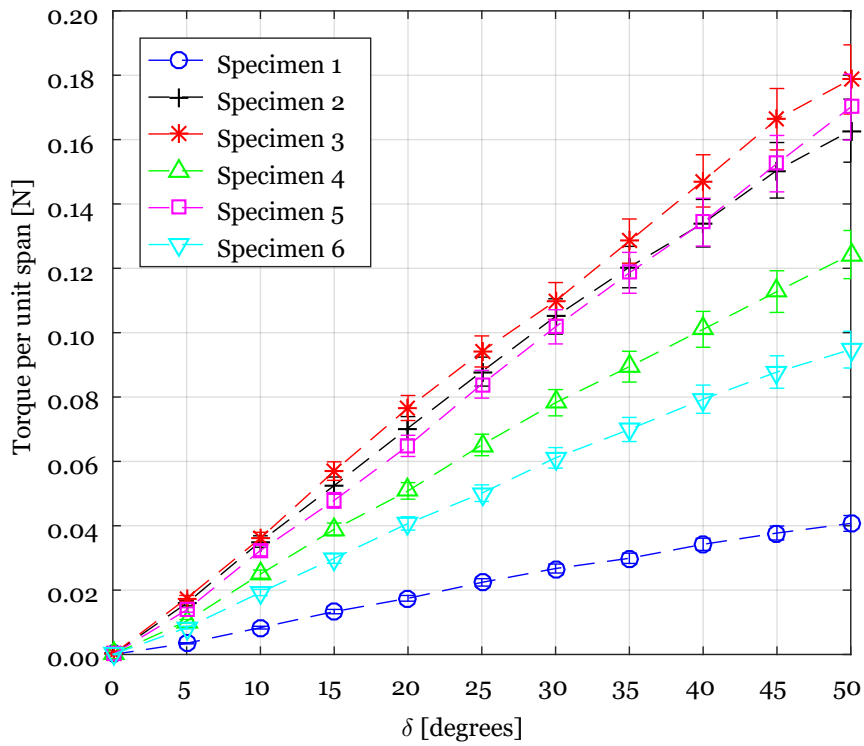


Figure 5.9: Torque per unit span versus measured deflection: 10 mm horn height and 3 mm joint width.

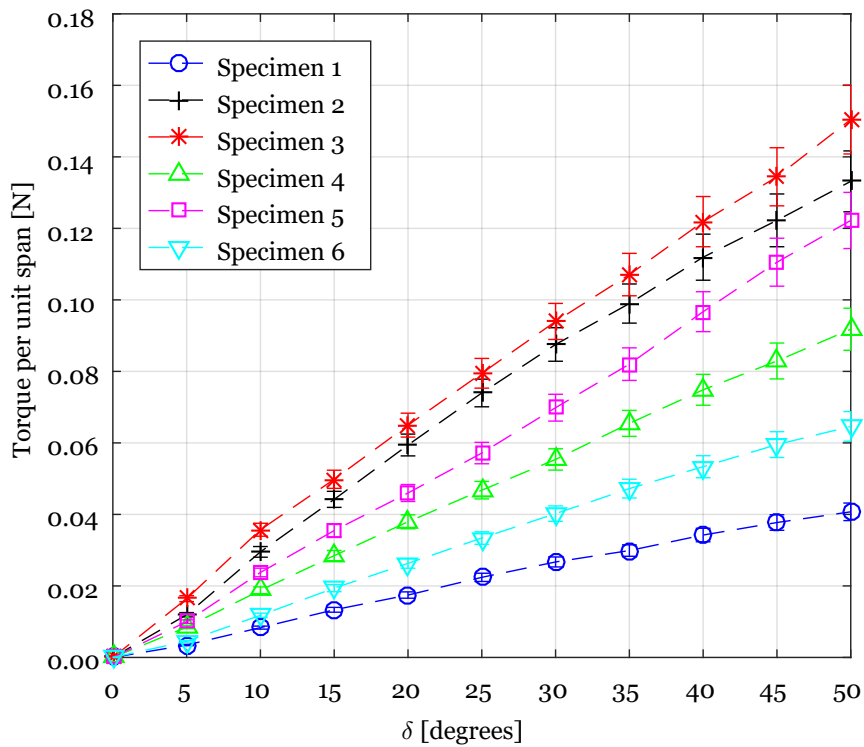


Figure 5.10: Torque per unit span versus measured deflection: 10 mm horn height and 5 mm joint width.

5.2 Elastomer Sheet

This section discusses the results regarding the silicone RTV tensile/strain test and the bonding agent shear stress. In Figure 5.11, the silicone elastic behaviour can be observed as the stress increases linearly with the strain. The linear fit slope gives the elastomer's Young's Modulus in MPa. The result is significantly lower than the predicted, using A. N. Gent equation [44], for the vendors specified shore A range (Table 5.2). This shows the equation inaccuracy for shore A values below 40. Another important property is the Poisson's coefficient, since it is necessary as material data for the Ansys mechanical analysis. The calculated result with the help of MatLab's image processing toolbox and the written program (section 3.2.4) is displayed in Table 5.3. The result shows a value lower than the typical 0.5 for rubbers.

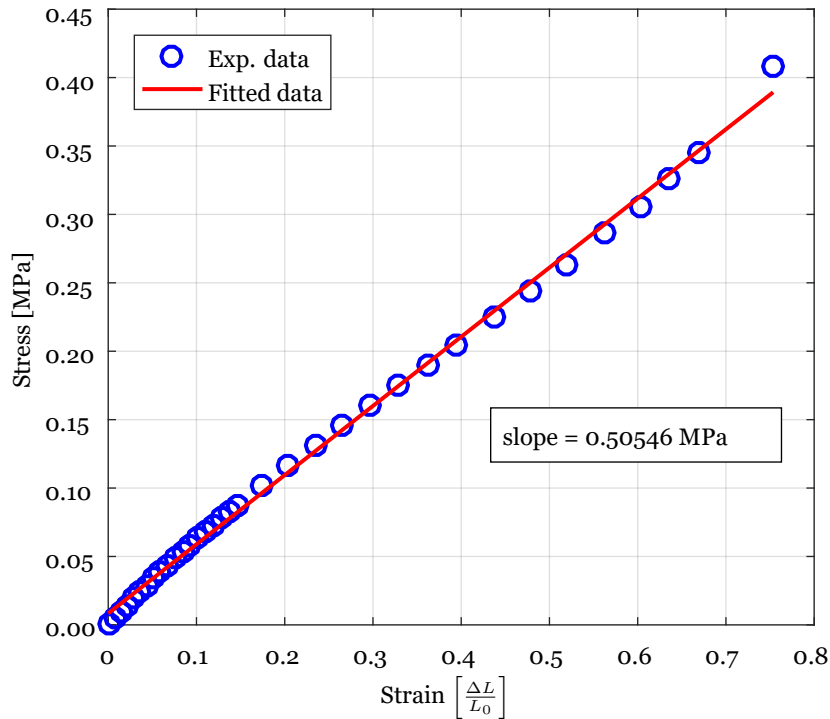


Figure 5.11: Elastomer stress versus strain test results and Young's modulus calculation.

Table 5.2: Predicted elastomer Young's modulus versus experimental test.

Experimental	A. N. Gent	
	23 Shore A	27 Shore A
0.505 MPa	0.844 MPa	1.007 MPa

Table 5.3: Elastomer Poisson's coefficient calculation.

Longitudinal strain (ϵ_z)	Transversal strain (ϵ_x)	Poisson's ratio (ν)
0.75	-0.26	0.35

5.3 XFOIL Hinge Moment

In this section, the XFOIL simulations results for the hinge moments are presented per unit span (m). As can be noted by analysing Figure 5.12, for a deflection of around -20° the moment is neutral for all the Reynolds numbers. As deflection increases from -20° to 0 and then increases in its positive deflection to 50° , the hinge moment also increases. This phenomenon is amplified for higher Reynolds numbers. When deflection keeps increasing in its negative direction from -20° to -50° , the moment also increases but on the opposite direction. Again the Reynolds number has an impact on the values, for higher numbers the moment is also larger. For a Reynolds number of 100 000 and for a -20° flap deflection there is not any result available because the XFOIL simulation never converged for that case.

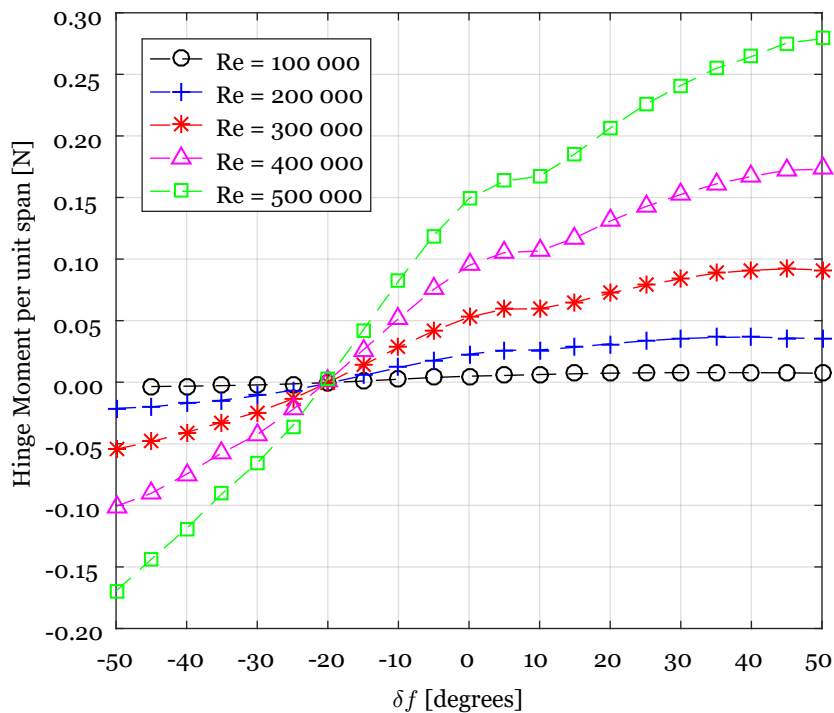


Figure 5.12: Aerodynamic hinge moment per unit span for different Reynolds numbers.

5.4 Elastomer Hinge Moment

In this section, the elastomer's hinge moment results, are presented. With the data gathered in section 5.2 and using the methodology described in section 4.1.1, the moment was calculated for sheets with thickness from 0.1 mm to 1 mm and values of L_0 ranging from 5 mm to 25 mm. The results are presented in Table 5.4. As can be observed, the moment increases with sheet thickness because it requires a larger force to strain the material, as expected. As the value of L_0 increases, the moment decreases. This is due to the elastomer strain being higher a lower values and since the deformations are similar, the initial length will be responsible by the change in moment. For sheets with thickness over 0.4 mm the values for moment per unit span are high even for large values of L_0 . This makes it not suitable for the

project. Also at a low values of thickness and L_0 , the moment is still fairly large. That leaves only as suitable option for the project, a combination of low sheet thickness with a higher value of L_0 .

Table 5.4: Elastomer hinge moment by unit span (m) [N].

L_0 [mm]	Thickness [mm]									
	0.1	0.2	0.3	0.4	0.5	0.6	0.7	0.8	0.9	1
5	0.58	1.16	1.73	2.31	2.89	3.47	4.05	4.62	5.20	5.78
10	0.22	0.44	0.65	0.87	1.09	1.31	1.53	1.75	1.96	2.18
15	0.13	0.27	0.40	0.53	0.67	0.80	0.93	1.07	1.20	1.34
20	0.10	0.19	0.29	0.38	0.48	0.58	0.67	0.77	0.87	0.96
25	0.08	0.15	0.23	0.30	0.38	0.45	0.53	0.60	0.68	0.75

5.5 Silicone Sealant Bonding

As for the bonding agent shear stress test, the results were diversified. This could be explained by the rudimentary methodology employed or due to an uneven application of the bonding agent. With this in mind and looking at Figure 5.13, the worst result for the shear stress test was with specimen 1, where it started to fail at around 45 kPa.

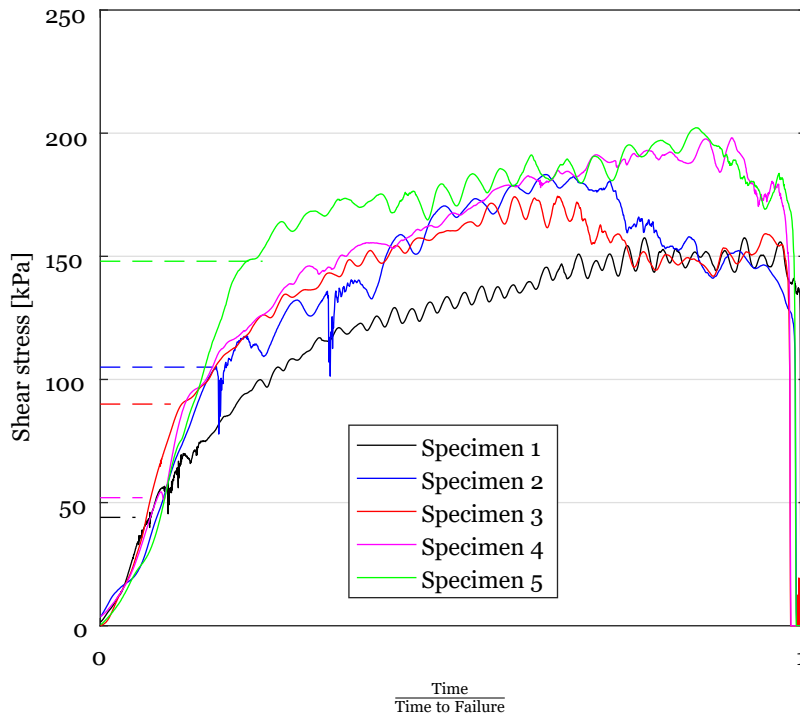


Figure 5.13: Silicone sealant bonding shear stress tests. Horizontal dashed lines indicate the initial failure point.

Finally, the silicone sealant shear stress results for the purposed elastomer sheet thickness (0.4 mm) and values of L_0 (20 mm and 25 mm), are displayed in Table 5.5. For the bonding area, the ACC2019 aircraft wing panel span (745 mm) and two 5 mm widths, one on each side, for a total area of 7450 mm², were considered. The force for both cases was calculated with Equation 4.1 for a 20° flap deflection. As can be observed, the silicone sealant with just two

5 mm wide strips in each side is more than capable of sustaining the shear forces, showing its viability for the project.

Table 5.5: Shear stress calculation for the considered elastomer sheet dimensions.

(L_0)	Force [N]	Shear stress [kPa]
20	40.2	5.4
25	31.4	4.2

5.6 Elastomer Deformation

In this section, the Ansys FEM analyses results, are displayed. The y axis deformation and the Von-Mises stress for the analysis realized in section 4.1.1 are shown in Table 4.7. Regarding the y axis deformation, the lower value of L_0 (20 mm) experiences the least change. That is due to its smaller area which makes it experience less force. For a -20° deflection, the upper skin C_p is positive so the elastomer sheet deforms inwards, which can be noted in tests 1 and 3. On the contrary, for a 20° flap deflection, as the C_p is negative, the elastomer surface experiences suction, so the sheet deforms outwards (test 2 and 4). Regarding the Von-Mises stress for all the performed tests, the values are substantially below the elastomer vendors indicated tensile strength (3.8 MPa and 4.2 MPa). As expected for the positive flap deflection, the 20 mm L_0 (test 2) sheet suffers a higher stress because it experiences a larger strain. Finally, for a negative flap deflection, the 25 mm L_0 (test 3) sheet has a slightly higher stress than test 1. This results from the fact that, at this δ_f , the sheets do not suffer any extension in the x axis. So, the only force acting on it, is the one resulting from the airflow pressure. This combined with a larger surface area leads to a higher force and to a larger stress.

Table 5.6: Elastomer sheet deformation (Y axis) and Von-Mises stress.

Test	Deformation	Von-Mises
1	-0.77 mm	0.013 MPa
2	0.19 mm	0.169 MPa
3	-1.04 mm	0.014 MPa
4	0.31 mm	0.142 MPa

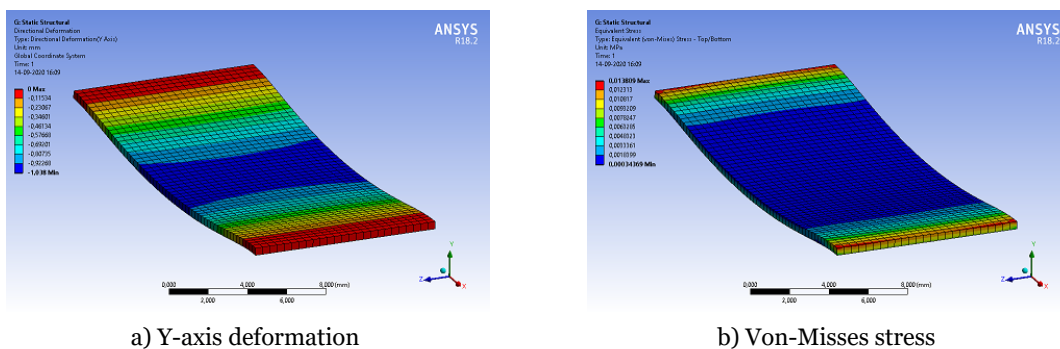


Figure 5.14: Ansys mechanical deformation and Von-Mises stress analyse for test 3.

5.7 Flap Hinge Moments

In this section, the results regarding the moments acting on the flap hinge are presented. Section 4.1.3 described the methodology to size the actuation system. Figure 5.15 illustrates the available torque at the hinge for 3 different servos. As can be observed, the project configuration for the actuation system was optimized with the program referred in section 4.1.3, so the available servo torque was maximum at 20° . For the servo selection, it was necessary that the full moment acting at the hinge was compared to the servo torque. So in Figure 5.15, the hinge moment that needs to be overcome was plotted for the two values of L_0 still in consideration. This moment is the sum of the composite laminate joint moment, aerodynamic moment and the elastomer's sheet moment for a 745 mm span panel. This dimension was chosen to serve as a comparison to the ACC2019 aircraft. As deflection goes from -20° to 20° the hinge moment increases linearly. The 20 mm L_0 has the higher values due to a larger elastomer's strain. Figure 5.15 highlights the importance of having the available servo torque increase as the control surface deflects and reaching its peak at maximum design deflection. Only servo 3 has the capacity to actuate the system for both values of L_0 , while servo 2 barely matches L_0 of 25 mm. Servo 1, which was used for ACC2019 model does not come close to meet the actuation requirements. This shows the elastomer's clear impact on the actuation system.

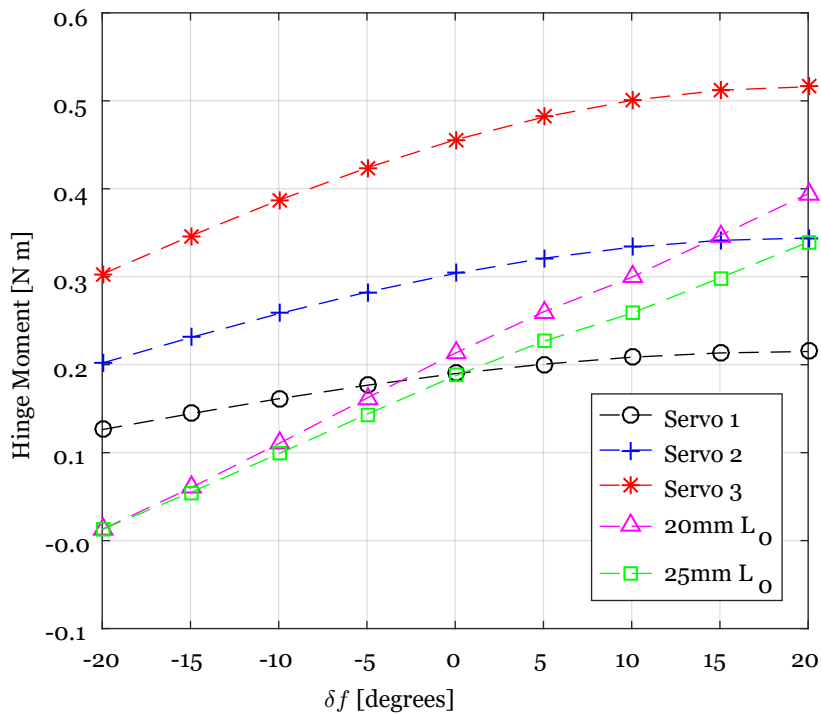


Figure 5.15: Hinge moment versus flap deflection: illustrates the available servo torque and the hinge moment to overcome.

5.8 Flap Validation

In this section, the results concerning the validation of the proposed design are presented. A small panel section (250 mm span) with the proposed design was manufactured with the goal to validate not only the concept but also the methodology behind it. Section 4.3 described the experimental setup to conduct such testing and the results are displayed in Figure 5.8. This test only took into account the mechanical moment resulting from the composite laminate joint and the elastomer sheet, the aerodynamic hinge moment was not considered. As can be seen, the experimental results are in agreement with the designs predictions. This demonstrates the concept viability and also the validity of the methodology used. Another important aspect is the panel final mass: Table 5.7 compares the design predicted mass to the built one. It is clear that the prototype has a larger mass. It is important to refer that the design mass does not include the epoxy resin mixture with micro-balloons, used to close the panel. Also, it does not take into account the silicone sealant used to bond the elastomer sheet. Even then, this would not account for all the extra mass, so it is clear that there was some added mass due to manufacturing inaccuracies.

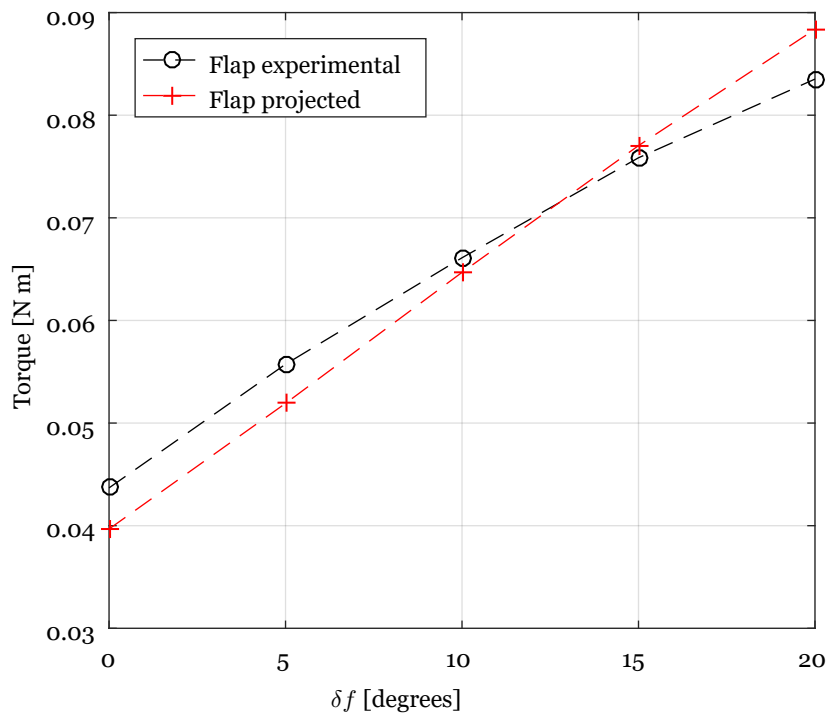


Figure 5.16: Flap design and final build required torque comparison.

Table 5.7: Final versus predicted panel mass by unit span (m).

Flap	Value [kg/span]
Design	0.344
Final	0.384

Chapter 6

Conclusions and Future Work

6.1 Conclusions

From the literature review accomplished in chapter 2, the recent push in the development of trailing edge morphing concepts can be noted. The increasing requirements in fuel emissions and noise regulations led the research for more efficient aircraft designs. In these concepts various actuation systems and structures were described but the use of piezoelectric actuators or SMA's made them unsuitable for this project due to high cost and/or complexity. SMA would require two systems to deflect, one for each direction. This made traditional servo motor actuated control surfaces as the only practical solution. The use of elastomeric material as skin proved to be an interesting solution for a flexible wing and one that was investigated. Modern competition gliders use flexible hinges placed at one of the wing skins for the control surfaces, while the other exhibits a gap. So, a smooth surface can be achieved, the gap is closed by means of a built in wiper or a gap seal. For the purpose of this work, the idea of closing the hinge gap with an elastomer sheet was worked on. As for the flexible hinge, different types of joints using various types of composite fabrics were researched.

With a basic concept defined, specimens for the joints types were manufactured and tested. The results showed that any configuration without aramid fibre was a suitable candidate. After market research, a silicone RTV rubber was chosen as a prime candidate for the elastomer. A novel test apparatus was devised to realize a stress/strain test to find the Young's Modulus. The results combined with the employed methodology led to conclude that within certain design parameters it was possible to use an elastomer sheet to close the upper wing skin gap. Although silicone is a material difficult to bond, testing proved that a silicone acetate was more than capable of sustaining the shear stresses. Fitting the actuation system inside a thin aerofoil proved a challenging task. Higher actuation requirements resulting from the use of an elastomer combined with a small actuation system lever led to the necessity of stronger servo motors. The creation of a program to calculate the available hinge torque based on design parameters, showed how important optimization is. It then became possible to size the actuation system so maximum torque was achieved at full design flap deflection, without unnecessary system oversizing.

With all previous steps concluded, a final flap design was incorporated in the ACC2019 model central wing panel. The manufacturing of this design brought to attention the extra complexity in installing an elastomer sheet. After the manufacturing of the upper skin, a cut had to be done where the elastomer sheet was going to be applied. For the bonding process a mould

with the flap deflection at installation was manufactured. For the closing process, the upper skin had to be fixed in position with the help of tape, since the elastomer had to be stretched for this. The finished panel section also demonstrated some other design limitations. The elastomer position meant that a replacement was almost impossible, also the flap horn being in the interior poses a challenge, in case of failure a cut in the panel is needed for servicing. Final testing led to conclude that the presented design is viable and the employed methodology predicted with good accuracy the built concept.

6.2 Future Work

In light of the conclusions drawn, it becomes imperative that a new design for the elastomer sheet needs to be achieved. Despite the concept viability, demonstrated by the realized work, a design that allows an easy service of the elastomeric sheet would be a great improvement. Also the silicone sheet massively impacted the required force to actuate the system. A study of different elastic materials not only could find an alternative with lower Young's Modulus, but also a manufacturing technique that enables the fabrication of sheets with lower thickness. A consequence of higher actuation requirements, is the need for bigger servo motors, these add extra weight to the system. Although this design removes a gap responsible for increased drag, in the end it is a trade-off. Air cargo challenge competitions involve, as the name suggests, the transportation of a payload. If systems mass is increased, available payload decreases. With this in mind, a study of the aerodynamic gains compared with the loss in payload would be of great interest and further prove or dismiss the concept application. Another aspect that requires a deeper look, is the aerodynamic effects on the elastomer. A basic study of the deformation resultant from pressure forces was performed in this work, but a full analysis including viscous forces and the aeroelastic behaviour from the elastomer structure would be of great value. A fatigue study of the flap device is required to find out how many cycles it takes until the system experiences failure, especially regarding the composite joint in the lower wing surface and the elastomer. An interesting experiment would be to manufacture composite laminate joints with a large thickness. Then small incisions would be made along the hinge line to remove material. This way the composite joint flexural rigidity could be controlled.

Bibliography

- [1] “The Competition |.” [Online]. Available: <http://acc2013.ubi.pt/?page{id}=2> 1
- [2] T. Corke, *Design of Aircraft*. Prentice Hall, 2003. [Online]. Available: <https://books.google.pt/books?id=u8keAQAIAAJ> 1
- [3] R. Pecora, F. Amoroso, M. Magnifico, I. Dimino, and A. Concilio, “KRISTINA: Kinematic rib-based structural system for innovative adaptive trailing edge,” S. F. Griffin, Ed., vol. 9801. International Society for Optics and Photonics, apr 2016, pp. 67–77. 3
- [4] J. Brezillon and J. Wild, “Evaluation of Different Optimization Strategies for the Design of a High-Lift Flap Device,” in *Evolutionary and Deterministic Methods for Design, EUROGEN, Munich*, 2005. 3
- [5] B. Gunston, *The Cambridge Aerospace Dictionary*, ser. Cambridge aerospace series. Cambridge University Press, 2004. [Online]. Available: <https://books.google.pt/books?id=l5JUAAAAMAAJ> 4
- [6] H. A. H. A. Taylor, *Fairey aircraft since 1915*. Putnam, 1974. 4
- [7] J. Anderson and J. Anderson, *A History of Aerodynamics: And Its Impact on Flying Machines*, ser. Cambridge Aerospace Series. Cambridge University Press, 1998. [Online]. Available: <https://books.google.pt/books?id=1OeCJFJY3ZYC> 4
- [8] J. Hansen, N. Aeronautics, and S. Administration, *The Wind and Beyond: A Documentary Journey Into the History of Aerodynamics in America: Reinventing the Airplane*, ser. Nasa History: SP 2007-2009. Bernan Assoc, 2009. [Online]. Available: <https://books.google.pt/books?id=ks887EpTBFMC> 4
- [9] F. Hitchens, *The Encyclopedia of Aerodynamics*. Andrews UK Limited, 2015. [Online]. Available: <https://books.google.pt/books?id=izvoCgAAQBAJ> 5
- [10] R. Pecora, F. Amoroso, and M. Magnifico, “Toward the bi-modal camber morphing of large aircraft wing flaps: the CleanSky experience,” S. F. Griffin, Ed., vol. 9801. International Society for Optics and Photonics, apr 2016. 5
- [11] A. K. Jha and J. N. Kudva, “Morphing aircraft concepts, classifications, and challenges,” in *Smart Structures and Materials 2004: Industrial and Commercial Applications of Smart Structures Technologies*, E. H. Anderson, Ed., vol. 5388. International Society for Optics and Photonics, jul 2004, pp. 213–224. 5

- [12] C. G. Diaconu, P. M. Weaver, and F. Mattioni, “Concepts for morphing airfoil sections using bi-stable laminated composite structures,” *Thin-Walled Structures*, vol. 46, no. 6, pp. 689–701, 2008. 5
- [13] A.-M. R. McGowan, A. E. Washburn, L. G. Horta, R. G. Bryant, D. E. Cox, E. J. Siochi, S. L. Padula, and N. M. Holloway, “Recent Results from NASA’s Morphing Project [C].” *SPIE’s 9th Annual International Symposium on Smart Structures and Materials*, vol. 4698, pp. 97–111, 2002. 5
- [14] D. Bornengo, F. Scarpa, and C. Remillat, “Evaluation of hexagonal chiral structure for morphine airfoil concept,” in *Proceedings of the Institution of Mechanical Engineers, Part G: Journal of Aerospace Engineering*, vol. 219, no. 3. SAGE PublicationsSage UK: London, England, mar 2005, pp. 185–192. 5
- [15] S. Barbarino, O. Bilgen, R. M. Ajaj, M. I. Friswell, and D. J. Inman, “A review of morphing aircraft,” pp. 823–877, jun 2011. 5
- [16] R. Vos, R. Barrett, R. de Breuker, and P. Tiso, “Post-buckled precompressed elements: a new class of control actuators for morphing wing UAVs,” *Smart Materials and Structures*, vol. 16, no. 3, pp. 919–926, jun 2007. 5
- [17] R. Vos, R. De Breuker, R. Barrett, and P. Tiso, “Morphing wing flight control via post-buckled precompressed piezoelectric actuators,” in *Journal of Aircraft*, vol. 44, no. 4, jul 2007, pp. 1060–1068. 5
- [18] O. Bilgen, K. Kochersberger, E. C. Diggs, A. J. Kurdila, and D. J. Inman, “Morphing wing micro-air-vehicles via macro-fiber-composite actuators,” in *Collection of Technical Papers - AIAA/ASME/ASCE/AHS/ASC Structures, Structural Dynamics and Materials Conference*, vol. 1. Reston, Virigina: American Institute of Aeronautics and Astronautics, apr 2007, pp. 1005–1020. 5
- [19] S. Barbarino, R. Pecora, L. Lecce, A. Concilio, S. Ameduri, and E. Calvi, “A Novel SMA-based Concept for Airfoil Structural Morphing,” *Journal of Materials Engineering and Performance*, vol. 18, no. 5-6, pp. 696–705, aug 2009. 6
- [20] C. Thill, J. A. Etches, I. P. Bond, K. D. Potter, and P. M. Weaver, “Composite corrugated structures for morphing wing skin applications,” *Smart Materials and Structures*, vol. 19, no. 12, p. 124009, dec 2010. 6
- [21] A. V. Popov, T. L. Grigorie, R. M. Botez, Y. Mébarki, and M. Mamou, “Modeling and Testing of a Morphing Wing in Open-Loop Architecture,” *Journal of Aircraft*, vol. 47, no. 3, pp. 917–923, may 2010. 6

- [22] R. Vos and R. Barrett, “Mechanics of pressure-adaptive honeycomb and its application to wing morphing,” *Smart Materials and Structures*, vol. 20, no. 9, p. 094010, sep 2011. 6
- [23] B. K. S. Woods and M. I. Friswell, “Preliminary investigation of a Fishbone Active Camber concept,” in *ASME 2012 Conference on Smart Materials, Adaptive Structures and Intelligent Systems, SMASIS 2012*, vol. 2, 2012, pp. 555–563. 6, 7
- [24] W. Liu, H. Zhu, S. Zhou, Y. Bai, Y. Wang, and C. Zhao, “In-plane corrugated cosine honeycomb for 1D morphing skin and its application on variable camber wing,” *Chinese Journal of Aeronautics*, vol. 26, no. 4, pp. 935–942, 2013. 6
- [25] A. Pankonien and D. J. Inman, “Experimental testing of spanwise morphing trailing edge concept,” H. Sodano, Ed., vol. 8688. International Society for Optics and Photonics, apr 2013, p. 868815. 7
- [26] T. Yokozeki, A. Sugiura, and Y. Hirano, “Development of Variable Camber Morphing Airfoil Using Corrugated Structure,” *Journal of Aircraft*, vol. 51, no. 3, pp. 1023–1029, may 2014. 7
- [27] D. Kumar, S. F. Ali, and A. Arockiarajan, “Structural and Aerodynamics Studies on Various Wing Configurations for Morphing,” *IFAC-PapersOnLine*, vol. 51, no. 1, pp. 498–503, 2018. 7
- [28] W. R. Kang, E. H. Kim, M. S. Jeong, I. Lee, and S. M. Ahn, “Morphing wing mechanism using an SMA wire actuator,” *International Journal of Aeronautical and Space Sciences*, vol. 13, no. 1, pp. 58–63, mar 2012. 7
- [29] Wimteevee. (2010, Dec. 21) Europhia wing build. [YouTube video]. Accessed Sep. 25, 2020. [Online]. Available: <https://www.youtube.com/watch?v=2LgqpFxTcAc> 7
- [30] Flightcomp. (2019, Jul. 06) How it’s made. inside gcm, vertigo f5j wing construction. [YouTube video]. Accessed Sep. 25, 2020. [Online]. Available: <https://www.youtube.com/watch?v=D88C8wkrVXM> 8
- [31] Flightcomp. (2020, Apr. 26) Vertigo f5j solid core center panel assembly. [YouTube video]. Accessed Sep. 25, 2020. [Online]. Available: <https://www.youtube.com/watch?v=GZXwVfsy4No> 8
- [32] Flightcomp. (2019, Aug. 15) Gcm vertigo f5j aileron servo install. [YouTube video]. Accessed Sep. 25, 2020. [Online]. Available: <https://www.youtube.com/watch?v=LqBzTygqK6A> 8

- [33] Flightcomp. (2019, Aug. 29) Samba prestige 2pk f5j flap servo installation. [YouTube video]. Accessed Sep. 25, 2020. [Online]. Available: <https://www.youtube.com/watch?v=-UN7GagaiYA8>
- [34] Flightcomp. (2019, Sep. 17) Gcm vertigo f5j flap servo install. [YouTube video]. Accessed Sep. 25, 2020. [Online]. Available: <https://www.youtube.com/watch?v=dpkTPoL9AK48>
- [35] Flightcomp. (2019, May. 26) Ccm optimus sport f5j/f3j intro and build part 2. [YouTube video]. Accessed Sep. 25, 2020. [Online]. Available: https://www.youtube.com/watch?v=PpoGhqo_ng88
- [36] Flightcomp. (2019, May. 26) Ccm optimus sport f5j/f3j intro and build part 3. [YouTube video]. Accessed Sep. 25, 2020. [Online]. Available: <https://www.youtube.com/watch?v=Le5tWjaL2Oo8>
- [37] J. Manor, “Carbon Testing Part 2! Hollow Molded Monster! - Page 126 - RC Groups.” [Online]. Available: <https://www.rcgroups.com/forums/showthread.php?778363-Carbon-Testing-Part-2-21-Hollow-Molded-Monster-21/page1268>
- [38] Meunier, Pierre. (2017, May 31) Wednesday tech n°003 : How to and why gap seal ? [YouTube video]. Accessed Sep. 25, 2020. [Online]. Available: <https://www.youtube.com/watch?v=zd4QjqXkNxQ9>
- [39] Timmy RC. (2017, Aug. 13) How to gap seal your glider. [YouTube video]. Accessed Sep. 25, 2020. [Online]. Available: <https://www.youtube.com/watch?v=mi12LHkcI6g9>
- [40] Scribner, Jason. (2015, Aug. 12) F3k gap-seal 101. [YouTube video]. Accessed Sep. 25, 2020. [Online]. Available: <https://www.youtube.com/watch?v=k6YaEmqRhyA9>
- [41] Departamento de Física da FCTUC, “INTRODUÇÃO AO CÁLCULO DE ERROS NAS MEDIDAS DE GRANDEZAS FÍSICAS,” Tech. Rep. [Online]. Available: http://fisica.uc.pt/data/20072008/apontamentos/apnt_221_1.pdf18
- [42] A. Limited, “6. How to Use Load Cells,” Tech. Rep. [Online]. Available: <https://www.aandd.jp/products/weighing/loadcell/introduction/pdf/6-1.pdf18>
- [43] E. A. Bubert, B. K. Woods, K. Lee, C. S. Kothera, and N. Wereley, “Design and Fabrication of a Passive 1D Morphing Aircraft Skin,” *Journal of Intelligent Material Systems and Structures*, vol. 21, no. 17, pp. 1699–1717, nov 2010. 19, 24
- [44] A. N. Gent, “On the Relation between Indentation Hardness and Young’s Modulus,”

Rubber Chemistry and Technology, vol. 31, no. 4, pp. 896–906, 1958. 19, 54

- [45] American Society for Testing and Materials. ASTM., “Designation: D 412 – 06a Standard test method for tensile properties of Vulcanized Rubber and Thermoplastic Elastomers—,” *ASTM D 412-06a*, vol. 598, pp. 143–152, 2018. 20

- [46] M. Drela, “XFOIL - Subsonic Airfoil Development System.” [Online]. Available: <https://web.mit.edu/drela/Public/web/xfoil/> 24

Appendix A

Annexes

A.1 Datasheets of the used components

Table A.1: YZC-133 1 kg and 5 kg Load Cell.

Model Capacity Rated output	Kg mV/V	YZC-133 1, 2, 3, 5, 10, 20 1.0 ± 0.15
Errors		
Non-linearity	%	0.05
Repeatability	%	0.03
Hysteresis	%	0.03
Creep (5 min)	%	0.1
Zero Balance	%RO	± 0.1
Temperatures		
Temperature effect of sensitivity	%RO/°C	0.003
Temperature effect on zero	%RO/°C	0.02
Compensated temperature range	°C	-10 +50
Operating temperature range	°C	-20 +65
Resistances		
Input resistance	Ω	1066 ± 20
Output resistance	Ω	1000 ± 20
Insulation resistance	MΩ(50V)	2000
Operation		
Recommended excitation voltage	V	5
Safe overload	%RO	120
Ultimate overload	%RO	150
Connection wire	Red input(+), black input(-) green output(+), white output(-)	

Table A.2: Silicone acetate for wet rooms.

Model	LE_08925600	
Technical Data		
Raw material base		Acetate system
Max. continuous motion absorption	%	25 of joint width
Skin formation time	minutes	Approx. 20 at 25°C/ 50% humidity
Curing speed	millimetre	Approx. 3 after 24h/ 50% humidity
Elastic at	°C	-40 to +100°C
Application temperature	°C	5 to 40
Can be painted over	No	But preliminary tests required
Coating compatibility	Yes	
Suitable for wet rooms	Yes	
Fungicidal properties	Yes	
Hardness	Shore A	Approx. 18
Specific mass at 23°C	g cm ⁻³	1.01
Breaking elongation	%	250
Storage	months	24
Performance		
Fire behaviour	Class E	
Release of harmful chemicals	%, g/l	<1, 10
Resistance to flow	%	≤ 10
Loss in volume	millimetre	≤ 2
Durability	Passed	
Tensile strength at -30°C	MPa	≤ 0.9
Elastic recovery	%	≥ 70
Determination of microbial effects	Class 1	

Table A.3: NI-TB 4330 data acquisition board.

Electrical		
Trace resistance QTR, EX+, EX-	m Ω	<20
Mechanical		
Screw terminal wire gauge	AWG, max	14
Physical		
Height	cm	15.28
Length	cm	12.95
Weight	g	548
Environmental Specifications		
Maximum altitude	m (mbar)	2000 (800)
Pollution Degree		2
Indoor use only		
Operating Environment		
Ambient temperature range	$^{\circ}\text{C}$	0 to 55
Relative humidity range	%	10 to 90
Storage Environment		
Ambient temperature range	$^{\circ}\text{C}$	-40 to 71
Relative humidity range	%	5 to 95
Shock and Vibration		
Operating Shock	30 g peak, half-sine,	11 ms pulse
Random vibration		
Operating	Hz, $g_m s$	5 to 500, 0.3
Non-operating	Hz, $g_m s$	5 to 500, 2.4
Safety		
Measurement Category		1
Safety Standards		
IEC 61010-1, EN 61010-1		
UL 61010-1, CSA 61010-1		

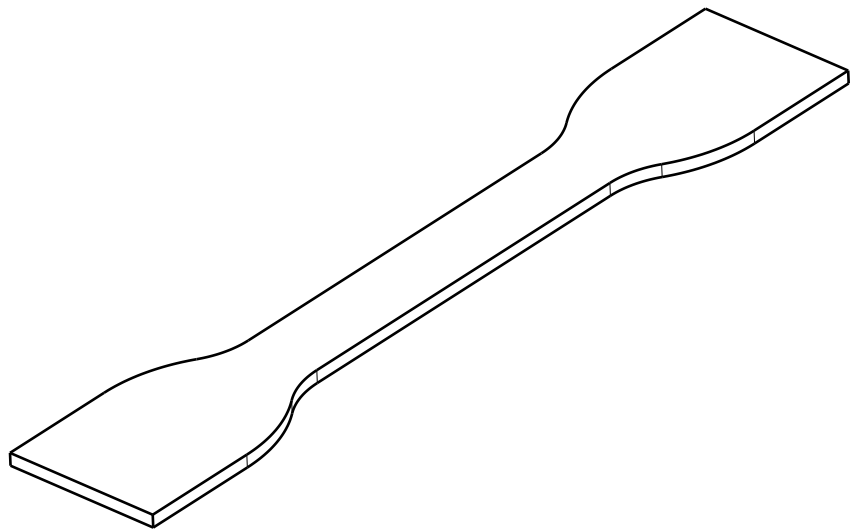
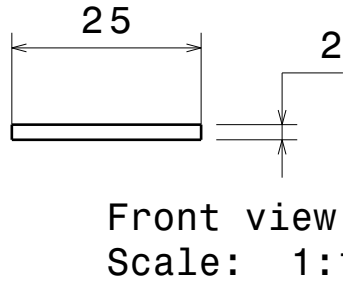
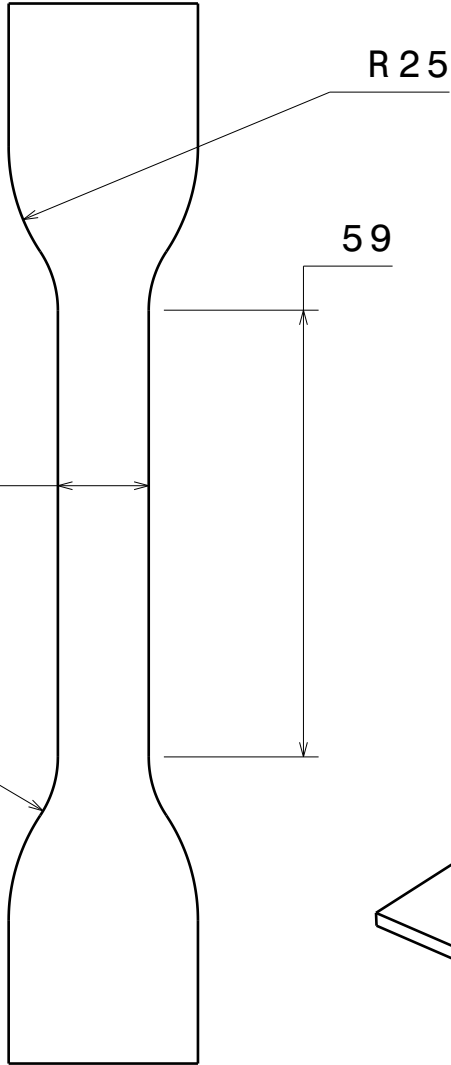
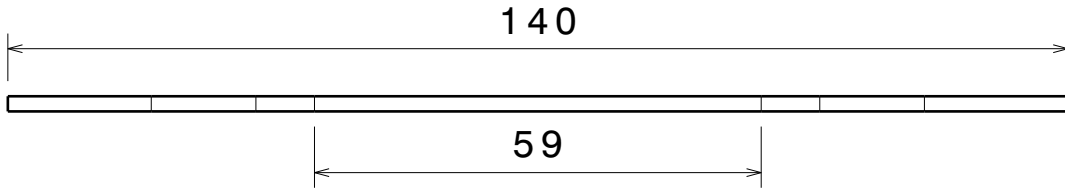
A.2 Technical Drawings

D

C

B

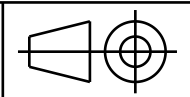
A



DESIGNED BY:
Ricardo
DATE:
17/10/2020
CHECKED BY:
XXX
DATE:
XXX

UNITS IN MILLIMITRES

SIZE
A4



DIE TYPE A

SCALE
1:1

DRAWING NUMBER
Part1

SHEET
1/1

I	-
H	-
G	-
F	-
E	-
D	-
C	-
B	-
A	-

This drawing is our property; it can't be reproduced or communicated without our written agreement.

D

A

4

4

3

3

2

2

1

1

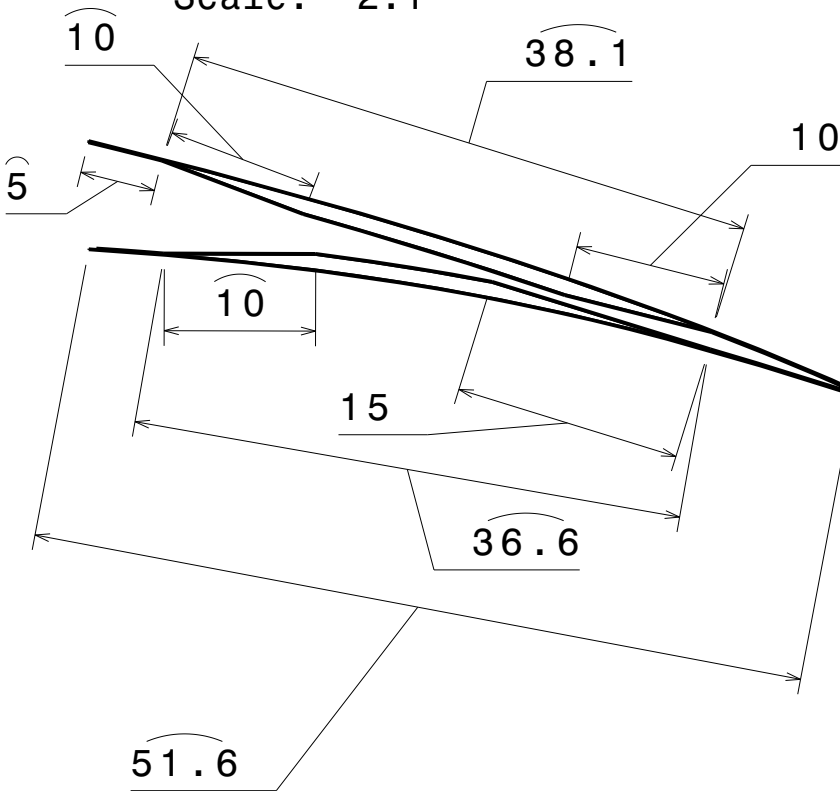
D

C

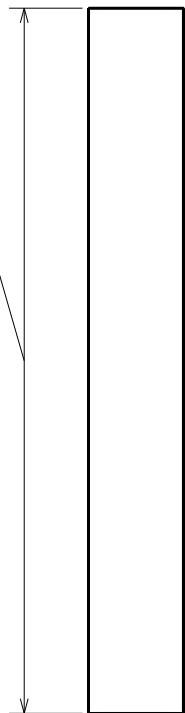
B

A

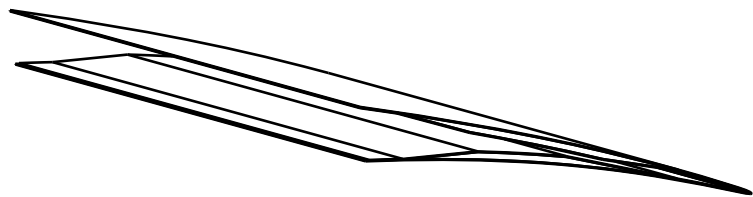
Front view
Scale: 2:1



372.5



Top view
Scale: 1:4



Isometric view
Scale: 1:1



Left view
Scale: 1:5

DESIGNED BY:
Ricardo

DATE:
17/10/2020

CHECKED BY:
XXX


DATE:
XXX

UNITS ARE IN MILLIMETRES

FLAP SHELL

I	-
H	-
G	-
F	-
E	-
D	-
C	-
B	-
A	-

SIZE
A4



SCALE
1:1

WEIGHT (kg)

DRAWING NUMBER
Part6

SHEET
1/1

This drawing is our property; it can't be reproduced or communicated without our written agreement.

D

A

4

4

3

3

2

2

1

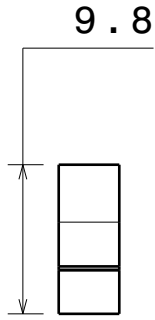
1

D

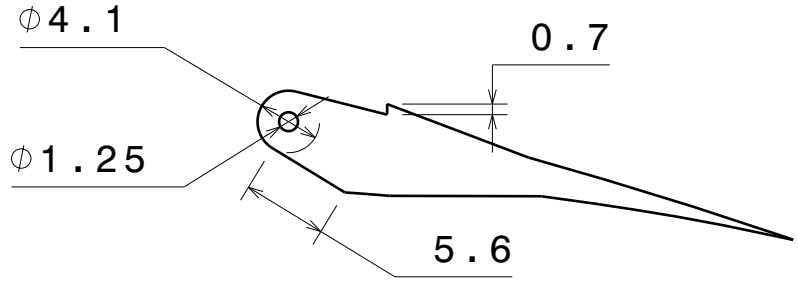
C

B

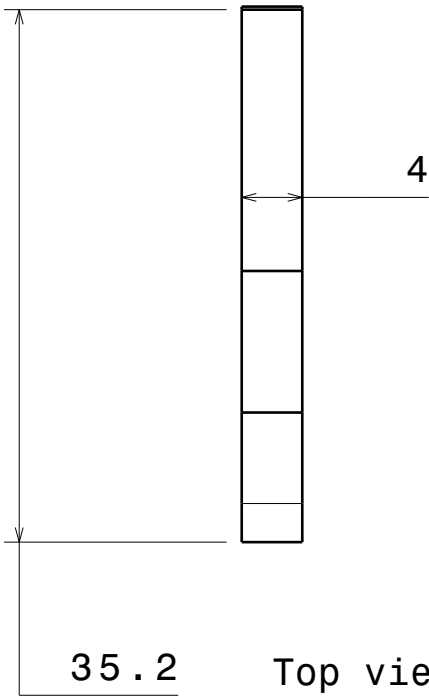
A



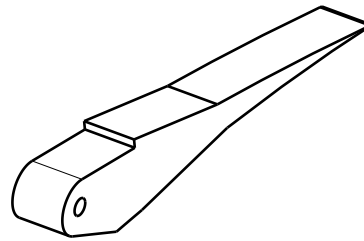
Front view
Scale: 2:1



Right view
Scale: 2:1



Top view
Scale: 2:1

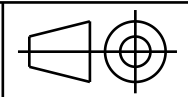


Isometric view
Scale: 2:1

DESIGNED BY:
Ricardo
DATE:
16/10/2020
CHECKED BY:
XXX
DATE:
XXX

UNITS ARE IN MILLIMETRES

SIZE
A4



FLAP HORN

SCALE
2:1

DRAWING NUMBER

Part6

SHEET
1 / 1

This drawing is our property; it can't be reproduced or communicated without our written agreement.

D

A

4

4

3

3

2

2

1

1

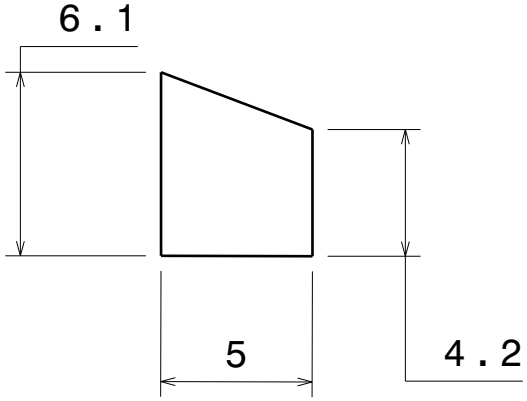
D

C

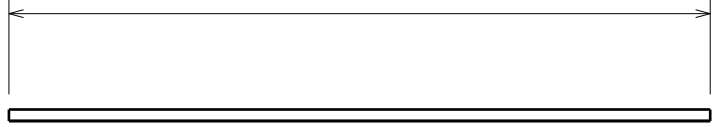
B

A

Front view
Scale: 4:1



370.5



Left view
Scale: 1:4

4

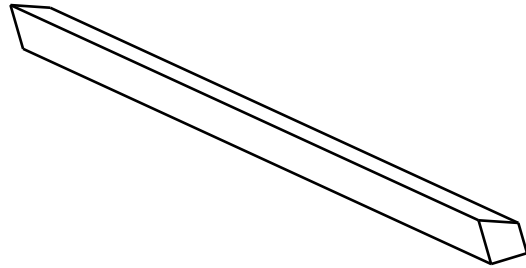
4

3

3



Top view
Scale: 1:4



Isometric view
Scale: 1:1

2

2

1

1

DESIGNED BY:
Ricardo

DATE:
16/10/2020

CHECKED BY:
XXX

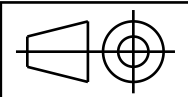
DATE:
XXX

UNITS IN MILLIMITRES

FLAP SPAR

I	-
H	-
G	-
F	-
E	-
D	-
C	-
B	-
A	-

SIZE
A4



DRAWING NUMBER
Part6

SHEET
1 / 1

SCALE
1:1

WEIGHT (kg)

DRAWING NUMBER
Part6

SHEET
1 / 1

This drawing is our property; it can't be reproduced or communicated without our written agreement.

D

A

D

C

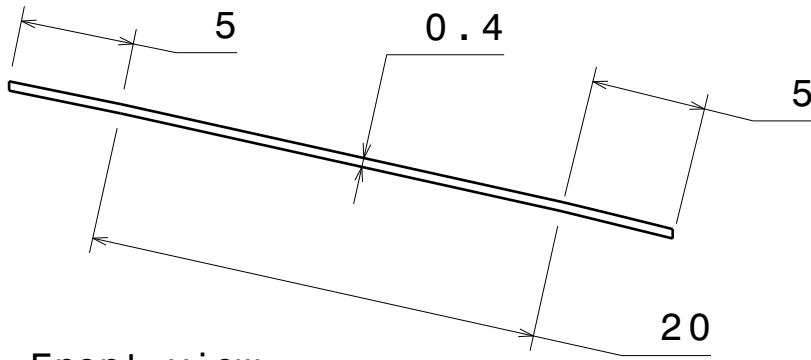
B

A

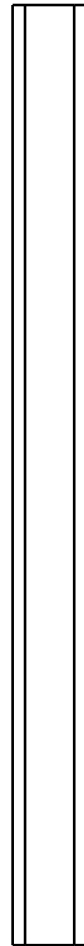
372.5



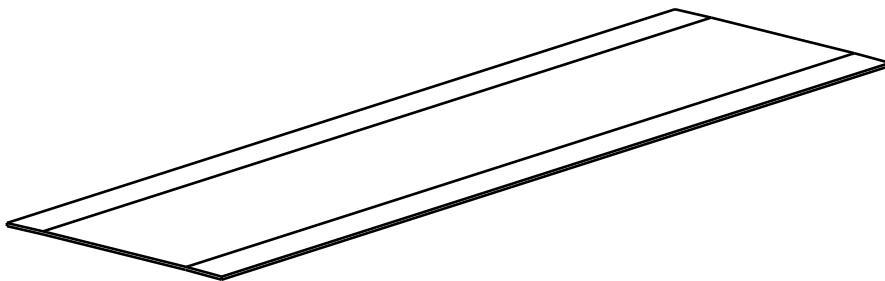
Right view
Scale: 1:3



Front view
Scale: 3:1



Top view
Scale: 1:3



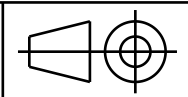
Isometric view
Scale: 1:1

DESIGNED BY:
Ricardo
DATE:
17/10/2020
CHECKED BY:
XXX
DATE:
XXX

UNITS ARE IN MILLIMETRES

I	-
H	-
G	-
F	-
E	-
D	-
C	-
B	-
A	-

SIZE
A4



ELASTOMER SHEET

SCALE
1:1

DRAWING NUMBER
Product1

SHEET
1 / 1

This drawing is our property; it can't be reproduced or communicated without our written agreement.

D

A

4

4

3

3

2

2

1

1

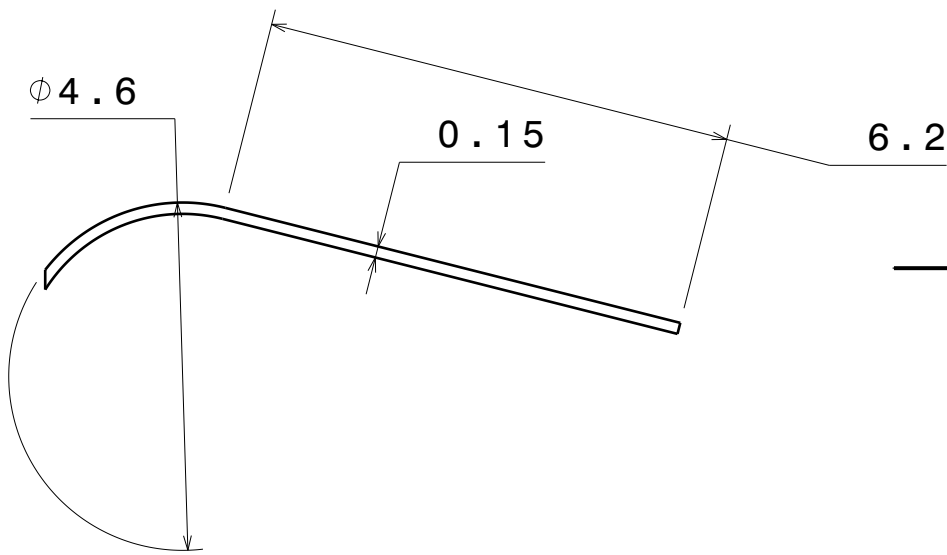
D

C

B

A

Front view
Scale: 10:1



Left view
Scale: 1:10

4

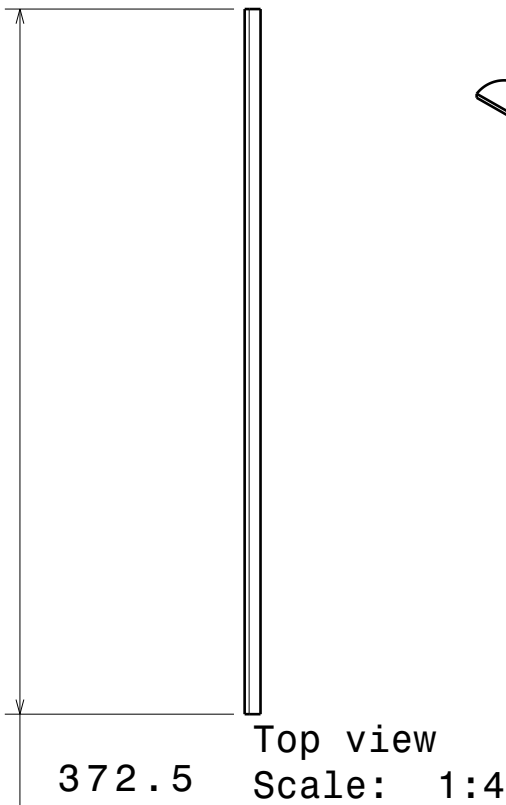
4

3

3

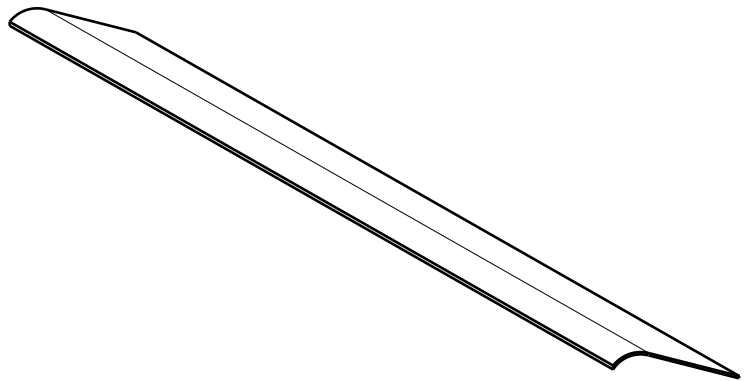
2

2



Top view
Scale: 1:4

Isometric view
Scale: 2:1



1

1

DESIGNED BY:
Ricardo

DATE:
17/10/2020

CHECKED BY:
XXX

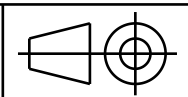
DATE:
XXX

UNITS IN MILLIMETRES

ELASTOMER SUPPORT

I	-
H	-
G	-
F	-
E	-
D	-
C	-
B	-
A	-

SIZE
A4



SCALE
1:1

DRAWING NUMBER
Part6

SHEET
1/1

This drawing is our property; it can't be reproduced or communicated without our written agreement.

D

A

D

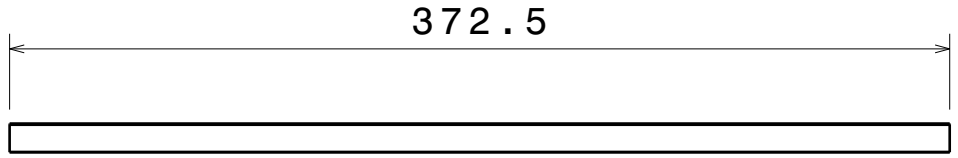
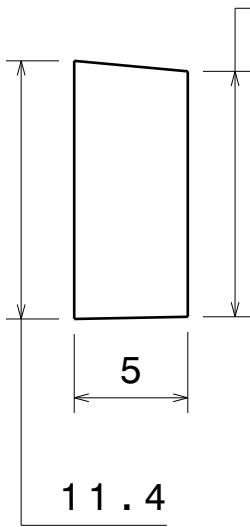
C

B

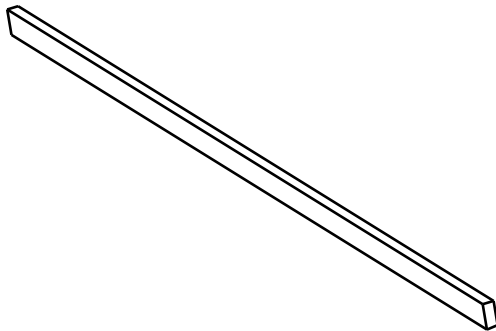
A

Front view
Scale: 3:1

Right view
Scale: 1:3



Isometric view
Scale: 1:3



Top view
Scale: 1:3



DESIGNED BY:
Ricardo

DATE:
17/10/2020

CHECKED BY:
XXX

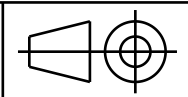
DATE:
XXX

UNITS IN MILLIMETRES

TE SPAR

I	-
H	-
G	-
F	-
E	-
D	-
C	-
B	-
A	-

SIZE
A4



SCALE
1:1

DRAWING NUMBER
Product1

SHEET
1/1

This drawing is our property; it can't be reproduced or communicated without our written agreement.

D

A

4

4

3

3

2

2

1

1

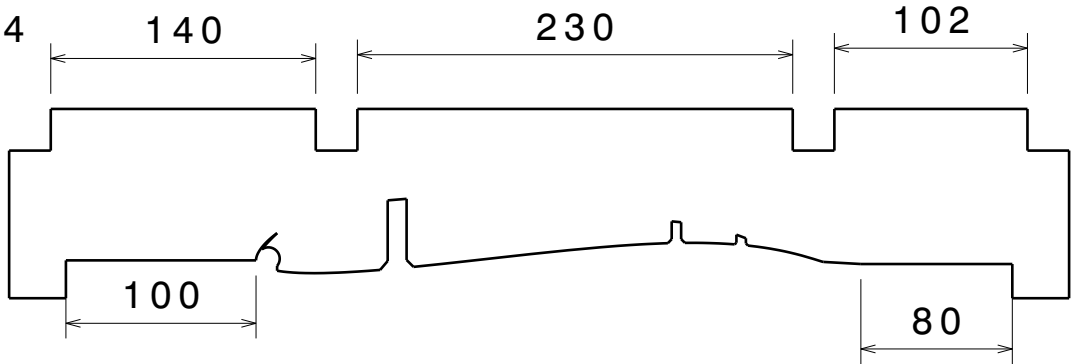
D

C

B

A

Right view
Scale: 1:4



22

22

22

22

5

22

78

Isometric view
Scale: 1:5

Top view
Scale: 1:5

Front view
Scale: 1:1

DESIGNED BY:
Ricardo

DATE:
17/10/2020

CHECKED BY:
XXX

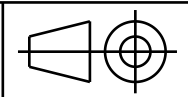
DATE:
XXX

UNITS ARE IN MILLIMETRES

JIG PLATE

I	-
H	-
G	-
F	-
E	-
D	-
C	-
B	-
A	-

SIZE
A4



SCALE
1:1

DRAWING NUMBER
wing_surface

SHEET
1/1

This drawing is our property; it can't be reproduced or communicated without our written agreement.

D

A

4

4

3

3

2

2

1

1

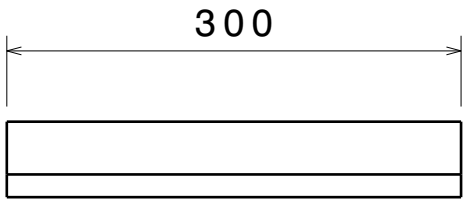
D

C

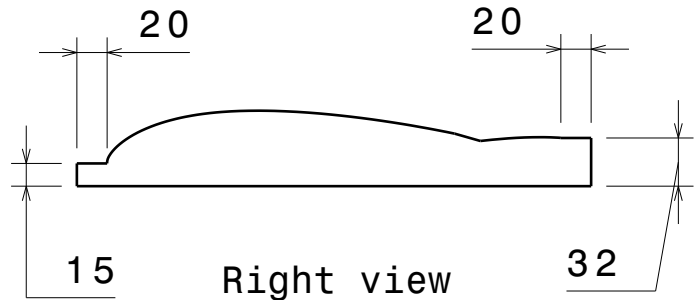
B

A

4

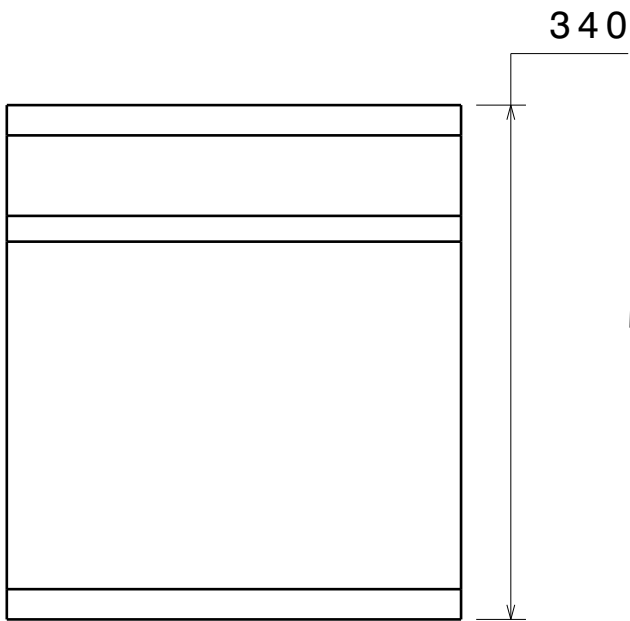


Front view
Scale: 1:5

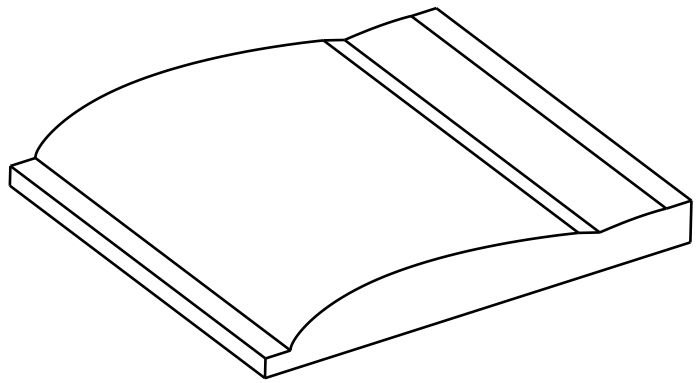


Right view
Scale: 1:5

3



Top view
Scale: 1:5



Isometric view
Scale: 1:5

2

4

3

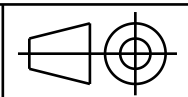
2

DESIGNED BY:
Ricardo
DATE:
17/10/2020
CHECKED BY:
XXX
DATE:
XXX

UNITS ARE IN MILLIMETRES

I	-
H	-
G	-
F	-
E	-
D	-
C	-
B	-
A	-

SIZE
A4



-20° DEFLECTION MOULD

SCALE
1:1

DRAWING NUMBER
molde elas

SHEET
1/1

This drawing is our property; it can't be reproduced or communicated without our written agreement.

D

A

1

1

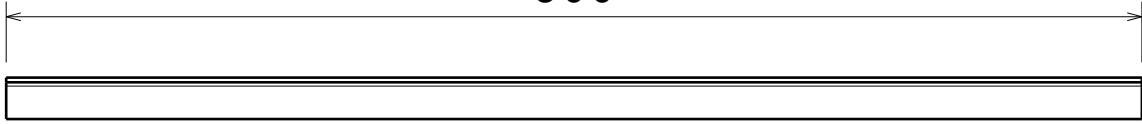
D

C

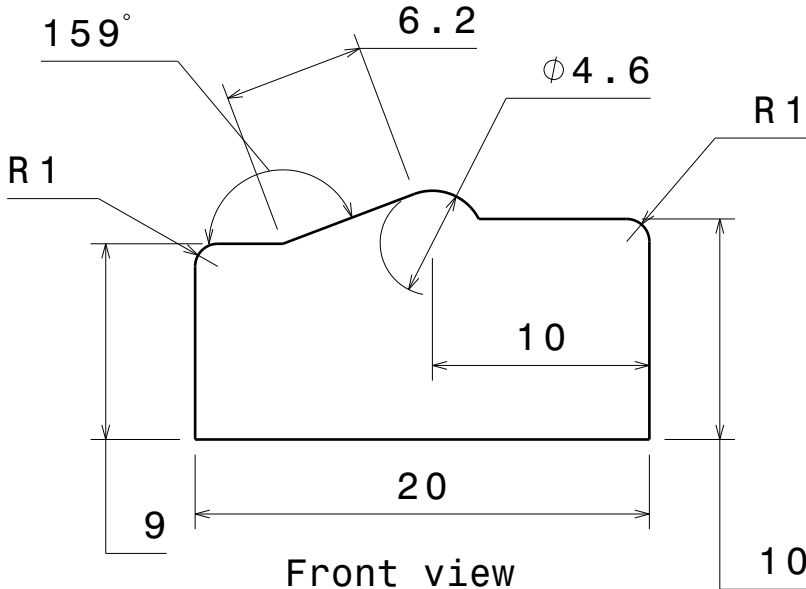
B

A

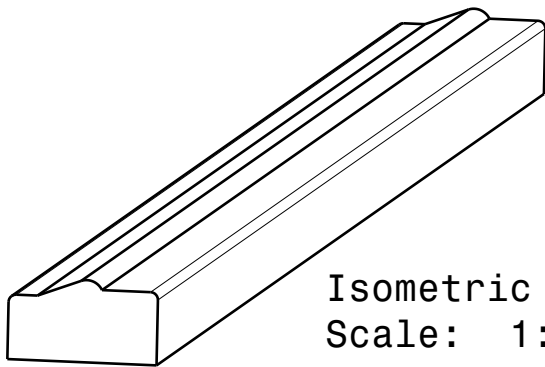
300



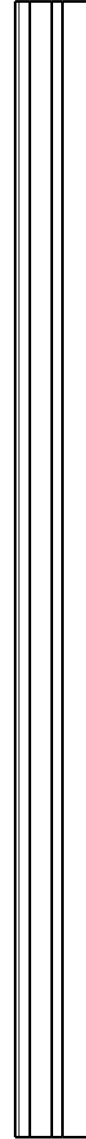
Right view
Scale: 1:2



Front view
Scale: 3:1



Isometric view
Scale: 1:1




Top view
Scale: 1:2

DESIGNED BY:
Ricardo
DATE:
17/10/2020

CHECKED BY:
XXX
DATE:
XXX

UNITS IN MILLIMETRES

SIZE
A4



ELASTOMER SUPPORT MOULD

SCALE
1:1

DRAWING NUMBER
molde suporte elas

SHEET
1/1

I	-
H	-
G	-
F	-
E	-
D	-
C	-
B	-
A	-

This drawing is our property; it can't be reproduced or communicated without our written agreement.

D

A

A.3 Matlab code

Listing A.1: Photometry code to determinate the Young's Modulus.

```
1 clear all
2
3 %valores de referencia%
4
5 sarea = 24; %area de seco do proveto%
6 xref = 50; %distancia entre marcaes no proveto%
7
8 %% ciclo for para ler e analisar todas as fotos%
9
10 for n=1:35 %indicar o numero de fotos%
11     images{n} = imread(sprintf('_DSC%03d.jpg',n)); %ler a foto%
12
13 Im=images{n};
14 %dividir a foto nos trs componentes RGB%
15 rmat=Im(:,:,1);
16 gmat=Im(:,:,2);
17 bmat=Im(:,:,3);
18
19 figure;
20 subplot(2,2,1), imshow(rmat);
21 title('Red Plane');
22 subplot(2,2,2), imshow(gmat);
23 title('Green Plane');
24 subplot(2,2,3), imshow(bmat);
25 title('Blue Plane');
26 subplot(2,2,4), imshow(images{n});
27 title('Original Image');
28
29 %ajustar os niveis de contraste para cada plano RGB%
30 levelr = 0;
31 levelg = 0.35;
32 levelb = 0;
33
34 %converter planos para preto e branco%
35 i1=im2bw(rmat,levelr);
36 i2=im2bw(gmat,levelg);
37 i3=im2bw(bmat,levelb);
38 Isum = (i1&i2&i3); %somar os 3 planos numa imagem%
39
40 %Plot the data%
```

```

41
42 figure,
43 subplot(2,2,1), imshow(i1);
44 title('Red Plane');
45 subplot(2,2,2), imshow(i2);
46 title('Green Plane');
47 subplot(2,2,3), imshow(i3);
48 title('Blue Plane');
49 subplot(2,2,4), imshow(Isum);
50 title('Original Image');
51
52     % Complementar e estruturar a imagem&
53
54 %Inverter o preto e branco e encher a imagem%
55 Icomp = imcomplement(Isum);
56 Ifilled = imfill(Icomp,'holes');
57
58 figure,
59 imshow(Ifilled);
60
61 %estruturar os objectos da imagem%
62 se = strel('line',75,0); %tipo de estrutura, dimenso, ngulo%
63 Iopenned = imopen(Ifilled,se);
64
65 figure
66 %imshow(Iopenned);
67 imshowpair(Iopenned, images{n});
68
69
70 % Extrair propriedades %
71 [labeled,numObjects] = bwlabel(Iopenned,4); %detectar numero de
    objectos na imagem%
72 Iregion = regionprops(Iopenned, 'centroid'); %achar propriedades do
    objecto (centroide)%
73 %sobrepor centroide na imagem original%
74 figure, imshow(images{n});
75 hold on;
76 for x = 1 : numel(Iregion)
77     plot(Iregion(x).Centroid(1),Iregion(x).Centroid(2),'ro');
78 end
79

```

```

80 cent = cat(1,Iregion.Centroid); %extrair dados do centroide num
    vector simples%
81 lenght = pdist(cent,'euclidean'); %calcular distncia entre os
    centroides%
82 u(n) = lenght; %adicionar valor ao vector u%
83 end
84 pixelsize = xref/u(1); %calcular dimenso de cada pixel
85 metric = pixelsize*u; %multiplicar o vector u pela dimenso do
    pixel para obter distancia unidades metricas"
86 F = importdata('force.txt'); %importar dados de ficheiro txt com os
    valores da fora%
87 FF = F.';
88 T = FF/sarea; %calcular stress%
89 D = (metric-metric(1))/metric(1); %calcular strain$
90
91 %% grfico %%
92
93 figure; %fazer grfico da tenso em funo do deslocamento
94 % fazer grfico %
95 plot(D, T, 'bo', 'LineWidth', 1.5, 'MarkerSize', 7.5);
96 grid on;
97 set(gcf, 'PaperPosition', [0 0 12 10])
98 set(gcf, 'PaperSize', [12 10]);
99 fontSize = 20;
100 % title(' Tenso vs Deslocamento', 'FontSize', fontSize);
101 xlabel('Strain  $\left[\frac{\Delta L}{L_0}\right]$ ',
    'interpreter','tex');
102 ylabel('Stress  $\left[\text{MPa}\right]$ ', 'interpreter', 'tex');
103 ax = gca;
104 ax.YAxis.TickLabelFormat = '%.2f';
105 coefficients = polyfit(D, T, 1);
106 fittedY = polyval(coefficients, D);
107 slope = coefficients(1);
108 hold on;
109 % Introduzir valor da recta de declive numa caixa %
110 plot(D, fittedY, 'r-', 'LineWidth', 1.5, 'MarkerSize', 7.5);
111 annotation('textbox', [0.6 0.3 .1 .1], 'String', ['slope = ', num2str
    (slope)], 'FitBoxToText', 'on', 'BackgroundColor', 'white');
112 legend({'Exp. data', 'Fitted data'}, 'interpreter', 'tex', 'Location',
    'northwest');
113 saveas(gcf, 'elas', 'svg')

```

Listing A.2: Code to calculate the available servo hinge torque.

```

1 clear all
2
3 syms x1 x2 y1 y2 r1 r2 a b d alfaRef alfa beta torque delta p1 p2
   Mjoint deltaDeg
4 r1 = input('\r1 :'); %raio do brao do guinhol%
5 r2 = input('\r2 :'); %raio do brao do servo%
6 alfaRef = deg2rad(input('\alfaRef :')); %angulo do guinhol para
   deflexao neutra%
7 a = input('\a :'); % Posio x do eixo do servo em relao a dobradica
   %
8 b = input('\b :'); % Posio y do eixo do servo em relo a dobradica%
9 d = input('\d :'); %Comprimento da haste%
10 torque = input('\Servo torque[kgf*cm] :'); %Binario do servo%
11
12 deltaI = deg2rad(input('delta inicial :')); %Deflexao inicial%
13 deltaF = deg2rad(input('delta final :')); %Deflexao final%
14 int = deg2rad(input('intervalo :')); % Passo de deflexao%
15 i=0;
16
17 %ciclo for para calcular a posicao%
18 for delta = deltaI:int:deltaF
19
20 alfa = alfaRef-delta;
21 i=i+1;
22
23 deltaDeg(i)= rad2deg(delta);
24
25 eqn1 = cos(alfa)*r1 == x1;
26 eqn2 = sin(alfa)*r1 == y1;
27 eqn3 = (x2-a)^2+(y2-b)^2 == r2^2;
28 eqn4 = (x2-x1)^2+(y2-y1)^2 == d^2;
29 eqn5 = y2<b;
30
31 sol = solve([eqn1, eqn2, eqn3, eqn4, eqn5], [x1, x2, y1, y2]);
32 x1Sol(i) = vpa(sol.x1);
33 y1Sol(i) = vpa(sol.y1);
34 x2Sol(i) = vpa(sol.x2);
35 y2Sol(i) = vpa(sol.y2);
36
37 beta(i) = asin((y2Sol(i)-b)/r2);
38 Fi = acos(abs(x2Sol(i)-x1Sol(i))/d);

```

```

39 psiG = deg2rad(90)-Fi-alfa;
40
41 psiS = deg2rad(90)-Fi-beta(i);
42
43 Fservo = torque/r2;
44 Ftirante = Fservo*cos(psiS);
45 Fguinhol = Ftirante*cos(psiG);
46 Mjoint(i) = vpa(Fguinhol*r1);
47
48
49 end
50
51 figure,
52 hold on
53 for t=1:1:i
54 plot([x1Sol(t),x2Sol(t)],[y1Sol(t),y2Sol(t)],'+-')
55 end
56 hold on
57 %x and y are the coordinates of the center of the circle
58 %r is the radius of the circle
59 %0.01 is the angle step, bigger values will draw the circle faster
    but less
60 %perfect%
61 ang=0:0.01:2*pi;
62 xp=r1*cos(ang);
63 yp=r1*sin(ang);
64 plot(0+xp,0+yp);
65 xp2=r2*cos(ang);
66 yp2=r2*sin(ang);
67 plot(a+xp2,b+yp2);
68 plot(0,0,'*');
69 plot(a,b,'*');
70 hold off
71 %Fazer grafico%
72 figure,
73 plot(deltaDeg,Mjoint)

```